Stretching and Slipping Liquid Bridges: Liquid Transfer in Industrial Printing

A dissertation
submitted to the faculty of the graduate school
of the University of Minnesota
by

Shawn Dodds

In partial fulfillment of the requirements
for the degree of
Doctor of Philosophy

Advisors: Satish Kumar and Marcio Carvalho

August, 2011

Acknowledgements

Science is at its core a collaborative discipline, where the unrelated insights of others have a unique impact on the way an individual approaches a problem. This thesis is no exception and, despite having a single author listed, it is the work of many people spread over many years who all deserve recognition. First and foremost I would thank my advisers, Professors Satish Kumar and Marcio Carvalho, for their constant support and guidance. Through them I not only learned how to do research, but how to be a more patient, organized person (which was sorely needed!). I would have struggled endlessly without them.

I would like to thank the late Prof. Skip Scriven for introducing me to the field of fluid mechanics and for whipping me into shape as a graduate student, even though this process was at times quite painful. I am truly fortunate to have had Skip as a teacher and a mentor, and I wish I had known him better. I would like to thank Prof. Lorraine Francis for teaching me what I know about coating and drying, and for helping to keep me focused on practical problems instead of theoretical abstractions. I would like to thank Prof. Victor Barocas for always having an open door, and for helping to guide me through my graduate career. Dr. Andrew Yeckel, Dr. Jaewook Nam and Dr. Kristianto Tjiptowidjojo taught me what little I know about the finite element method, and I thank them for their patience in guiding me through such a confusing maze. Wieslaw Suszynki was essential for all experimental work, and for making sure I didn't break anything.

I tell incoming graduate students that the most important decision they will make is not so much their future adviser, but their future group. I don't think I could have chosen better people to have buying me coffee, and I would like to thank Dr. Scott Roberts, Dr. Chunfeng Zhou, Dr. Nazish Hoda, Dr. Rick Lenz, Dr. Balram Suman, Dr. Changkwon Chung, Benson Tsai, Damien Brewer, Eric Vandre, Sreeram Kalpathy, Aruna Ramkrishnan, and Drew Corbett for many hours of useful discussions and distractions. I have also been fortunate enough to take part in the coating process fundamentals program, which has convinced me that coatings engineers will ***always*** be needed. I would like specifically to thank Dr. Christine Cardinal, Dr. Alex Lee, and Dr. Dan O'Neal (as well as Kris and Jaewook) for many interesting discussions. I would also like to thank the Carvalho and de Souza Mendes groups at PUC-Rio for giving me a home away from home.

Finally, I would like to thank my friends and family for all of their support. More than anyone else, this thesis is the result of your efforts in shaping me into the person that I am.

Abstract

Liquid bridges with moving contact lines are found in a variety of settings, such as capillary feeders and high-speed printing processes. Despite this relevance, studies on liquid bridges often assume that the contact lines remain pinned in place during stretching. While this may be the case for some applications, contact line motion is *desirable* in printing processes so that the amount of liquid transferred can be maximized. In this thesis we study several model problems to improve our understanding of how moving contact lines alter the dynamics of liquid bridges.

We use the finite element method to study the stretching of a liquid bridge between either two flat plates or a flat plate and a cavity. For axisymmetric bridges we find that while the wettability of the two surfaces is a key factor in controlling liquid transfer between two flat plates, the presence of a cavity leads to fundamentally different bridge dynamics. This is due to the pinning of the contact line on the cavity wall, which leads to a decrease in the amount of liquid transferred to the flat plate. We find that the presence of inertia aids in cavity emptying by forcing the interface further into the cavity. However, this increase in emptying can be offset by an increased tendency for the production of satellite drops as the flat plate is made more wettable.

To study non-axisymmetric flows we solve the Navier-Stokes equations in three dimensions. We find that when the stretching motion is asymmetric the liquid remains evenly distributed after breakup, so long as the two plates are not accelerating relative to each other. If the bridge shape is not initially cylindrical we find that the ability of the bridge to maintain its initial shape after breakup depends on the friction between the contact line and the solid.

Finally, we use flow visualization to observe the stretching of liquid bridges both with and without small air bubbles. We find that while the breakup of wetting fluids between two identical surfaces is symmetric about the bridge midpoint, contact line pinning breaks this symmetry at slow stretching speeds for nonwetting fluids. We exploit this observation to force the bubbles selectively toward the least hydrophillic plate confining the bridge.

Contents

List of Tables

List of Figures

CHAPTER 1

Introduction

It is a rare occurrence to find a commercial product that has not, in some way, been involved in a printing or coating process. Clothing, scratch-resistant glass, circuit boards, newspapers, photographic film, and non-stick cookware are all examples of printed and/or coated products. Coating is often defined as the *continuous* displacement of a gas at a solid surface by a liquid (Scriven, 2005). Our understanding of coating flows has advanced significantly over the past few decades, and there are now several review articles and books on the subject (Cohen and Gutoff, 1992; Kistler and Schweizer, 1997; Weinstein and Ruschak, 2004; Scriven, 2005). In contrast to coating, printing can be defined as the *discrete* displacement of a gas at a solid by a liquid. This seemingly subtle difference between the two techniques leads to fundamental differences in the fluid mechanics governing each process. In coating, for example, a steady, two-dimensional flow is desired so that long production runs of uniform product can be maintained. In printing, however, the reproduction of a discrete pattern means that the flow will be inherently transient and three-dimensional, significantly complicating both experimental and theoretical analyses. Current printing processes are able to produce pattern resolutions below the scale detectable by the human eye ($\sim$ 50 μm when viewing at $\sim$ 10 cm, see Clark, 2011), and even our home printers can produce vivid, well-resolved images. However, advances in the solution processing of electrically conducting materials has made the use of traditional printing processes feasible for the large-scale manufacture of electronic devices, presenting a market of nearly $3 billion in 2008 (Markets and Markets, 2011). This requires the production of features as small as 100 nm (Gamota et al., 2004), which represents a significant increase in resolution from current printing technology. To achieve such high resolutions requires not just our current technical know-how for each printing operation, but a fundamental understanding of the physical mechanisms governing printing. In particular, the transfer of liquid from one surface to another is a key stage in any printing process which remains poorly understood. The goal of this thesis is to improve our understanding of the mechanisms through which this transfer occurs, with a particular emphasis on gravure printing.

1.1 Industrial printing processes

We begin by summarizing five of the most promising techniques for the large-scale printing of organic electronics (Michel et al., 2001). For the interested reader, Krebs (2009) has written an excellent review on techniques for solution processing of polymer solar cells specifically, which covers most of the techniques discussed here. The Graphic Arts Technical Foundation (GATF) also provides very good technical primers on several of these techniques, including gravure (Kasunich, 1998), lithography (Wilson, 2005), flexography (Crouch, 1998), and screen printing (Ingram, 1999).

1.1.1 Ink-jet printing

Ink-jet printing is likely the technique that the average person is the most familiar with, given its ubiquity at home and in the workplace. In ink-jet printing, liquid is ejected from a nozzle in discrete droplets that eventually land on a substrate. The substrate and/or the nozzle are displaced so that the drops land in different locations, creating the desired pattern (figure 1.1). While a personal printer often has only 4 nozzles, one for black and three for color, an industrial ink-jet printer may have more than one hundred nozzles (Creagh and McDonald, 2003).

There are several pumping mechanisms used to produce the liquid drop, but the two most common are thermal and piezoelectric. In thermal (or bubble) jet printing, a resistor is used to heat a small piece of fluid, causing the formation of a bubble that forces ink out of the nozzle as the bubble expands. Once the pressure in the nozzle is large enough the bubble breaks, resulting in a vacuum that pulls more ink in from a reservoir, allowing the process to be repeated indefinitely. The rate of drop production is thus limited by the ability to expand and collapse this vapor bubble. In piezoelectric printing, a small voltage is applied to a piezoelectric crystal, causing it to oscillate. This oscillation produces a drop production cascade similar to the one in thermal ink-jet printing, though here the rate of drop production is limited by the material properties of the crystal (Gamota et al., 2004).

The primary advantage of ink-jet is that it can be easily adjusted to produce different patterns by simply changing the profile of pressure actuation within the nozzle, along with the location of the nozzle relative to the substrate. This allows drops to be produced only when they are required, so that ink-jet is sometimes called a drop-on-demand technique. For applications that do not require a large number of copies, this adaptability is a distinct advantage over the other printing techniques discussed in this chapter, which require a physical or chemical image to produce a pattern. Because the size of the drop and the location of the nozzle can be precisely controlled, ink-jet printing is able to produce high-resolution images. However, high printing speeds cannot be attained because the liquid is applied drop by drop, instead of continuously as in gravure or lithographic printing. Additionally, if drop formation is not precisely controlled it is possible to produce secondary drops known

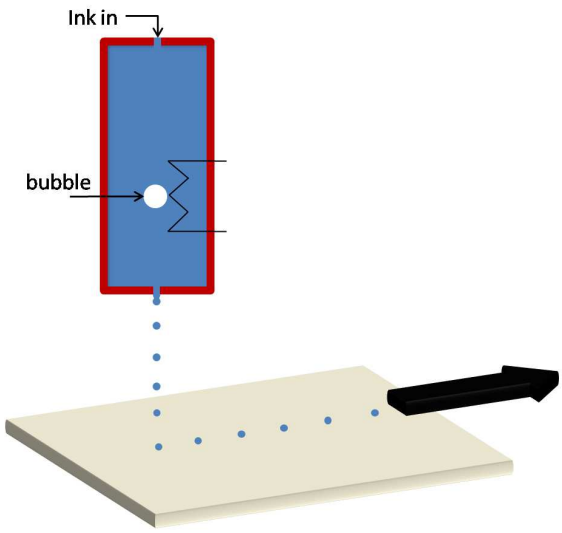

Figure 1.1: Schematic of an ink jet printing apparatus

as satellites, or even continuous jets of ink, that can damage the final pattern resolution (Yildirim and Basaran, 2006). Finally, ink-jet printing nozzles can become clogged, leading to defects in the final pattern. Despite this, ink-jet is considered a prime candidate for printing electronics, and it has already been used to print transistors (Sirringhaus et al., 2000), light emitting diodes (LEDs, see Bharathan and Yang, 1998; Shimoda et al., 2003) and DNA microarrays (Blanchard et al., 1996; Hughes et al., 2001).

1.1.2 Screen printing

Screen printing is also a technique many of us are familiar with, often from silk-screening in an art class. However, this seemingly simple technique can be scaled up to produce prints $2-3$ m wide, and is already used to print circuit boards (Gamota et al., 2004).

The principle of operation for screen printing is quite simple, and is depicted graphically in Figure 1.2. A screen, which is a matrix of regularly woven fibres, is first coated in a photosensitive polymer. An area of the screen is blocked off, and the entire screen is exposed to UV light. This cures the polymer in the exposed areas of the screen, allowing the unexposed polymer to be rinsed off while leaving a gap in the screen through which liquid can be passed (see the inset picture in Figure 1.2). A substrate is then brought under the mesh, and ink is scraped across the top of the mesh using a squeegee. Pressure is applied to ensure that ink seeps through the fibres, and the ink is transferred onto the substrate (Gamota et al., 2004).

Because the screen is flexible and the squeegee is able to apply additional pressure, this method can be used with high viscosity inks (up to 50 poise), which helps the ink to retain its shape after printing. This is important for inks with high solids loadings, where the viscosity may be too high for the other printing techniques discussed in this chapter.

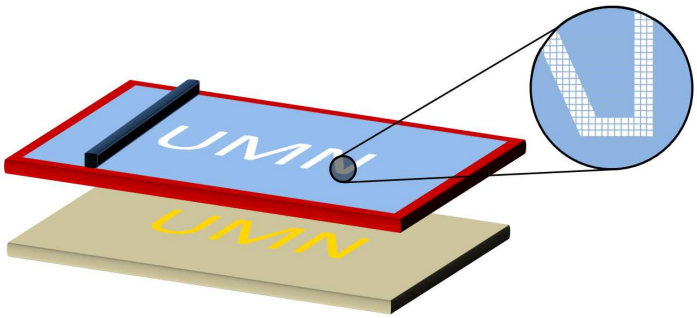

Figure 1.2: Schematic of a screen printing apparatus

Screen printing also allows for the production of very thick coats because many passes with the squeegee can be made, while the substrate is successively lowered to leave room for each new layer of ink (Gamota et al., 2004). This would be difficult to achieve in a roll printing technique such as gravure, where multiple copies of the same roll would be required to produce such a thick coating.

Because of its simplicity, screen printing has been widely used on a lab-scale to print components for devices such as transistors (Bao et al., 1997), organic LEDs (OLEDs, see Pardo et al., 2000; Birnstock et al., 2001), solar cells (Durr et al., 2005), and motion sensors (Sekitani et al., 2007). However, screen printing has the lowest resolution of the methods presented in this section (see table 1.1) as well as a low printing speed compared to other roll-to-roll techniques.

1.1.3 Gravure printing

First developed in England in 1784, gravure has become one of the most widely used printing methods in the world. Gravure is commonly employed to print materials at high volumes, such as magazines/catalogues, stamps and labels. Additionally, the high resolutions possible with gravure have made it a method of choice in the graphics arts industry (Kasunich, 1998). While we briefly discuss the basics of gravure here, we review it in more depth in section 1.2 because of its importance to this thesis.

In its simplest form gravure involves four components (see figure 1.3). The gravure roll is a chrome-plated cylinder that has been engraved with a large number of small cavities or grooves, some examples of which are shown in Figure 1.4. The cavities are filled with liquid from a pool beneath the gravure roll, and any excess fluid is wiped off by a doctor blade. This ideally leaves the area between the cavities (the lands) dry, and allows the amount of fluid that is printed to be controlled by the cavity volume. A substrate is then pressed against the gravure roll, often with a rubber backing roll to apply additional pressure and ensure good contact between the substrate and the cavities (Kasunich, 1998). As the web and roll are separated, a liquid bridge forms which is stretched and broken, pulling liquid out of the cavities and onto the web. However, liquid transfer is often incomplete, which

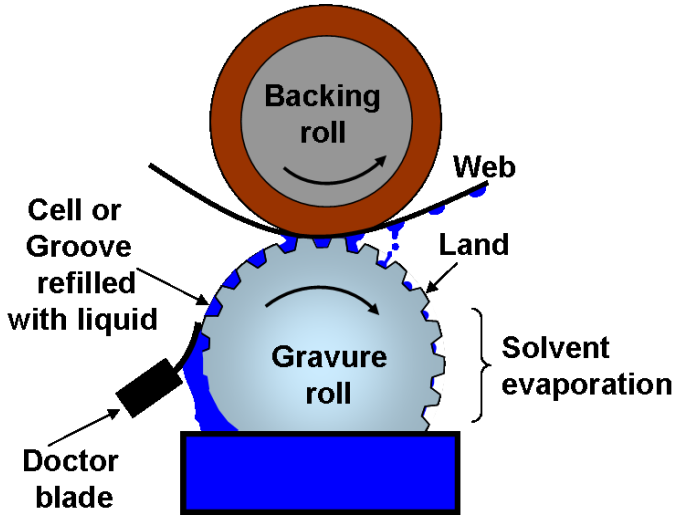

Figure 1.3: Schematic of gravure apparatus

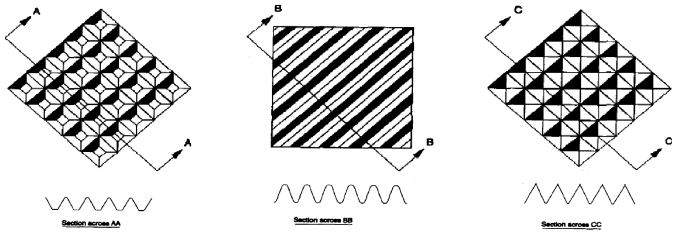

(a) (b) (c)

Figure 1.4: Different gravure cell geometries, taken from Benkreira and Patel (1993), (a) quadrangular, (b) trihelical, and (c) pyramidal

can leave gaps in the printed pattern. Additionally, if the ink contains a volatile solvent, residual solids can collect in the cavities as the solvent evaporates. This fouling can lead to coating defects because the effective cell volume and geometry have been altered (Yin and Kumar, 2006a). Once the pattern has been dried, the web can be passed through additional gravure rolls to apply inks with different compositions or colors. For graphic arts applications, a gravure press will often have 8 or more different rolls.

Gravure is a popular technique because it is able to produce high-resolution features ($\sim$10 μm) at high speeds (up to 15 m/s). Because the pattern has been engraved into a chrome-plated metal roll, the features degrade slowly and each roll is able to produce millions of copies before it must be replaced. However, the rolls take hours to engrave, so the desired pattern cannot be easily changed. The rolls are also expensive, and one needs to make hundreds of thousands of copies to pay back the additional cost of manufacturing a gravure roll relative to rolls for lithography or flexography. Despite this, gravure has been used for several cutting-edge applications, including the printing of electric circuits (Hagberg et al., 2001; Kittilä et al., 2004; Pudas et al., 2004), antennas (Pudas et al., 2005),

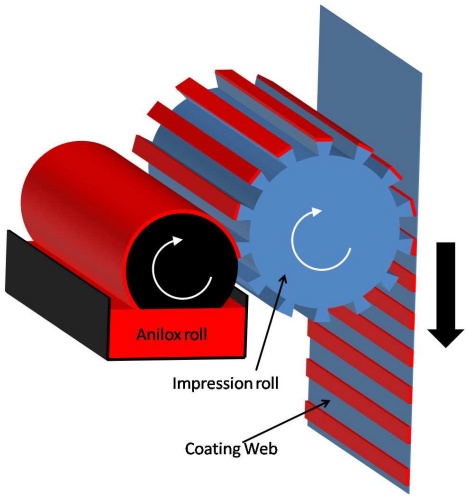

Figure 1.5: Schematic of a flexographic printing apparatus

solar cells (Santa-Nokki et al., 2006) and photocatalytic coatings (Kawahara et al., 2003).

1.1.4 Flexographic printing

Flexographic printing, which is often simply called flexo, is in a sense gravure coating with an extra step. Liquid is transferred from a pool to an anilox roll, which is an engraved cylinder similar to a gravure roll, with any excess fluid wiped off using a doctor blade (see figure 1.5). The purpose of the anilox roll is to control the amount of fluid that is printed. The fluid is then transferred from the anilox roll to an impression roll, which has been patterned with an upraised polymer layer. The impression roll is then pressed against the web, normally with a backing roll used to ensure contact between the web and the impression roll, allowing the transfer of liquid to take place (Gamota et al., 2004).

The advantage to flexographic printing is that the rubber impression layer allows the surface to conform to rough or oddly shaped surfaces, which allows flexography to be used on a much wider array of substrates than gravure. Flexographic rolls are also much cheaper and easier to produce than gravure rolls because they don't require the engraving of a unique metal roll for each pattern. The trade-off is that the flexibility of the polymer decreases the attainable pattern resolution, as it can deform and smudge the desired features. Additionally, these rolls have a shorter life-span than gravure because the polymer wears more easily than the chrome plated roll. Therefore, flexographic printing has traditionally been used for low-resolution, low value-added applications, such as printing on cardboard and bread bags (Gamota et al., 2004). However, as our ability to manufacture the impression and anilox rolls has improved, flexography has been able to produce prints with comparable quality to gravure and lithography (Larson, 2007). Flexography has been used in the printing of polymer transistors (Mäkelä et al., 2005) and conductive wires (Han et al., 2007; Kwak et al., 2010).

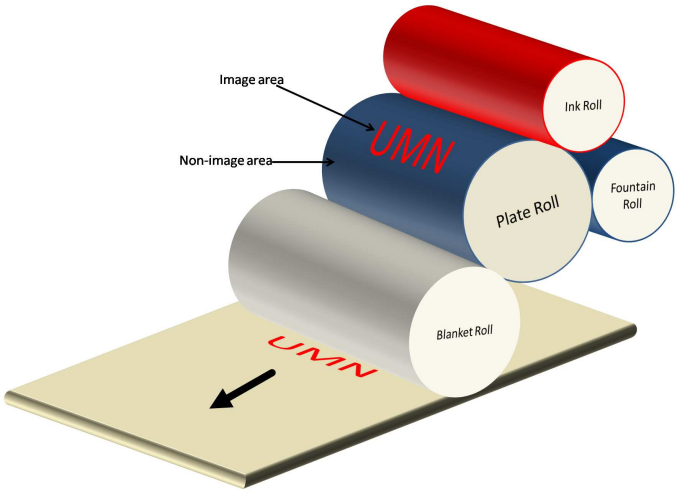

Figure 1.6: Schematic of a lithographic printing apparatus

1.1.5 Lithographic printing

Lithographic printing was developed in the late eighteenth century by a German playwright named Alois Senefelder, who was trying to find a way to print screenplays without having to engrave expensive copper plates. In the two centuries since its conception, lithography has developed into one of the most powerful printing tools, used for products as varied as newspapers, business forms, and scratch tickets (Gamota et al., 2004).

While the term lithography can refer to many different processes, the common thread is the use of a chemically patterned surface to produce a desired shape. In lithographic printing, this is accomplished through hydrophobic (image) and hydrophilic (non-image) areas on the plate roll (see figure 1.6). An emulsion is created on the plate roll using separate ink and fountain solutions. This emulsion is designed to provide the desired amount of ink while maintaining an appropriate fluid viscosity. The hydrophobic ink displaces water from the image area, filling in the pattern on the plate roll. The ink is then transferred to a rubber blanket roll, which can deform to allow printing on non-planar surfaces (MacPhee, 1998).

Because the fluid is transferred using surface forces, the wetting/dewetting properties of the fluid and plates must be carefully designed to ensure the fidelity of the printed pattern. Viscous inks, up to 500 poise (MacPhee, 1998), are often used to minimize spreading during drying, which helps to create high resolution images. This is a distinct advantage over gravure or flexographic printing processes, where low viscosity inks (1-100 cp) are required to properly fill the cells in the gravure/anilox roll (Gamota et al., 2004). The ability to print viscous fluids also allows inks with high solids content to be used, which is important when printing electronic circuits. However, the chemical pattern wears more easily than the mechanical pattern used in gravure, leading to relatively short production runs before a new

Table 1.1: A summary of the fabrication techniques for flexible/organic electronics. Unless otherwise cited, all information is from Gamota et al. (2004)

Method	Speed	Resolution	Strength	Weakness
Ink-jet	10 kHz[a]	20 μm	Drop-on-demand	Slow
Screen	3 m/s	50 μm	Very cheap	Slow, poor resolution
Gravure	15 m/s	15 μm	Fast, high resolution	Expensive
Flexography	7 m/s	40 μm	Balance of cost/speed	Moderate resolution
Lithography	15 m/s	20 μm[b]	Cheap image plates	Short plate lifetime

[a]Creagh and McDonald (2003). The speeds for ink-jet are normally given in Hz, which represents the number of drops formed per second

[b]Parashkov et al. (2005)

plate roll must be fabricated. Lithographic printing has been used to print source/drain structures for field-effect transistors (Zielke et al., 2005) and batteries (Southee et al., 2007).

1.1.6 Comparison of methods

Each of the methods discussed in this section has advantages and disadvantages, and it is possible that they will all have their own niche applications. For example, when fabricating display screens it is not important to make thousands of feet per minute, but the print quality must be very high and many printed components are required, so ink-jet may be the most appropriate technology. However, radio-frequency identification (RFID) tags must be mass-produced to be economical, though they do not generally require micron-sized features. Therefore, gravure or flexography are likely the best options for this type of application. We summarize the key factors one should consider when choosing a particular printing technique in table 1.1.

1.2 Review of literature relevant to gravure

Because of its high speed and resolution, as well as its mechanical simplicity, gravure is considered to be one of the most promising printing techniques for the mass-production of organic electronics. However, as we discussed in section 1.1.3 gravure is a poorly understood process, and its operation is still considered to be somewhat of an art. The purpose of this section is to provide context for the work performed in this thesis, which builds on the existing literature. We organize this section into three major areas of study: doctoring in gravure, gravure coating, and gravure printing.

1.2.1 Doctoring in gravure

The metering action in gravure is provided by a doctor blade, which cleans excess fluid off the lands in an attempt to ensure that only the fluid in the cavities is transferred to the web. This is a sensitive process, as under-doctoring can lead to overfilled cells and wet lands,

which increases the coating thickness and decreases the pattern resolution. Conversely, over-doctoring can result in poor contact between the web and the liquid, leading to a decrease in the amount of liquid removed from the cavity, and potential gaps in the printed pattern. Therefore, an understanding of the doctoring process is essential in achieving consistent, high quality products with gravure.

Our understanding of doctoring in gravure is largely built through the use of lubrication theory, which takes advantage of the fact that the gap between the blade and the roll is generally much smaller than the width of the blade. As a blade glides over a lubricating liquid film, the pressure in the film increases as the gap between the blade and the surface decreases. In gravure, this results in higher pressures over the lands, where the gap is small, than within the cavities. Therefore, doctoring is able to clear the lands by driving liquid into the cavities (Kistler, 1988). As the capillary number is increased and viscosity becomes more important the blade deflects more significantly, leading to a smaller pressure differential and thus a thicker film on the land (Patel and Benkreira, 1991). Therefore, good doctoring is obtained at low capillary numbers. However, if the capillary number is too low it is possible that the meniscus will drag liquid out of the cavity, resulting in under-doctoring and poor liquid transfer.

Another study on doctor blades was motivated by an observation that the mean coating thickness from a gravure roll decreases steadily after installation of a new blade. To understand this, Hanumanthu (1999) used a lubrication model to describe the flow between the blade and a flat surface, including a model for the wear of the blade. The coating thickness was calculated as a function of time, and then fit to experimental data using the blade thickness as a regression parameter. The theory accurately predicts experimental results, showing that blade wear alone is enough to account for the change in coating thickness with time.

1.2.2 Gravure coating

Once doctoring is complete, a substrate is pressed against the gravure roll and the cavities are emptied. This is where the differences between gravure printing and coating become apparent. In coating, the cavities are organized in a way that promotes hydrodynamic interaction between each cavity, so that the features merge properly and a uniform film is produced over the entire substrate. In printing, however, this merging would ruin any discrete pattern, and so proper spacing between each feature must be included. This results in completely different flow profiles for coating and printing, and thus separate studies are required to understand and optimize the dynamics of each process.

Much of the early understanding of gravure was confined to the trade and patent literature, and was focused on observations of specific systems without any attempts to gain insight into the fundamental science of the process. While there is no summary of these works in the literature, there are several reference sources for the gravure practitioner (Ka-

sunich, 1998; Kipphan, 2001; Gamota et al., 2004). Pulkrabek and Munter (1983) performed the first systematic study of gravure, finding that stable coatings at high speeds could be obtained in trihelical gravure by matching the wavelength of the grooves on the gravure roll to the wavelength of the ribbing instability, as predicted at the same conditions for smooth rolls. Benkreira and Cohu (1998) were able to expand the operating window of Pulkrabek and Munter (1983) to include several cavity geometries, while also observing that if the substrate speed is much higher than the roll speed, an air-entrainment limit is reached.

Benkreira and Patel (1993) were the first to relate the coated film thickness to the process variables, such as the Reynolds number and the cavity shape. They found that at a high enough Reynolds number, the film thickness depends only on the cavity geometry/arrangement. However, they ignored the effect of surface tension, which was shown by Kapur (2003) to be a key parameter in controlling the amount of liquid removed from the cavities. Kapur (2003) also found that complete cavity emptying could be achieved by increasing the speed of the substrate relative to the gravure roll, producing a shearing motion. This is an excellent example of the differences between gravure coating and printing. While shear may help in emptying a cavity, it can also potentially distort any discrete features, which would be catastrophic for a printing application.

There has been some success in developing theoretical models to describe the fluid mechanics of gravure coating. Kapur et al. (2001) used a lubrication model to study the onset of ribbing in offset gravure, which does not include the presence of the cavities. This model was extended to include trihelical cavities with a square geometry by Hewson et al. (2006) and with an arbitrary shape and inclination relative to the coating direction by Hewson et al. (2010). Lee et al. (2010) showed that the amount of liquid transferred from a trihelical gravure roll can be related simply to the angle of inclination of the grooves relative to the substrate, with a higher inclination leading to a decrease in the amount of liquid transferred. In all of these cases, convincing agreement with experimental results was observed. However, offset and trihelical gravure present rare cases where two-dimensional, steady state operation is possible. In the more general case the cavities are three-dimensional (see figure 1.4), and no steady state reference frame can be found.

To address these issues, one must at a minimum consider the transient motion of an interface over an array of cavities. This has been done with a lubrication model by Schwartz et al. (1998), who found that better emptying was obtained with wider cavities, which is in agreement with the experimental results of Kapur (2003). The same model was also used by Schwartz (2002) to understand the effect of cavity arrangement on the transfer of liquid to the web. For the patterns studied, the amount of liquid initially removed from the cavities was nearly identical in all cases. However, as the cavities were emptied the meniscus would eventually impinge on the cavity walls and on the lands, causing liquid to flow back into the cavity and decreasing the final liquid transfer. It is during this refilling stage that the cavity arrangement becomes relevant, with different amounts of refilling for each pattern.

While this work provides important insight into the mechanism of liquid transfer, it also makes several unrealistic simplifications, most importantly that the contact line remains pinned on the roll surface. While this may be reasonable over a short enough period of time for gravure coating, it is certainly not the case in gravure printing, where the contact line motion is key in achieving complete cavity emptying.

1.2.3 Gravure printing

Work related to printing is often focused on developing an understanding of how drops of liquid move from one surface to another, with an emphasis on how this transfer is altered by process conditions, such as the fluid properties or the surface geometry. A common assumption in much of this research is therefore to examine the dynamics of a single drop of fluid, instead of the more complex network of cavities and grooves that is actually present on the surface of a gravure roll.

As a first approximation in understanding the detailed fluid mechanics of gravure printing, Yin and Kumar (2005) used a lubrication model to study the effect of a deformable substrate on the liquid within a trapezoidal cavity. Their results compared well to a two-dimensional finite element study by the same authors (Yin and Kumar, 2006b), indicating that despite rapid changes in the vertical length scale at the cavity walls, lubrication analysis remains a useful tool for studying gravure. The work of Yin and Kumar (2005, 2006b) shows that when viscous forces are large relative to the web elasticity/tension, large web deformations are observed that can significantly alter the flow profile within the cavity. In this work, the effect of web stiffness is implicitly ignored through the use of a one-dimensional spring model for the substrate, though it was later shown by Hewson et al. (2009) that web stiffness is the more important factor in the typical operating range for gravure. However, none of these studies include the effect of the liquid/gas interface, and they are therefore unable to make quantitative conclusions about the transfer of liquid from the cavities.

Another simplified approach is to consider a single meniscus being dragged over a 2D-planar groove by a moving web, which is similar to cavity filling for nano-imprint lithography (Reddy et al., 2005; Chauhan et al., 2009; Marín et al., 2010). Using the finite element method, Powell et al. (2000) found that the limiting factor in cavity emptying was the impingement of the free surface with the cavity corner. This implies that the dewetting speed of the contact line must be faster than the rate at which the meniscus is drawn across the cavity. Emptying can therefore be improved by either making the cavity less wettable, or by increasing its width relative to its depth. This was confirmed through flow visualization experiments by Yin and Kumar (2006a). Hoda and Kumar (2008) studied a similar system using the boundary integral method, and found that while cavities could be completely emptied when the web velocity has both shear and extensional components, they could not be emptied by either component alone.

While the planar geometries discussed in the previous paragraph are relevant to trihelical

gravure, the typical cavity height, width, and depth are often of the same order of magnitude in gravure printing (see figure 1.4). In this case, the liquid will form a cylindrical thread away from the cavity due to surface tension, leading to a nearly axisymmetric feature. This allows one to approximate the drop as a cylindrical liquid bridge, a system which has been studied extensively in the literature (see for example Gaudet et al., 1996; Zhang et al., 1996; Yao and McKinley, 1998, as well as chapter 2). In these studies, it is common to assume that the contact lines are pinned in place, which greatly simplifies both experimental and theoretical analyses. However, this is not the case in most printing processes, where the motion of the contact lines is required for the transfer of liquid to be optimized. Therefore, to capture the dynamics of printing, one must consider the motion of the contact lines.

Despite this importance, the role of surface wettability has until recently been studied only in liquid bridge systems at low capillary numbers (Pepin et al., 2000; Darhuber et al., 2001; Cai and Bhushan, 2008; De Souza et al., 2008). However, in realistic printing processes both viscous and inertial forces can become significant (see chapters 2 and 3 for scaling analyses), and therefore must be included in any realistic model. Powell et al. (2002) began to address this, though Panditaratne (2003) was the first to perform a systematic study of surface wettability on liquid bridge dynamics. Huang et al. (2008) used the volume-of-fluid method to model liquid bridges stretched between either two flat plates or a flat plate and a cavity. However, their work on cavities was restricted to low capillary numbers ($\sim O(10^{-2})$), which we show in chapter 2 produces significantly different breakup behavior than higher capillary numbers.

Efforts to visualize the liquid transfer process are challenging because of the small lengths and high speeds involved in most printing processes. Gravure is especially problematic because the gravure roll is opaque, making it difficult to observe the fluid within the cavity. Therefore, most of the experimental studies performed have been restricted to liquid bridges between flat surfaces (Chadov and Yakhnin, 1979; Yakhnin and Chadov, 1983; Gupta et al., 2007; Huang et al., 2008). Two notable exceptions to this are the work of Yin and Kumar (2006a), discussed earlier, and of Chuang et al. (2008), who studied the emptying of gravure cavities onto a cylindrical roll. They found that networks of cavities were inherently more difficult to empty due to hydrodynamic interaction between the cavities. This is an extremely important point, as truly isolated cavities are rarely encountered, and it is therefore vital to understand this interaction to design optimal cavity networks for printing.

1.3 Thesis overview

While the work presented in section 1.2 provides a foundation of knowledge for both gravure coating and printing, there is still much that is not well-understood. In particular, the mechanisms through which system parameters such as inertia, wettability, and cavity shape alter breakup and liquid transfer remain unclear. Therefore, it is difficult to extend results

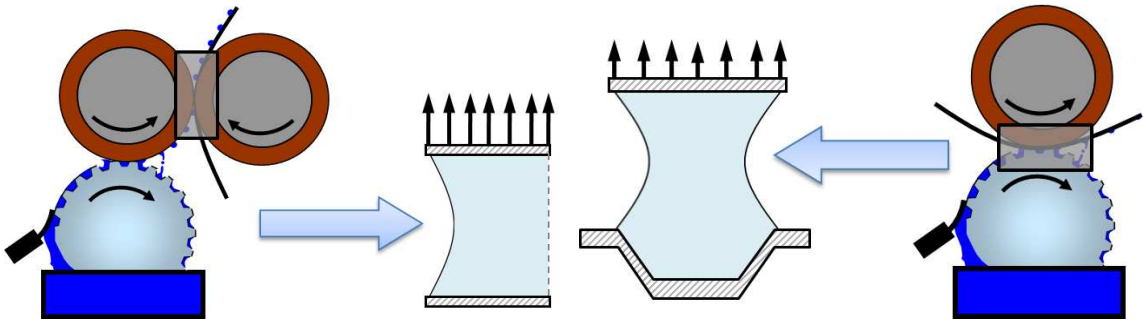

Figure 1.7: Schematics of the two types of problems studied in this thesis. (a) Offset printing between two cylinders, using gravure offset as an example. (b) Gravure printing.

from a specific study on gravure to a more general system.

In an attempt to elucidate these mechanisms, we focus on the dynamics of a single liquid bridge in one of two different types of geometries. In the first case, we consider a liquid bridge between two flat plates. This is a model for any type of offset printing, where a pattern is transferred onto a rubber roll before being printed on the web. Figure 1.7(a) depicts gravure offset printing, though lithographic (or flexographic) offset could just as easily have been used as a demonstration. The second geometry that we consider is stretching between a flat plate and a trapezoidal cavity, depicted in figure 1.7(b), as a model for gravure printing.

In this thesis we make several additional approximations. First, we assume that the characteristic size of the printed features are much smaller than the roll radii, allowing the roll curvature to be ignored. Second, with the exception of chapter 4, we assume that the shear rates are small so that the plates undergo a purely extensional motion. This is a reasonable approximation so long as the rolls have similar sizes and rotational rates, so that they are not moving relative to each other. Third, we assume that the extensional velocity remains constant during stretching to simplify analysis of our results. Finally, with the exception of chapter 4, we assume that the bridge remains axisymmetric during stretching.

The remaining chapters in this thesis each consist of the study of a model problem used to isolate a specific physical phenomena (*i.e.*, wettability, inertia, etc.) relevant to industrial printing processes. Each chapter is described in further detail in the following paragraphs.

1.3.1 Stretching liquid brides in Stokes flow

As we have repeatedly stressed in this chapter, a primary motivation for further study of printing processes is the desire to print small-scale features, typically 10 μm or less. These small length scales, combined with stretching speeds on the order of cm/s allow us to neglect the inertial terms in the Navier-Stokes equations, greatly simplifying analysis. In chapter 2 we solve Stokes equations for an axisymmetric stretching liquid bridge with moving contact

lines, and evaluate the effect of surface tension, viscosity, wettability, and cavity geometry on the dynamics of breakup and the transfer of liquid from one surface to the other. We also compare our results to the Rayleigh-Plateau stability limit for static cylinders of fluids, to isolate the role that viscosity plays in modifying breakup.

1.3.2 Stretching liquid bridges with inertia

While current interest is generally in producing small-scale features, there are many situations where printed patterns are on the order of hundreds of microns (Mäkelä et al., 2005; Pudas et al., 2005). At these sizes inertial forces can become significant, resulting in nonlinear effects that produce substantial departures from the bridge behavior observed in Stokes flow. In chapter 3 we solve the Navier-Stokes equations for an axisymmetric liquid bridge, and evaluate the effect of inertia, wettability, and cavity shape on the dynamics of breakup and the transfer of liquid from one surface to the other. In particular, we consider the creation of secondary drops, known as satellites, to better understand how the fluid and geometric parameters can be used to suppress their formation.

1.3.3 Stretching liquid bridges in three dimensions

In chapters 2 and 3 we consider cylindrical liquid bridges, allowing the use of the 2D-axisymmetric Navier-Stokes equations. However, in real printing processes the stretching motion may combine extension with either a shear or rotational component if the roll radii/speeds are not properly matched. Additionally, the liquid bridge need not be cylindrical, but can instead have a non-axisymmetric shape. To account for these more complex situations, we solve the three-dimensional Navier-Stokes equations in chapter 4 using a novel extension of the two-dimensional finite element technique presented in chapters 2 and 3.

1.3.4 Stretching liquid bridges with bubbles

Finally, the entrapment of small air bubbles in gravure cavities is known to lead to a defect known as spackle, which can significantly reduce the amount of liquid transferred. In chapter 5 we use flow visualization to understand the dynamics of these bubbles during stretching at low capillary numbers. In particular, we consider the effect of wettability on the motion of the bubble from one plate to the other.

CHAPTER 2

Stretching liquid bridges in Stokes flow

The dynamics of liquid bridges are relevant to a wide variety of applications including high-speed printing, extensional rheometry, and floating-zone crystallization. Although many studies assume that the contact lines of a bridge are pinned, this is not the case for printing processes such as gravure, lithography, and microcontacting. To address this issue, we use the Galerkin/finite element method to study the stretching of a finite volume of Newtonian liquid confined between two flat plates, one of which is stationary and the other moving. The steady Stokes equations are solved, with time dependence entering the problem through the kinematic boundary condition. The contact lines are allowed to slip, and we evaluate the effect of the capillary number and contact angle on the amount of liquid transferred to the moving plate. At fixed capillary number, liquid transfer to the moving plate is found to increase as the contact angle on the stationary plate increases relative to that on the moving plate. When the contact angle is fixed and the capillary number is increased, the liquid transfer improves if the stationary plate is wetting, but worsens if it is non-wetting. The presence of a cavity on the stationary plate significantly affects the contact line motion, often causing pinning along the cavity wall. In these cases, liquid transfer is controlled primarily by the cavity shape, suggesting that the effects of surface topography dominate over those of surface wettability. At low capillary numbers, bridge breakup can be understood in terms of the Rayleigh-Plateau stability limit, regardless of the combination of contact angles or the plate geometry. At higher capillary numbers, the bridge is able to stretch beyond this limit, though the deviation from this limit appears to depend on contact line pinning, and not directly on the combination of contact angles or the plate geometry.[1]

[1]This chapter is reproduced with minor modifications from S. Dodds, M. S. Carvalho, and S. Kumar. "Stretching and Slipping of Liquid Bridges near Plates and Cavities", *Physics of Fluids*, **21** (2009) 092103

2.1 Introduction

The breakup of liquid columns has been studied extensively for over one hundred years, dating back to pioneering works by Lord Rayleigh (1878) and Plateau (1863). This topic has generated so much interest because of its relevance to a diverse range of practical applications, such as oil recovery (Gaudet et al., 1996), rheological measurements (Yao and McKinley, 1998), high-purity crystallization (Meseguer, 1983), and industrial printing processes (Powell et al., 2002). An equally important motivation for the study of the breakup of liquid columns is the rich mathematical and physical nature of the problem, as discussed by Eggers (1997) and Eggers and Villermaux (2008).

The breakup of liquid columns is normally studied using one of two experimental systems: a liquid jet ejected from a nozzle and subjected to controlled perturbations, or by stretching a mass of liquid between two solid plates, a setup known as a liquid bridge. These two systems are often modelled using a periodic (repeating) domain for the jet, or an axisymmetric, cylindrical column of liquid with pinned contact lines between two flat, parallel plates for the liquid bridge. However, by pinning the contact lines the effect of the wettability of either plate is ignored, so it is not possible to generalize the results currently in the literature to systems with a liquid bridge between two chemically different surfaces. These kinds of systems are observed in a variety of places, including the agglomeration of particles (Pepin et al., 2000), and industrial printing processes such as gravure, flexography and lithography. In addition, geometric variations on the surfaces could affect the dynamics of the bridge breakup by altering the contact line speed, and so represent another important area of study. The goal of this chapter is to address these issues using a finite element model (FEM) of an axisymmetric liquid bridge, including both contact line slip and plates with cavities.

There have been many studies on the stability and breakup dynamics of static liquid bridges (Lord Rayleigh, 1878; Plateau, 1863; Gillette and Dyson, 1971; Rivas and Meseguer, 1984; Tjahjadi et al., 1992), including the famous Rayleigh-Plateau stability limit (Plateau, 1863; Lord Rayleigh, 1878), which states that the length of a static liquid column cannot be greater than its circumference. These studies motivated work on stretching jets by Tomotika (1936), who used a linear stability analysis to show that the stretching of a viscous jet also stretches any perturbations, creating a slower growth rate than is predicted for static jets. Tomotika's analysis laid the groundwork for many later studies such as those of Mikami et al. (1975), who improved on Tomotika's model and included experimental results, and Frankel and Weihs, who studied the stability of stretching liquid jets in the inviscid flow limit (Frankel and Weihs, 1985), as well as solving the full Navier-Stokes equations (Frankel and Weihs, 1987).

Work on stretching liquid bridges, however, did not become popular until the early 1990s, and was initially motivated by a necessity for accurate measurement of the extensional viscosity of low viscosity liquids. First proposed by Sridhar et al. (1991), the filament

stretching rheometer stretches a drop of liquid while tracking the radius of the thinnest cross-section of the liquid bridge. Then, by performing a stress balance, the extensional viscosity can be calculated. This system was modeled by Shipman et al. (1991) using the finite element method, though they were limited by a computational model which required a fixed axial length. Therefore, instead of modelling the entire bridge, they modeled only the regions near the end-plates and strongly imposed the theoretical extensional stress that the bridge should be experiencing as an outflow boundary condition. Despite this serious limitation, they achieved reasonable agreement with the experimental results presented by Sridhar et al. (1991).

A later study by Gaudet et al. (1996) used the boundary integral technique to model the extension of Newtonian liquid bridges in Stokes flow, and found that the bridges can be stretched well beyond their static stability limits. This effect is greater at high capillary numbers, indicating that viscosity works to stabilize the bridge as it is stretched. These results are complemented by FEM computations using a 1D slender jet approximation by Zhang et al. (1996), who were able to obtain very good agreement between their computational and experimental results. They were also able to predict the formation of satellite drops at a moderate Ohnesorge number, which represents a ratio of viscous to surface tension forces, but found that the inclusion of gravity in their model could prevent satellite drops if the ratio of gravitational forces to surface tension forces was high enough.

The mechanism of jet or bridge breakup is the rising capillary pressure created as the liquid column thins. This thinning produces a small azimuthal radius of curvature, which creates a large capillary pressure that drives liquid away from the thinning region, accelerating breakup. The breakup event has been shown to produce self-similar interface profiles in the vicinity of the breakup location for a wide variety of flow regimes, such as when surface tension and viscosity are in balance and inertia is ignored (Papageorgiou, 1995), or when surface tension, viscosity and inertia are all in balance (Eggers, 1993), as well as for non-Newtonian liquids (Renardy, 2002; Doshi et al., 2003; Renardy and Renardy, 2004).

A large body of work has been built upon these earlier studies, mostly examining non-Newtonian or surfactant effects. Yao and McKinley (1998) studied the extension of Oldroyd-B fluids using a 2D FEM model, and found that the bridge strain-hardens during stretching, and therefore thins uniformly along its mid-section, *i.e.* the bridge remains cylindrical far away from the end-plates. Therefore, pinch-off occurs close to the end plates, producing a large satellite drop. This is in contrast to viscous Newtonian liquids, which do not thin evenly, but instead break at the mid-point of the bridge. Yildirim and Basaran (2001) used a 1D FEM model to study shear thinning liquids, and found a decrease in the bridge length at breakup because of the low viscosities produced in the high-shear neck region. This results in a local capillary number that is lower than in the bulk liquid, which leads to faster breakup.

Ambravaneswaran and Basaran (1999) studied the effect an insoluble monolayer of sur-

factant has on breakup using a 1D FEM model. They found that at high Péclet numbers the surfactant is convected away from the neck, resulting in a surface tension gradient that drives liquid back into the neck, and thus stabilizes the bridge. However, for high extensional velocities the neck thins too quickly for the surfactant to redistribute on the surface, and so no benefit from the surfactant is observed. These results were extended by Liao et al. (2006) to include experimental validation, as well as gravitational effects using a 2D FEM model.

A common feature of the works reviewed so far is the assumption that the contact lines remain pinned as the bridge is stretched. While this may be the case in some applications where the contact line can be easily pinned to geometrical features, such as in extensional rheology, it is not obvious that the contact lines will pin during the printing of liquids. In fact, when printing it is *desirable* for the contact lines to slip, so that the transfer of liquid from one surface to the other can be maximized. However, there has been relatively little research into the effect that moving contact lines might have on liquid transfer during the stretching of a mass of liquid. Motivated by the gravure printing process, Powell et al. (2000) performed FEM computations on an interface being dragged through a 2D planar square cavity by a moving plate, and found that incomplete liquid transfer would occur if the trailing free surface reached the upper cavity corner before the contact line. These results were confirmed experimentally by Yin and Kumar (2006a). Reddy et al. (2005) used FEM computations to show a similar trend for the filling of a square cavity.

Hoda and Kumar (2008) extended the results of Powell et al. (2000) to explore a larger parameter space, as well as to study the effect of extensional motion on liquid transfer. They found that complete liquid transfer could not be obtained with shear motion alone under the parameter set studied, but could be achieved if shear and extension were used simultaneously. However, by assuming a 2D planar geometry, neither Powell et al. (2000) nor Hoda and Kumar (2008) were able to study 3D effects. One such effect is the azimuthal radius of curvature, which is responsible for the high pressures developed in the bridge as it thins, accelerating breakup. Powell et al. (2002) began to address this issue, using a 2D-axisymmetric FEM model to study the removal of liquid from trapezoidal cavities, though they did not perform a systematic study of the effect of surface wettability or of cavity shape. Huang et al. (2008) used a volume-of-fluid method to track the shape of a 2D planar liquid bridge being stretched between a flat surface and a trapezoidal cavity. They studied a variety of contact angles and cavity shapes, and so addressed some of the limitations of the study by Powell et al. (2002), though by choosing a planar geometry they do not account for the effect of the azimuthal radius of curvature. In addition, the results presented on the emptying of gravure cavities were only for a capillary number of 0.01, which as we will show in section 2.4, is too low to see the effect of cavity shape and contact angle.

Schwartz et al. (1998) and Schwartz (2002) used a two-dimensional lubrication model to study the emptying of networks of cells during gravure coating. However, they treated the

contact line as being pinned, and so were unable to study the effects of surface wettability on liquid transfer. Therefore, further investigations incorporating moving contact lines are needed to improve our understanding of liquid transfer in gravure printing.

Finally, there have also been contributions to the study of liquid bridges that attempt to understand the adhesive forces created when a liquid is trapped between solid particles, *e.g.* grains of sand, dating back to early work by Orr et al. (1975), who solved the Young-Laplace equation for the interface shape of static liquid bridges between spherical and flat particles in terms of elliptic integrals. Orr et al. (1975) laid the groundwork for many future studies which utilized the Young-Laplace equation, along with mass conservation, to obtain interface profiles and adhesive forces for stretching liquid bridges between spherical particles. Of interest to the current discussion is a body of work which attempts to account for the effect that contact line slip has on adhesion (Pepin et al., 2000; Urso et al., 2002; Cai and Bhushan, 2008; De Souza et al., 2008; Vagharchakian et al., 2009; Davis and Frenkel, 1992). However, these works are restricted by the presupposition of an equilibrium interface shape, which implies a pseudo-steady-state stretching process. While this assumption should be valid in the low capillary number limit, at more moderate capillary numbers one would expect that the fluid mechanics of the system play an important role in determining the interface shape.

To address some of the issues presented in this section, we set forth a computational model to study the transfer of liquid from a stationary to a moving plate using an axisymmetric liquid bridge as a model system (Section 2.2). The Galerkin finite element method is used to solve the governing equations, and elliptic mesh generation is used to track the position of the interface as it evolves in time. To account for differences in surface wettability between the two plates, we allow the contact line to slip along the plates with a constant contact angle, while imposing a Navier slip law to relieve the stress singularity that develops near the moving contact line. The steady Stokes equations are solved, with time dependence entering the problem through the kinematic boundary condition. We begin by examining the effect of contact line slip on liquid bridges between two flat plates by varying the contact angles on either plate, as well as the capillary number (Section 2.3). Our goal is to characterize how changes in surface wettability and surface tension affect the amount of liquid found on either plate after breakup. We then replace one of the flat plates with a trapezoidal cavity, to study how geometric features alter the breakup dynamics of the liquid bridge (Section 2.4). When our results are compared to the Rayleigh-Plateau limit, we see good agreement at a low capillary number, even though the liquid-air interface in our computations is highly curved (Section 2.5). Finally, we end by summarizing and discussing the key conclusions presented in this work (Section 2.6).

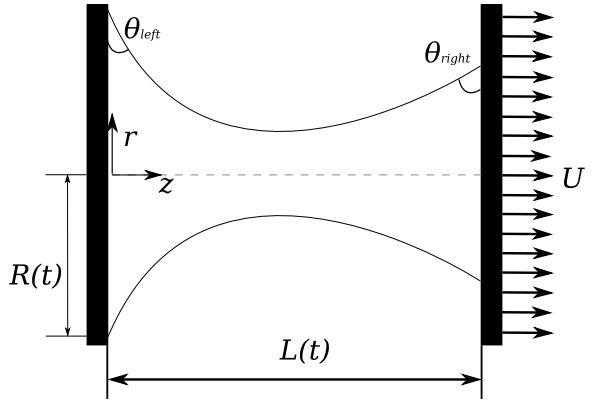

Figure 2.1: A schematic of a liquid bridge between flat plates.

2.2 Problem formulation

2.2.1 Governing equations

We consider an axisymmetric liquid bridge of an incompressible Newtonian liquid with a constant volume V, viscosity μ, surface tension σ, and density ρ (see figure 2.1). The viscosity of the fluid outside the bridge is taken to be small relative to that within the bridge. Therefore, the outer phase is taken as a passive gas and its dynamics are neglected. While it is important to consider the outer fluid to obtain an accurate representation of the fluid interface during the late stages of breakup (Lister and Stone, 1998), the shape of the large drops resting on either plate will be unaffected by these late-time dynamics. Therefore, we assume that ignoring the outer fluid will have a negligible effect on the amount of liquid resting on either plate after breakup, which is the variable of interest in this study.

For this problem, length is scaled with the initial liquid bridge radius R, velocity with the constant extensional velocity U, time with R/U, and pressure with $\mu U/R$. We can define a Reynolds number $Re = \rho UR/\mu$ and a Stokes number $St = \rho g R^2/\mu U$, where g is the acceleration due to gravity, such that the Navier-Stokes equations can be written as:

$$Re\frac{D\mathbf{v}}{Dt} = -\nabla P + \nabla^2\mathbf{v} + St\hat{\mathbf{g}}, \tag{2.1}$$

$$\nabla \cdot \mathbf{v} = 0. \tag{2.2}$$

where $\mathbf{v}$ is the velocity, P is the pressure, and $\hat{\mathbf{g}}$ is a unit vector in the direction of the gravitational field.

In many printing processes the goal is to produce small features, on the order of 10 μm. The liquid viscosity can range anywhere from 1-100 cp. The extensional velocity experienced by the liquid is on the order of 1 - 10 cm/s, and so estimates for the range of Reynolds and Stokes numbers during printing are $Re \approx 0.001 - 1$ and $St \approx 10^{-5} - 10^{-1}$. While inertial effects can be important at the upper range of the listed operating conditions,

they can generally be ignored. Therefore, we will neglect the effects of inertia and gravity in equation (2.1), and will solve equation (2.2) along with the Stokes equations:

$$\nabla P = \nabla^2 \mathbf{v}. \tag{2.3}$$

At the gas-liquid interface, we need to satisfy kinematic and interfacial stress boundary conditions:

$$\mathbf{n} \cdot \mathbf{v} = 0, \tag{2.4}$$

$$\mathbf{n} \cdot \mathbf{T} = -\frac{\kappa}{Ca}\mathbf{n}, \tag{2.5}$$

where $\mathbf{n}$ is the outward pointing normal at the interface, $\mathbf{T}$ is the total stress tensor, $Ca = \mu U/\sigma$ is the capillary number, and κ is the curvature, which can be calculated by taking the surface divergence of the normal vector:

$$\kappa = -\nabla_s \cdot \mathbf{n}, \tag{2.6}$$

where $\nabla_s = (\mathbf{I} - \mathbf{nn}) \cdot \nabla$ is the surface gradient operator, and $\mathbf{I}$ is the identity tensor. It should be noted that when writing equation (2.5), we have assumed that the pressure of the ambient fluid surrounding the liquid bridge is zero. Using the operating conditions listed above, and a surface tension of 20-70 mN/m, an estimated range for the capillary number experienced during printing is $Ca \approx 10^{-4} - 0.5$.

At the two solid surfaces we apply no-slip and no-penetration conditions:

$$\mathbf{t} \cdot \mathbf{v} = 0, \text{at } z = 0, L(t), \tag{2.7}$$

$$\mathbf{n} \cdot \mathbf{v} = \begin{cases} 0 & \text{for } z = 0, \\ U & \text{for } z = L(t). \end{cases} \tag{2.8}$$

An important point to note is that we will observe the same results pulling the two plates apart at $\pm U/2$ as we will using equation (2.8) because we can perform a Galilean transformation to move the reference frame for the system (Papageorgiou, 1995). Because we are studying axisymmetric cylindrical liquid bridges, we must impose symmetry boundary conditions along the bridge axis:

$$\mathbf{t} \cdot (\mathbf{n} \cdot \mathbf{T}) = 0, \tag{2.9}$$

$$\mathbf{n} \cdot \mathbf{v} = 0, \tag{2.10}$$

where $\mathbf{t}$ and $\mathbf{n}$ are the tangent and normal vectors to the symmetry line.

Finally, as a key objective of this work is to evaluate the effect of chemically different surfaces on the breakup behaviour of liquid bridges, we must allow the contact lines to slip along the two surfaces. However, this produces a well known singularity in the stress tensor as the contact line is approached (Huh and Scriven, 1971). To relieve this singularity, we

replace equation (2.7) at the contact line with a Navier slip boundary condition and force the liquid to maintain a constant contact angle with the solid surface:

$$\mathbf{t}_{wall} \cdot (\mathbf{n}_{wall} \cdot \mathbf{T}) = \frac{1}{\beta} \mathbf{t}_{wall} \cdot \mathbf{v}, \tag{2.11}$$

$$\mathbf{n}_{wall} \cdot \mathbf{n}_{interface} = cos\,(\theta)\,, \tag{2.12}$$

where β is the slip coefficient. In the FEM discretization of the solution, equations (2.11) and (2.12) are applied only at the node located on the contact line, *i.e.* the slip length is taken to be less than the length of an element, and the value of β was taken to be 10^{10}, implying that equation (2.11) represents a zero-stress condition. However, the results were found to be independent of β down to $\beta = 0.1$, indicating that the slip coefficient does not have a significant effect on the bulk fluid motion.

It is important to note that equation (2.12) imposes a constant contact angle on both plates, regardless of the wetting velocity. This approach is technically only valid for small wetting velocities, whereas typical contact line velocities observed during computation were on the order of -0.5 dimensionless units, which corresponds to dimensional velocities on the order of 0.5-5 cm/s. While more realistic models exist which account for the dependence of the contact angle on the slip velocity (Blake, 2006), one would expect the qualitative trends predicted by these models to be the same as ours. Therefore, we assume that despite utilizing such a simplistic slip model, we will capture the essential features of stretching liquid bridges with moving contact lines.

2.2.2 Numerical methods

To solve equations (2.2) and (2.3), subject to boundary conditions (2.4) through (2.12), we use the Galerkin finite element method. The moving interface is tracked using elliptic mesh generation, which utilizes a set of elliptic partial differential equations to map the physical coordinates (r, z) onto a square computational domain with coordinates (ξ, η):

$$\begin{aligned} \nabla \cdot (D_\xi \nabla \xi) &= 0, \\ \nabla \cdot (D_\eta \nabla \eta) &= 0, \end{aligned} \tag{2.13}$$

where D_ξ and D_η can be thought of as mesh diffusion coefficients, and are used to specify the spacing of the elements within the physical domain. The details of this method are provided in Christodoulou et al. (1997), and so are not repeated here. Because this is a moving mesh method, we must subtract the effect of mesh convection from any calculated time derivatives, *i.e.*

$$\left(\frac{\partial \mathbf{v}}{\partial t}\right)_{actual} = \left(\frac{\partial \mathbf{v}}{\partial t}\right)_{node} - \left(\frac{\partial \mathbf{x}}{\partial t}\right)_{node} \cdot \nabla \mathbf{v}. \tag{2.14}$$

Time integration is performed using the second-order adaptive time-stepping algorithm outlined by Gresho et al. (1980). To avoid spurious oscillations in the solution, the first three time steps are performed using a first-order forward difference predictor and a first-order backward difference corrector, all with a fixed time step. After this, the trapezoid rule is used as a corrector with a second-order Adams-Bashforth predictor to integrate our system of equations, as well as to provide an estimate of the local truncation error in the integration. The time step is then adjusted such that the predicted error at the next time step is less than a prescribed tolerance, taken here to be 2×10^{-4}. The resulting non-linear system of equations is then solved using Newton's method and LU-decomposition to obtain values for the unknown coefficients in the FEM approximation of the solution. Normally, two to three Newton iterations were required to obtain convergence at each time step.

Because the length of the liquid bridge increases with time, the elements often become stretched during computations. Therefore, it is occasionally necessary to add additional elements to the domain. New columns of elements are distributed evenly throughout the liquid bridge when needed, and the position, velocity and pressure at each node in the refined mesh are interpolated from the solution with the old mesh. The time stepping is then re-started, using a fixed time step size with a first-order backward Euler method for the first three time steps, after which the trapezoid rule with adaptive time stepping is used, as explained earlier in this section. The remeshing procedure was not required more than three times for each liquid bridge computation. It should be noted that, during computation, we track the total volume of liquid in the bridge. To ensure that no mass is gained/lost during remeshing, we calculate the percent deviation of the liquid bridge volume using $100 * (V_{max} - V_{min})/V_{ini}$, where V_{max} and V_{min} are the maximum and minimum volumes of the bridge during stretching, and V_{ini} is the initial bridge volume. This value was generally on the order of 0.01%, and if it was greater than 0.1% the results were deemed inaccurate, and the run was repeated with a refined mesh/time step.

As the bridge nears breakup, thin threads of liquid connect two primary drops resting on either plate. In these threads the elements become extremely elongated and the numerical algorithm eventually fails, often at a dimensionless thread radius of roughly 10^{-3}. At this point the computation is considered to be complete. While this large mesh deformation will certainly introduce error into the solution, it occurs only during the very late stages of breakup. Therefore, it is not expected that the final shape of the interface on the scale of the primary drops will be significantly affected by the error in the connecting thread, which is therefore ignored. Indeed, we generally observe less than 1% variation in the final breakup time and position of the contact lines when doubling the number of elements in the axial direction.

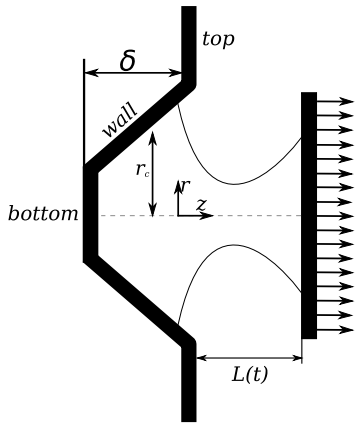

Figure 2.2: A schematic of the trapezoidal cavity used in this study.

2.2.3 Geometry

For the computations involving flat plates, the initial condition used is a cylindrical liquid bridge with a length equal to its diameter. This value was chosen for easy comparison to results already in the literature (Gaudet et al., 1996; Zhang et al., 1996), and not with any particular application in mind. However, we do not expect a different initial condition, such as a larger aspect ratio or an equilibrium interface shape, to qualitatively affect any predicted trends between the wettability of the plates and the amount of liquid transferred during stretching. Therefore, we will proceed with this initial condition to outline the physics of stretching liquid bridges with moving contact lines. The computational mesh used for these runs contained 16 elements in the radial direction and 70 elements in the axial direction. For these runs, remeshing was not generally required.

For the computations involving plates with cavities, we chose an axisymmetric trapezoidal cavity, shown in figure 2.2, as a model system. This particular geometry was selected because it allows us to easily evaluate the effect of a variety of topographical features, such as corners and inclined surfaces, on the flow field and liquid transfer. Additionally, this geometry is relevant to the gravure printing process (Powell et al., 2002; Yin and Kumar, 2006a; Hoda and Kumar, 2008), which uses micron-sized cavities to deliver liquid to a substrate. Despite being commonly used in industry, gravure is not a well-understood technology, so a theoretical study of the removal of liquid from trapezoidal cavities could help improve our understanding of the gravure printing process.

The cavities are modelled using a hyperbolic tangent function to define the left (stationary) plate:

$$z = \frac{1}{2}\delta\left(1 - \tanh\left(\frac{r - r_c}{r_s}\right)\right), \tag{2.15}$$

where r and z are the radial and axial positions along the wall, δ is the depth of the cavity, r_c corresponds to the distance from the axis of symmetry to the centre of the wall (see figure

2.2), and r_s is related to the curvature of the corners and to the steepness of the cavity wall. Sharp corners and steep walls are obtained by using small values of r_s. The length scales presented in this chapter are non-dimensionalized using the depth of the cavity, which is roughly 50μm for most printing processes.

Before stretching the liquid bridge, we first find a static meniscus shape by solving the system of equations (2.2)-(2.12) with equation (2.8) replaced by the condition

$$\mathbf{n} \cdot \mathbf{v} = 0 \text{ for } z = 0, L. \tag{2.16}$$

This equilibrium bridge shape is then used as an initial condition for the computations involving stretching bridges. For these computations, an initial mesh with 35 elements in the radial direction and 30 elements in the axial direction was used.

2.3 Results: Flat plates

We first validated our code with results presented by Gaudet et al. (1996), who used the boundary integral method to model the stretching of a Newtonian liquid bridge with no inertia and pinned contact lines. For these computations, equations (2.11) and (2.12) were replaced with the condition that at $z = 0$ and $L(t)$, the contact lines are fixed at $r = 1$. We compared the predicted interface shapes from our results to those presented in figures 6 and 10 of Gaudet et al. (1996) and found excellent agreement. An important observation is that, because we have assumed Stokes flow and the contact lines are pinned in place, there is nothing in the governing equations to differentiate the liquid adjacent to one plate from the liquid adjacent to the other plate. Therefore, the breakup is always symmetric about the mid-point of the bridge, and exactly half of the liquid will rest on each plate after breakup.

If one of the contact lines is allowed to slip while the other remains pinned in place, we can begin to evaluate how motion of the contact line might alter the breakup of the bridge. Physically, this corresponds to the stretching of a liquid bridge between a surface with a surface discontinuity at which the contact line will pin readily, and a perfectly smooth surface. We present results for the case where the contact line on the left plate is unpinned. However, if we instead allow the right contact line to slip while pinning the left contact line, we would observe the mirror image of the results presented here.

Figure 2.3 shows the evolution of the interface shape at $Ca = 0.1$, and a contact angle on the left plate $\theta_{left} = 60^\circ$. While the bridge initially has a cylindrical shape, it quickly evolves to have a shape which is asymmetric about the mid-point of the bridge, leading to drops of different size resting on either plate after breakup. The drop on the left plate becomes larger as the bridge is stretched because, with a contact angle of 60° the liquid will spread over the plate. If we repeat these computations for different capillary numbers, we can probe the effect of surface tension relative to viscosity. In figure 2.4(a) we have

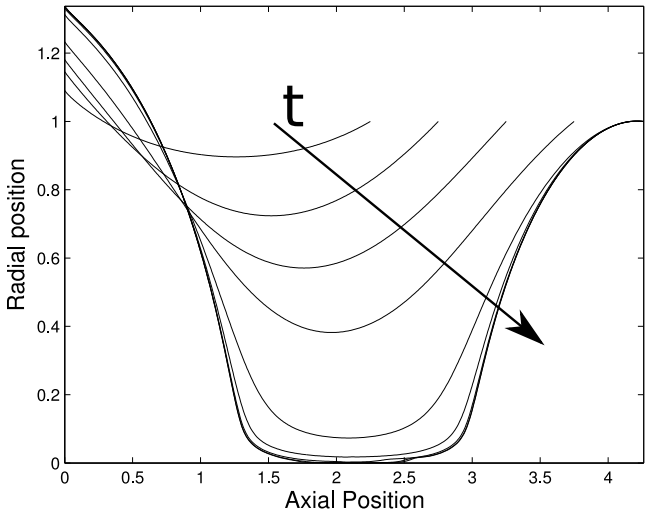

Figure 2.3: Interface shapes at various times for $Ca = 0.1$, and $\theta_{left} = 60^\circ$

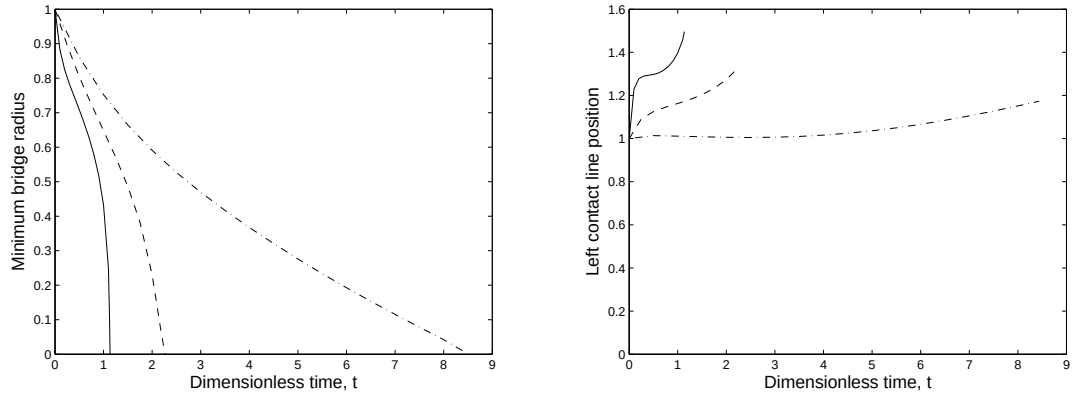

(a) (b)

Figure 2.4: A comparison of results obtained at $Ca = 1$, 0.1 and 0.01 for $\theta_{left} = 60^\circ$, plotting (a) the minimum radius of the liquid bridge and (b) the position of the left contact line vs. time. The runs presented are for $Ca = 0.01$ (—), $Ca = 0.1$ (−−), and $Ca = 1$ (− · −).

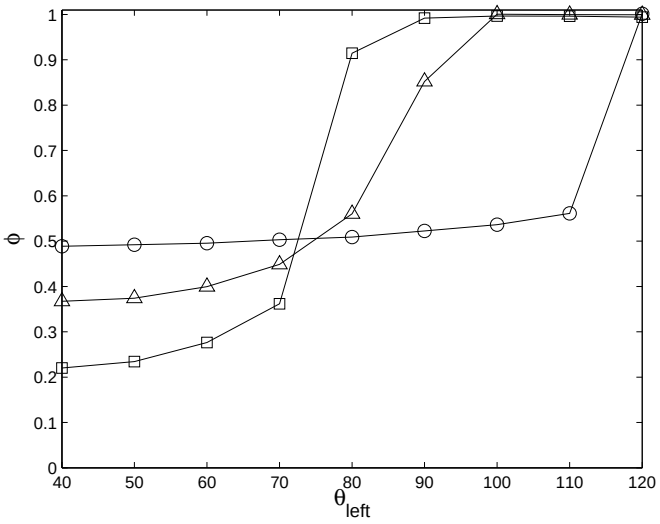

Figure 2.5: The fraction of liquid resting on the right plate after breakup vs. the contact angle on the left plate. The runs are for $Ca = 0.01$ (□), $Ca = 0.1$ (△) and $Ca = 1$ (○),

shown the evolution of the minimum radius of the liquid bridge (*i.e.* the thinnest part of the bridge) with time at $Ca = 0.01$, 0.1, and 1. As Ca rises, the bridge is able to stretch to greater lengths. The same trend was observed when both contact lines were pinned, and is shown in figure 16 of Gaudet et al. (1996). In figure 2.4(b), we have shown the position of the left (moving) contact line vs. time at the same conditions as in figure 2.4(a). At $Ca = 1$, the relatively low strength of surface tension allows the contact line to effectively pin in place, moving only $\sim 15\%$ from its initial position and resulting in breakup that is nearly symmetric about the midpoint of the bridge. This is explained by noting that a higher capillary number allows for a greater amount of interface deformation, which in turn allows the interface to compensate for the contact angle boundary condition by deforming near the contact line, instead of slipping along the plate. However, as the capillary number is decreased and surface tension is made more important, the contact line slips a great deal along the plate, moving $\sim 50\%$ from its initial position for $Ca = 0.01$. This is because at a low capillary number, the interface is unable to deform enough to allow the contact line to maintain the same angle and position.

Figure 2.5 shows the fraction of liquid in the right-hand drop after breakup, ϕ, as a function of θ_{left} at $Ca = 0.01$, 0.1, and 1. The amount of liquid transferred to the right plate falls with increasing θ_{left} for all three capillary numbers studied. This is an intuitive result because as the left plate becomes more wettable, liquid is drawn towards that plate. This leads to a larger drop on the left plate than the right plate after breakup. If we consider a fixed contact angle and examine the effect of the capillary number, we see that the relationship between ϕ, Ca, and θ_{left} is more complex. If the contact angle of the left plate is high, then as the capillary number falls more liquid is found on the right plate after

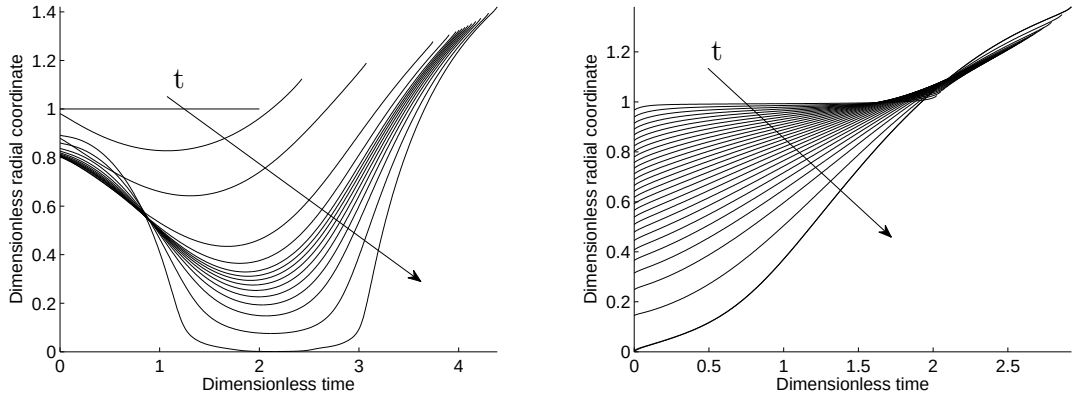

Figure 2.6: Liquid bridge shapes at various times for $Ca = 0.1$, $\theta_{right} = 60°$, and (a) $\theta_{left} = 80°$ (b) $\theta_{left} = 120°$.

breakup than on the left plate. This is because in the case of a less-wettable left plate, surface tension forces aide in moving liquid to the right, and thus work to increase liquid transfer. Therefore, if we decrease Ca we see an increase in ϕ. If we instead examine a low contact angle, the liquid shows a preference for the left plate, and so surface tension forces drive the liquid towards the left, resulting in a decrease in ϕ as the capillary number is increased. However, as the capillary number is increased, the contact line slips less along the surface (see figure 2.4(b), and so the effect of the wettability of either plate becomes less important, as was noted in the previous paragraph. Therefore, at a high enough capillary number, the effect of the contact angle on the interface shape will be small, and the breakup event will be nearly symmetric about the midpoint of the bridge, so we will observe $\phi \approx 0.5$. This result is consistent with experimental observations (Yakhnin and Chadov, 1983), and is observed at $Ca = 1$ in figure 2.5, where ϕ remains close to 0.5 up to a contact angle of 110°.

If both contact lines are allowed to slip, we see qualitatively similar behavior to the results obtained with a single moving contact line. Figure 2.6(a) shows the interface profile at several times as the liquid column is stretched with $\theta_{right} = 60°$ and $\theta_{left} = 80°$. Here, the right plate pulls liquid away from the left plate because it is more wettable. So, despite the left plate being wettable (*i.e.* $\theta_{left} < 90°$), the contact line moves down this surface. In figure 2.6(b) we show an extreme case of this behaviour, where $\theta_{left} = 120°$. In this example the left plate is non-wettable, so the contact line slips down this plate more quickly than the bridge can thin, and all the liquid after breakup rests entirely on the right plate, leading to complete liquid transfer.

Figure 2.7(a) shows ϕ as a function of the difference between θ_{left} and θ_{right}, hereafter referred to as $\Delta\theta$, at different values of θ_{left}. The first point of interest in this figure is that the plate with the largest drop after breakup is always the plate which is most wettable,

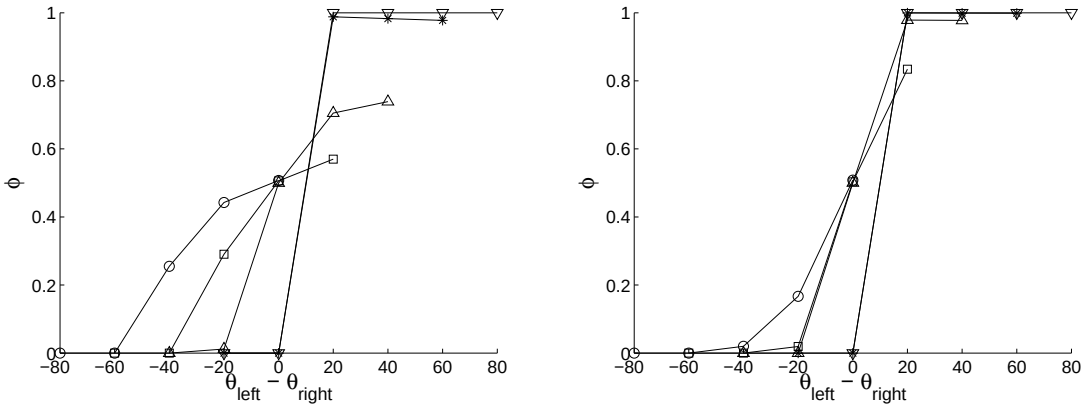

Figure 2.7: Mass fraction transferred to the right plate after breakup, ϕ, vs. the difference in the contact angles of the two plates, $\Delta\theta = \theta_{left} - \theta_{right}$ for (a) $Ca = 0.1$ and (b) $Ca = 0.01$. In both plots the symbols correspond to $\theta_{left} = 40^\circ$ ($\circ$), 60° ($\square$), 80° ($\triangle$), 100° ($*$), 120° ($\triangledown$).

and the difference in the amount of liquid on either plate increases as $\Delta\theta$ rises. Therefore, if the two plates have the same contact angle, breakup will be symmetric about the midpoint of the bridge. This is the reason curves of constant θ_{left} meet at $(\Delta\theta = 0, \phi = 0.5)$, with the exception of the curves for $\theta_{left} = 100^\circ$ and $\theta_{left} = 120^\circ$. In these two cases, because both plates are non-wettable, the contact lines slip down the plates more quickly than the bridge can thin, as shown in figure 2.8(a). This forces the bridge to reach a maximum at the bridge midpoint, instead of a minimum, as was observed for all other computations when $\Delta\theta = 0$.

Because the contact angles on either plate are equal in this situation, the contact lines slip off both plates at the same speed, as shown in figure 2.8(b), where the time evolution of the left and right contact line positions, along with the minimum bridge radius, are indistinguishable. Therefore, the breakup event occurs at both plates simultaneously, instead of in the middle of the bridge, and so no liquid is transferred to the right plate. However, it is important to note that the incorporation of a more realistic contact line model (Blake, 2006) could affect the dynamics of breakup if the two surfaces have different dewetting speeds. This would result in the liquid slipping off of one surface before the other.

The second point to note in figure 2.7(a) is that, as the left plate becomes less wettable, ϕ becomes more sensitive to changes in θ_{right}. This indicates that there is no simple relationship between $\Delta\theta$ and ϕ, but that ϕ must depend on the absolute values of the contact angles at either plate as well. This is because the contact angle can greatly alter the shape of the interface, *i.e.* the interface should assume a different shape if $\theta_{left} = 60^\circ, \theta_{right} = 40^\circ$, vs. when $\theta_{left} = 100^\circ, \theta_{right} = 80^\circ$, even though $\Delta\theta = 20^\circ$ in both cases.

Figure 2.7(b) shows results from a set of computations which are identical to those presented in figure 2.7(a), but at $Ca = 0.01$. Qualitatively, this plot is similar to figure

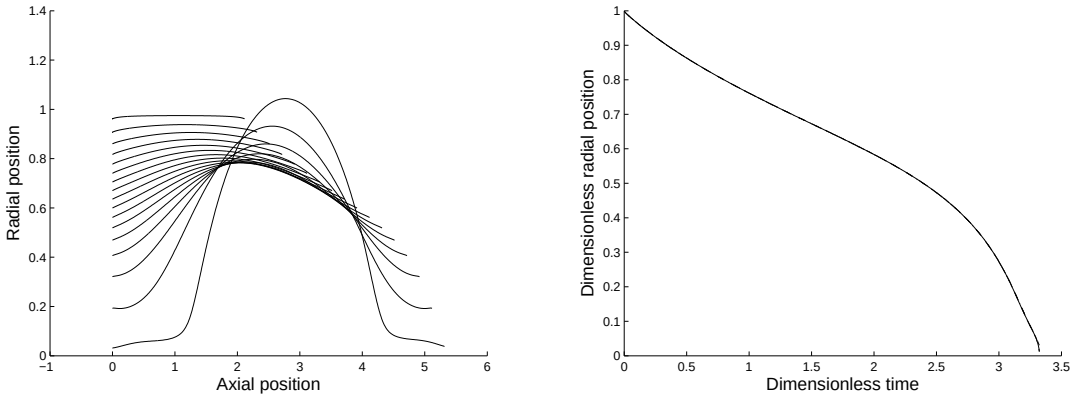

(a) (b)

Figure 2.8: Results from a computation with $Ca = 0.1$ and $\theta_{left} = \theta_{right} = 100^\circ$. Panel (a) shows the interface shape at various times, while panel (b) shows the minimum radius (—), left contact line position (−−), and right contact line position (− · −), all as a function of time. Note that these three curves are indistinguishable.

2.7(a), though the curves of constant θ_{left} change more rapidly around $\Delta\theta = 0$. The reason for this is similar to that discussed when only one contact line was pinned (see figure 2.5), *i.e.* as surface tension forces become stronger, the liquid will move rapidly towards the more wettable surface, and therefore more liquid will be found on that surface after breakup than at a higher capillary number.

It is of interest to compare our computational results to experiments performed by Gupta et al. (2007) on stretching liquid bridges between chemically different surfaces. They observed that the static contact angle, θ_S, could not be used to predict which surface would receive more liquid after breakup. They postulated instead that whichever surface had the smallest difference between θ_S and the receding contact angle, θ_R, would be the surface that experienced the greatest amount of slip. This additional slip would then leave the surface with a smaller drop of liquid on it after breakup than the surface with a larger value of $\theta_S - \theta_R$. While our computations do not account for a difference between static and dynamic contact angles, figure 2.7 agrees with Gupta et al.'s conclusion that the liquid transfer should depend on the dynamic contact angle. It should also be noted that the experiments by Gupta et al. (2007) did not test whether $\theta_S - \theta_R$ or simply θ_R could explain the trends in their data, as the plate with the largest value of $\theta_S - \theta_R$ was also the plate with the lowest θ_R in the experiments discussed. We note that there are also several experimental and theoretical studies examining liquid transfer between flat plates in the quasi-static regime (Chadov and Yakhnin, 1979; Darhuber et al., 2001; Kang et al., 2009), which are not discussed here.

The results from this section illustrate the rich nature of the problem of stretching liquid bridges with dynamic contact lines. Even when ignoring the relationship between contact line velocity and dynamic contact angle (see the review by Blake (2006) for more

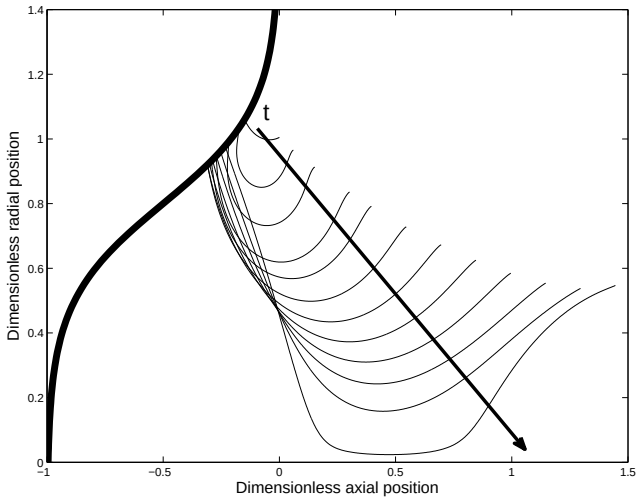

Figure 2.9: Liquid bridge shapes at various times for $Ca = 0.1$, $r_c = 0.8$, $r_s = 0.3$, $Ca = 0.1$ and $\theta_{left} = \theta_{right} = 70°$. The thick black line on the right-hand side of the plot shows the outline of the gravure cavity.

information), we observe a diverse range of breakup behaviors. We have shown that more liquid rests on the plate with the lowest contact angle after breakup, and that the amount of liquid is proportional to the difference in contact angle between the two plates. We also find that this difference becomes more important as the capillary number is decreased, *i.e.* as surface tension becomes more important, the difference in wettability between the two surfaces has a greater effect on liquid transfer. The next step is to address the effect that cavities with corners and slanted walls have on liquid transfer.

2.4 Results: Trapezoidal cavities

If we replace one of the flat plates with a trapezoidal cavity (figure 2.2), we find that the evolution of the free surface, and thus the liquid transfer, is quite different. Figure 2.9 shows the evolution of the interface shape at $Ca = 0.1$, $\theta_{left} = \theta_{right} = 70°$, $r_c = 0.8$, and $r_s = 0.3$. For this computation, the right plate was initially touching the top of the cavity, such that $L(t = 0) = 0$, and the liquid meniscus was placed slightly below the upper cavity corner, similar to the example shown in figure 2.2. The interface was allowed to reach a static equilibrium shape from a cylindrical shape before stretching began, as discussed at the end of section 2.2.3. As the bridge thins, the contact line initially slips down both plates. However, despite having the same contact angle on both plates, the liquid slips down the left plate much more slowly than the right plate. This is shown in figure 2.10(a), which plots the time evolution of the contact line position on both plates, as well as the minimum bridge radius. The relatively slow slippage of the left contact line down the cavity

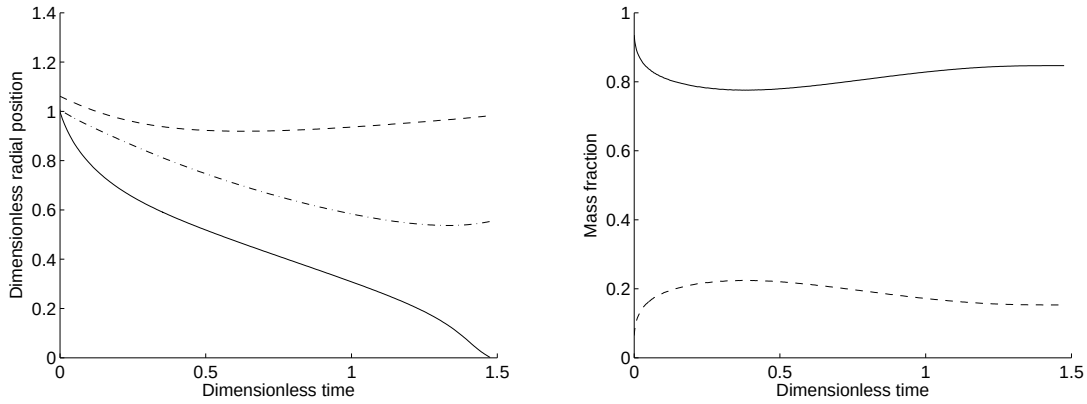

(a) (b)

Figure 2.10: Results from a computation at the same conditions as figure 2.9. Panel (a) shows the time evolution of the minimum bridge radius (—), the left contact line position (−−), and the right contact line position (− · −). Panel (b) shows the fraction of liquid on either the left (—) or the right (−−) of the minimum.

wall creates a large difference in the size of the drop resting on either plate after breakup. Figure 2.10(b), which shows the evolution of the fraction of liquid on either the left or right of the minimum bridge radius, indicates the same trend, with $\phi \approx 0.2$, despite both plates having the same contact angle. This is in contrast to our observations on liquid transfer with flat plates, where we find that when $\Delta\theta = 0$, $\phi = 0.5$.

To explain this difference in slip down flat plates and cavities, it is useful to examine the pressure contours near the contact lines, as is shown in figure 2.11 for the same conditions as the computation presented in figures 2.9 and 2.10. The contour plots were created for results taken at a dimensionless time $t \approx 0.4$, which was just before the left contact line pinned. At the right plate (figure 2.11(b)), the pressure gets very high near the contact line, and decreases gradually as the distance from the contact line is increased. This indicates a strong driving force pumping liquid from the right contact line towards the rest of the bridge, causing the contact line to slip down the plate. The pressure also increases at the left contact line (figure 2.11(a)), but not nearly as much as at the right contact line. The relatively small driving force for flow at the left contact line, compared to the right contact line, creates the effective contact line pinning observed on the cavity wall.

The relatively low pressure gradient at the left plate can be explained by noting that the curvature of the free surface near the cavity wall is nearly constant. Because the plate is angled towards the inside of the bridge, the liquid interface does not need to deform as much as it approaches the cavity wall to maintain a constant contact angle as it does when it approaches the flat plate. Therefore, while a large pressure gradient develops near the right plate due to capillary forces, the gradient near the left plate remains small, producing the contact line pinning observed in figure 2.10.

Figure 2.12 shows how ϕ varies with the cavity aspect ratio at $Ca = 0.1$ for five com-

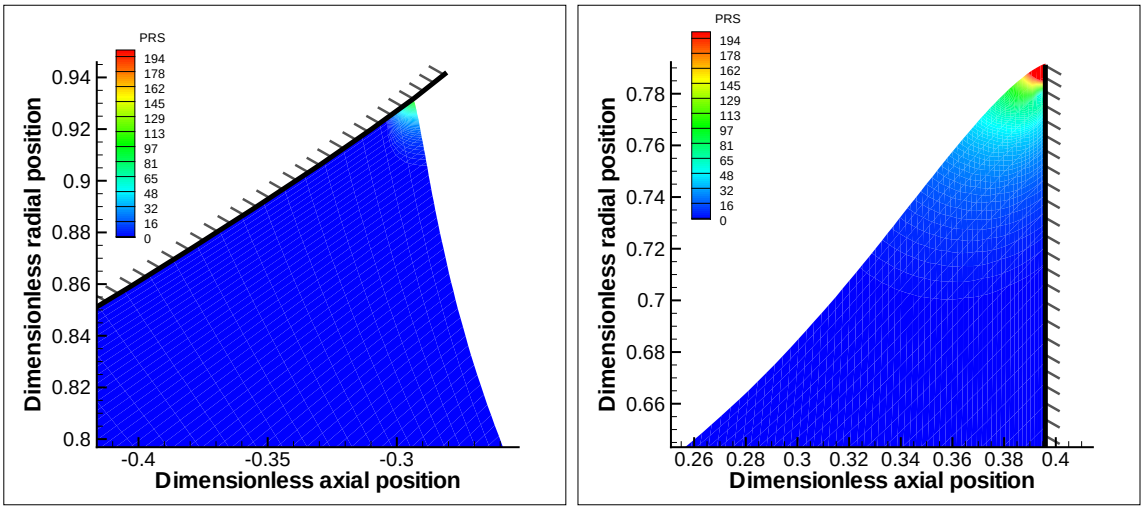

(a) (b)

Figure 2.11: Contours of the dimensionless pressure for a liquid bridge being stretched under the same conditions as in figures 2.9 and 2.10. These plots were produced using results at a dimensionless time of $t \approx 0.4$. Panel (a) shows the liquid region near the contact line on the cavity wall, while panel (b) shows the liquid region near the contact line on the flat plate

binations of contact angles. The initial cylindrical bridge was made to intersect the cavity wall at the same axial position for all runs (see figure 2.13), so that the location of the contact line relative to the cavity corners did not change as the cavity width was increased. The results are shown in dimensionless form, using cavity depth as the characteristic length, which is typically on the order of 50μm for industrial printing processes. As with the results presented in figures 2.9-2.11, the meniscus was initially located just beneath the upper cavity corner, and the right plate was initially touching the top surface of the cavity, so $L(t = 0) = 0$.

As was observed with flat plates, if the cavity geometry and θ_{left} are fixed, ϕ rises as θ_{right} falls, *i.e.* as the right plate is made more wettable it receives more liquid. Also, ϕ rises as θ_{left} rises for constant θ_{right}, *i.e.* as the cavity is made less wettable it receives less liquid. Therefore, for a given cavity shape, the dependence of ϕ on the contact angles can be understood through our results obtained using flat plates. If the cavity is made wider while holding the contact angles fixed, more liquid is transferred to the right plate, indicating that it is easier to empty wide cavities. This is due to the existence of two inherent timescales in the stretching bridge: the time required for breakup of the liquid bridge due to rising capillary pressures in the neck, and the time it takes the contact line to slip off of the cavity wall. With the former, one would expect that this time depends only on the initial thickness of the bridge, and not on external parameters such as the cavity geometry or contact angles, whereas the wall slip time should depend strongly on both the cavity geometry and the contact angle. If a wide cavity is used, the capillary breakup timescale will be larger than for a narrow cavity because the bridge is thicker. However, because the

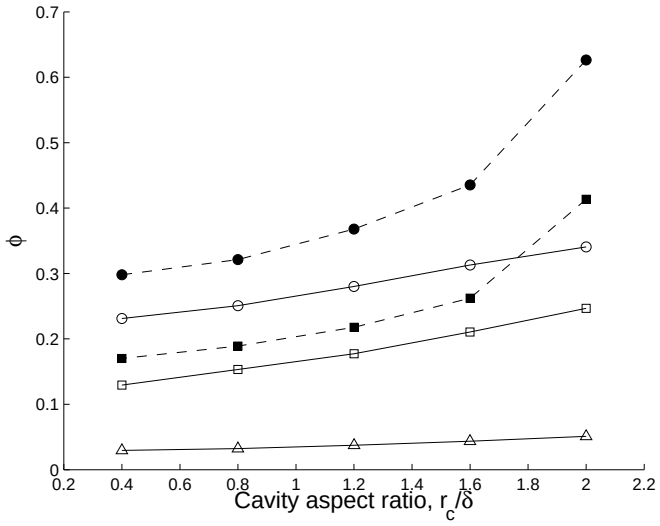

Figure 2.12: Mass fraction transferred to the right plate after breakup, ϕ, vs. cavity width for $\delta = 50\mu m$, $r_s = 15\mu m$ and $Ca = 0.1$. The curves represent $(\theta_{left}/\theta_{right})$: 70/50 (○), 70/70 (□), 70/90 (△), 90/50 (●), 90/70 (■).

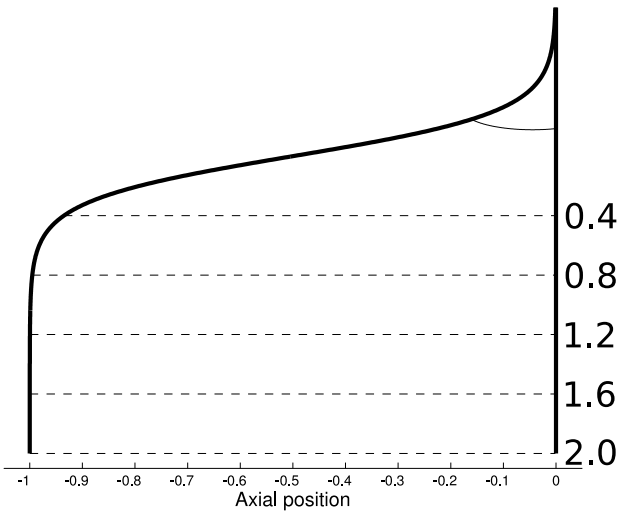

Figure 2.13: Trapezoidal cavity geometries for the runs presented in figures 2.12 and 2.14. The left and right lines represent the cavity and flat plate respectively. The dashed lines show the location of the bridge symmetry axis ($r = 0$) for the aspect ratio listed on the right side of the figure. The initial meniscus (—) for a run with $\theta_{right} = \theta_{left} = 70^\circ$ is also included.

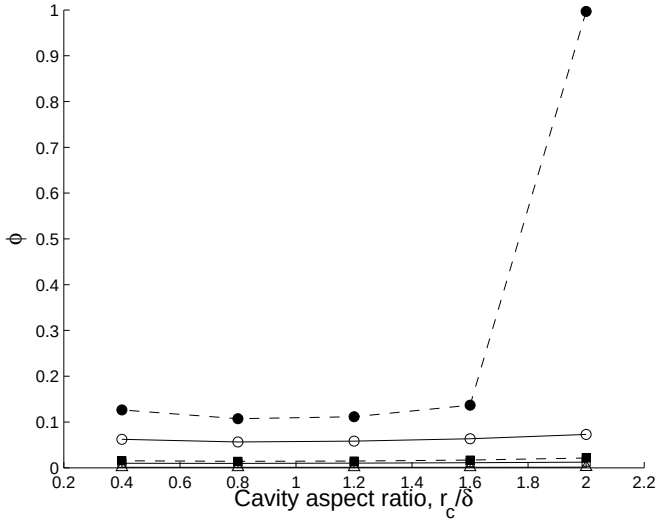

Figure 2.14: As for figure 2.12, but at $Ca = 0.01$

slope of the cavity wall has not changed (figure 2.13), the time it takes the contact line to slip down the wall and onto the cavity bottom will not have changed either. Therefore, the contact line will be able to slip further down the cavity wall for a cavity with a large aspect ratio, which will increase ϕ. In fact, at an aspect ratio of 2 and with $\theta_{left} = 90°$, the contact line has enough time to slip around the bottom corner of the cavity and onto the cavity bottom, producing the sudden increase in ϕ for these widths.

Predictions at a lower capillary number, $Ca = 0.01$, are shown in figure 2.14. For nearly all the contact angle combinations and geometries, ϕ has decreased from the values shown in figure 2.12. While the optimal capillary number for liquid transfer depends on the sign of $\Delta\theta$ when flat plates are used (figure 2.7), figures 2.12 and 2.14 show that ϕ increases with increasing Ca when a cavity is present, except when $r_c/\delta = 2$, $\theta_{right} = 90°$ and $\theta_{left} = 50°$, where ϕ increases as Ca is decreased. This one data point occurs because, for this contact angle/geometry combination, the contact line has enough time before the bridge breaks to slip around the bottom corner and onto the flat base of the cavity. At this point, the system behaves as if it were a bridge between flat plates, and so the large difference in wettability drives liquid towards the right plate, completely emptying the cavity.

This decrease in liquid transfer normally observed is due to contact line pinning, which is found to be stronger as the capillary number is lowered. As was discussed earlier, the right contact line slips quickly down the flat plate due to the high capillary pressure gradient developed there, relative to that seen on the cavity wall (figure 2.11). Therefore, if we increase the effect of surface tension, we will also increase the capillary pressure gradient developed near the right contact line, and so the liquid will slip down the flat plate more quickly at a lower capillary number. However, the relatively constant curvature of the free surface by the cavity wall (figure 2.11(a)) indicates that when surface tension forces are

made stronger the capillary pressure gradient will not increase significantly. In fact, we observed a slight decrease in the capillary pressure gradient because the stronger surface tension forces further smoothed the curvature of the interface. Therefore, as the capillary number is lowered, the contact line on the cavity wall pins more strongly while the contact line on the flat plate slips more quickly, leading to much lower liquid transfers than at a high Ca.

If the capillary number is increased to $Ca = 1$, the effect of plate wettability essentially vanishes, as would be expected from our results with flat plates (see figure 2.5), and the liquid transfer becomes only a weak function of contact angle (results not shown). However, the effect of cavity aspect ratio remains significant, with larger cavities emptying more completely than smaller cavities, for the same reason discussed above for $Ca = 0.1$.

Another parameter to study is the location of the contact line relative to the upper cavity corner. This is an important parameter to understand because of its relevance to the doctoring process in gravure printing, which is used to remove excess liquid from the area between cavities. Doctoring can result in either over- or under-filled cavities, which will affect the amount of liquid transferred onto the substrate. To model this, we no longer have the right plate touching the top surface of the cavity, but instead will allow for a thin film of liquid initially outside the cavity. We assume an initial dimensionless gap of $L(t = 0) = 0.07$ units between the top of the cavity and the flat plate. This distance was chosen to be as small as possible, without producing excessive mesh distortion during the early stages of stretching. For this analysis, we chose $r_s = 0.3$, $r_c = 0.8$, and varied the initial meniscus position from 0.6 to 1.4. This value corresponds to the radius of the initially cylindrical bridge of liquid that is allowed to relax to a steady state configuration, as discussed in the last paragraph of section 2.2.3. Figure 2.15(a) shows some examples of this initial meniscus shape for $\theta_{left} = \theta_{right} = 70°$.

Figure 2.15(b) shows that as the meniscus is moved further up the cavity wall, ϕ increases for all contact angle combinations considered. If the meniscus initially lies far down the cavity wall, the contact line motion will be slow because it will pin in place quickly, as was noted earlier. This results in a large amount of liquid being unavailable for transfer to the right plate. However, as we move the meniscus up the cavity wall, the wall becomes less slanted, eventually resembling a flat plate. This change in the cavity topography allows the contact line to move more freely down the upper portion of the wall, resulting in an increase in the fraction of liquid that can be transferred to the right plate. When the meniscus lies well within the cavity, as shown by the bottom interface profile in figure 2.15(a), the low liquid transfer is likely due to the disparity between the initial radial position of the right and left contact lines, which has produced a very thin initial bridge. However, for all the other initial conditions this effect does not appear to be large.

The results presented in this section highlight the effect that geometrical features, such as corners and slanted walls, have on liquid transfer. We find that the relatively constant

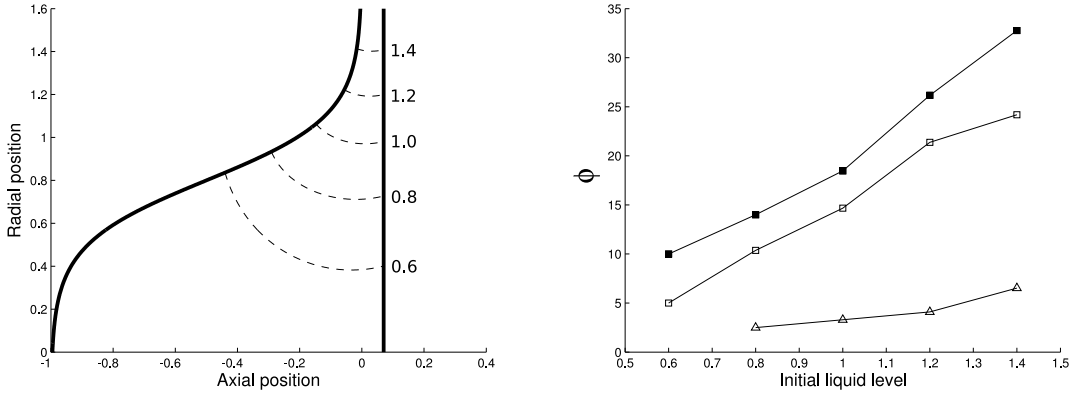

(a) (b)

Figure 2.15: (a) Initial meniscus locations ($- - -$) for computations with $\theta_{left} = \theta_{right} = 70°$. The left and right lines represent the cavity and flat plate respectively, and the liquid lies beneath the dashed line. The numerical value to the right of each meniscus profile corresponds to the initial liquid level used when representing the results. (b) Mass fraction transferred to the right plate after breakup, ϕ, vs. initial meniscus position for $r_s = 0.3$, $r_c = 0.8$, and $Ca = 0.1$. The curves represent ($\theta_{left}/\theta_{right}$): 70/70 (□), 70/90 (△), 90/70 (■).

interfacial curvature near the cavity wall produces a correspondingly small pressure gradient near the contact line, relative to that developed near the flat plate. This allows the contact line to pin in place on the cavity wall, while the contact line on the flat plate is forced to slip down the plate. The pinning event has a significant effect on liquid transfer, decreasing the amount of liquid found on the moving plate after breakup relative to the computations with flat plates. If the cavity is made wider, more liquid is transferred to the flat plate. This is because a wider cavity allows the liquid to slip a greater distance down the cavity wall before breakup. Finally, if the initial position of the contact line is moved up the cavity wall, we find that contact line pinning is delayed, allowing the bridge to stretch further before breakup. This increase in stretching time allows for a greater fraction of liquid to be transferred to the flat plate, indicating that an over-filled cavity will transfer liquid more efficiently.

2.5 Comparison to the Rayleigh-Plateau limit

If surface tension is dominant, a stretching liquid bridge will progress through a series of equilibrium shapes, determined by conservation of mass and the Young-Laplace equation of capillarity. This concept has been applied frequently in the literature to simplify the computation of the interface shape at low capillary numbers (Pepin et al., 2000; Urso et al., 2002; Cai and Bhushan, 2008; De Souza et al., 2008; Vagharchakian et al., 2009). However, it is not clear at which capillary numbers this quasi-static assumption becomes applicable, and when viscosity needs to be incorporated in the model. A comparison of our results on stretching liquid bridges to the static Rayleigh-Plateau limit (RPL), which states that

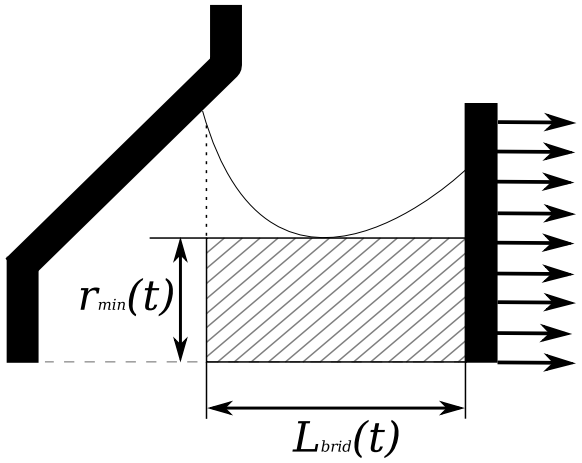

Figure 2.16: Schematic of the system considered for figure 2.17

a cylinder of liquid with a length greater than its circumference is unstable, could provide an upper bound on the capillary number for which a quasi-static assumption can be used, and could also provide insight into the nature of the stabilizing effect of viscosity on the stretching bridge. We note that one could perform a comparison between our results and the stability of a surface of revolution, such as a nodoid, but we choose to compare to the RPL because the comparison is much simpler.

To do this, we have tracked the length of the bridge, L_{brid}, defined as the axial distance between the two contact points, as the bridge thins. If we then consider a static cylinder of length L_{brid} and radius r_{min}, as shown in figure 2.16, we can apply the RPL to determine whether this liquid cylinder is stable. The value of $L_{brid}(t)$ at which the hypothetical cylinder is elongated just enough that it is unstable is referred to as L_{RP}. This length is then compared to the final breakup length, $L_{breakup}$, as seen in figure 2.17, for the data presented in this chapter with two moving contact lines. The solid line in the plots represents the line $L_{RP} = L_{breakup}$. A data point that lies on this line represents a computation where the bridge broke immediately after the hypothetical cylinder reached the RPL. Figure 2.17(a) shows results for a capillary number of 0.1. The data is shifted to the right of the RPL, indicating that the bridge was able to stretch beyond where the hypothetical cylinder becomes unstable. This implies that viscosity acts to stabilize the bridge during stretching, which has already been noted for flat plates (Gaudet et al., 1996). This stabilization occurs because the viscous normal stresses, which become more important as Ca is increased, oppose surface tension driven thinning. It is interesting to observe that, despite covering a wide range of contact angles, initial conditions and cavity geometries, all of the data points for flat plates appear to lie on a single line, while all the results for cavities appear to lie on another line. This indicates that the role viscosity plays in stabilizing the stretching bridge depends only on the inclination of the cavity wall. In fact, the two computations where the liquid was able to slip onto the flat cavity bottom (seen at $L_{breakup} \approx 5$ and 5.5 in figure

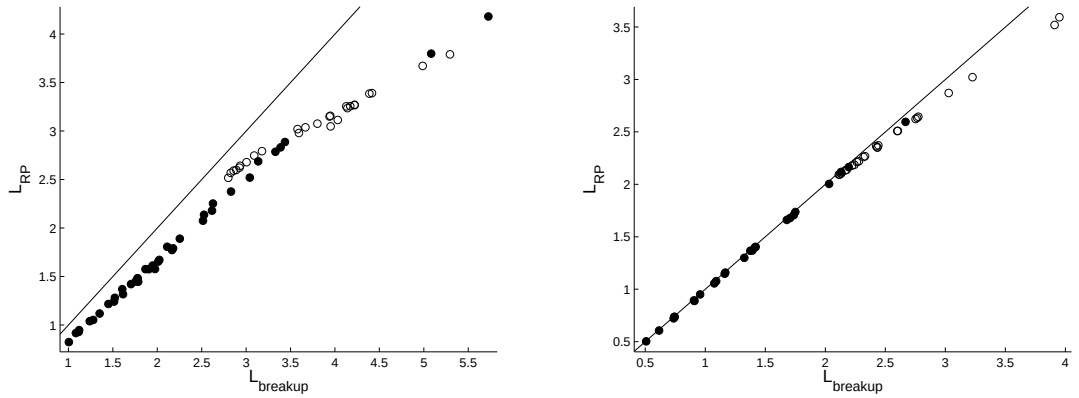

Figure 2.17: A comparison of the length at which a static cylinder with L_{brid} and r_{min} becomes unstable to the final bridge length. The line $L_{RP} = L_{breakup}$ (—) is plotted along with the results presented in this chapter for both flat plates with unpinned contact lines (○) and cavities (●). Panel (a) presents data for $Ca = 0.1$ and Panel (b) for $Ca = 0.01$.

2.17)(a), appear to fall on the trend line for flat plates. This provides further support for our hypothesis that the inclination of the plate is the only factor determining the level of stabilization of the bridge.

At a lower capillary number the bridge breaks shortly after the hypothetical cylinder reaches the RPL, regardless of the contact angle or plate geometry, as shown in figure 2.17(b). While not all of the data lies on the line $L_{RP} = L_{breakup}$, there is very little deviation, and a further decrease in the capillary number is expected to improve the agreement between L_{RP} and $L_{breakup}$. This is a surprising observation because the RPL is valid for static cylinders of liquid, whereas we have modeled highly curved, stretching interfaces with both flat plates and cavities, as is shown in figure 2.16. However, the agreement between our dynamic results and the static RPL indicates that, at a capillary number below $Ca \approx 0.01$, our system can be treated as if it were in a quasi-static state.

The analysis presented in this section has shown that the effect of viscosity on stabilizing a stretching liquid bridge depends only on the inclination of the end plates and not any other geometrical feature, contact angles, or initial condition. Also, we have shown that at a low capillary number, the breakup length of stretching liquid bridges agrees with the Rayleigh-Plateau limit applied to a static cylinder of liquid with radius r_{min} and length L_{brid}. While this analysis does not aid in predicting the breakup length of the bridge before performing a computation, it does provide an upper bound on the capillary number for which a quasi-static analysis (Pepin et al., 2000; Urso et al., 2002; Cai and Bhushan, 2008; De Souza et al., 2008; Vagharchakian et al., 2009) can be trusted. This is an important finding because quasi-static analyses are much less computationally intense than transient, 2D FEM computations.

2.6 Conclusions

We have used a 2D Galerkin FEM to study the stretching of axisymmetric liquid bridges in Stokes flow, while allowing the contact lines to slip along the end plates. If both surfaces are flat and have the same contact angle ($\Delta\theta = 0$), then the size and shape of the droplet resting on either plate after breakup are identical. If there is a difference in wettability between the two surfaces, more liquid is found after breakup on whichever surface has the lower contact angle, or the higher wettability. The relative amount of liquid on either plate is then determined by the capillary number, with a low capillary number producing a much larger drop on the surface with the higher wettability, and a high capillary number producing nearly equal-sized drops on both surfaces. The presence of a cavity on one of the plates was also studied in an attempt to understand how geometric features affect the breakup dynamics. The qualitative conclusions from this work can be applied to any curved surface, though the cavity shape chosen was motivated by gravure printing. We find that the constant interfacial curvature in the vicinity of the contact line on the cavity wall produces a smaller pressure gradient than is observed on the flat plate, which forces the contact line to pin in place on the cavity wall. Because contact line pinning is tied to the curvature of the interface, we find that a lower capillary number produces stronger pinning, and thus smaller drops on the flat plate, unless the cavity is both wide and hydrophobic enough to allow the contact line to slip onto the cavity base. At this point, the large difference in wettability between the two plates drives liquid towards the flat plate, and a higher liquid transfer is observed at a lower capillary number.

While we did not perform any studies to determine the effect of the cavity wall inclination, r_s, we can postulate the effect that varying this parameter would have on contact line slip, and thus liquid transfer. If r_s is increased the inclination of the cavity wall will decrease, producing a flat plate in the limit that $r_s \to \infty$. Because contact line pinning does not occur on flat plates, we therefore expect to observe weaker pinning on the cavity wall as r_s increases, which will lead to higher liquid transfer. Conversely, if we decrease r_s and so increase the inclination of the cavity wall, we would expect to see stronger contact line pinning, and thus a decrease in liquid transfer.

Finally, we performed a simple analysis comparing the breakup length of the stretching bridges to the Rayleigh-Plateau limit by comparing the maximum stable length of a hypothetical cylinder of static liquid with a radius given by the minimum radius of the bridge, to the breakup length of the bridge for the data presented in this chapter with two moving contact lines. At a capillary number of 0.1 we find that the bridges are able to stretch beyond the point where the hypothetical cylinder becomes unstable, and that the additional distance the bridge stretches depends on the inclination of the cavity wall, but not on the cavity width, contact angle combination, or initial meniscus location. This indicates that the stabilizing effect of viscosity is related to how strongly the contact line pins on the cavity wall, which is the manifestation of increasing the inclination of the cavity

wall. At a capillary number of 0.01 the bridge broke at approximately the same length that the hypothetical cylinder became unstable, regardless of the shape of the plates or combination of contact angles. This agreement between the breakup length of our stretching liquid bridges and the static model allows us to set an upper bound on the capillary numbers for which the often used quasi-static approximation (Pepin et al., 2000; Urso et al., 2002; Cai and Bhushan, 2008; De Souza et al., 2008; Vagharchakian et al., 2009) can be applied when modeling stretching liquid bridges.

The present work provides an important extension of previous work on stretching liquid bridges by considering the effect of contact line slip along flat plates and plates with cavities. These results are applicable to any system with chemically different plates and plates with corners or slanted walls, but they are especially relevant to the gravure printing process, because an understanding of the cavity emptying process will aid the gravure practitioner in designing gravure rolls that can print smaller features than is currently possible. While industrial printing inks are rarely Newtonian and the cavities are not normally axisymmetric, the incorporation of moving contact lines and geometrical features with Newtonian liquid bridges provides an important first step in the analysis of industrial printing processes. However, non-Newtonian effects can produce drastically different breakup shapes from stretching Newtonian liquid bridges and jets (Yao and McKinley, 1998; Renardy, 2002; Doshi et al., 2003; Renardy and Renardy, 2004; Yildirim and Basaran, 2001), and therefore it is important to understand their effect on liquid transfer to improve our understanding of industrial printing processes.

Another important effect to study is the interaction of liquid between multiple cavities (Chuang et al., 2008). If a continuous pattern is to be printed, it is generally done by transferring liquid from multiple cavities spaced closely together, so that the printed droplets can combine to create a continuous feature. This interaction is especially important when printing electronic circuits, because if two drops do not connect the circuit will not function properly. To model these systems, however, requires a 3D FEM model, developed in chapter 4. Such a model would also allow us to describe non-axisymmetric bridge shapes and stretching velocities, such as combinations of shear and extensional motion, which has already been shown to improve liquid transfer in 2D planar systems (Hoda and Kumar, 2008).

CHAPTER 3

Stretching liquid bridges with inertia

Liquid bridges with moving contact lines are found in a variety of settings, such as capillary feeders and high-speed printing. Although it is often assumed that the length scale for these flows is small enough that inertial effects can be neglected, this is not the case in certain applications. To address this issue, we solve the Navier-Stokes equations with the finite element method for the stretching of a liquid drop between two surfaces for non-zero Reynolds numbers. We consider an axisymmetric liquid bridge between a moving flat plate and either a stationary flat plate or a cavity. The contact lines are allowed to slip, and we evaluate the effect of the Reynolds number and contact angles on the transfer of liquid to the moving plate. In the case of two flat plates, we find that inertia forces the interface to map onto a similarity solution in a manner that shifts the breakup point toward the more wettable surface. Inertia and wettability are thus competing effects, with inertia driving fluid toward the surface with the higher contact angle, and wettability driving fluid toward the surface with the lower contact angle. When a cavity is present, contact line pinning on the cavity wall biases breakup toward the cavity as the Reynolds number is increased, leading to improved cavity emptying. As the flat plate is made more wettable, a second pinch-off point can form near that plate, leading to a satellite drop and a reduction in liquid transfer to the plate. Therefore, higher liquid transfer is not always obtained with a more wettable substrate when inertia is present, in contrast to Stokes flow. We also compare our results to those obtained using a model based on the long-wave approximation and find good qualitative agreement, with the long-wave model overpredicting the amount of liquid transferred after breakup.[1]

[1]This chapter is reproduced with minor modifications from S. Dodds, M. S. Carvalho, and S. Kumar. "Stretching Liquid Bridges with Moving Contact Lines: The Role of Inertia", *accepted for publication in Physics of Fluids*

3.1 Introduction

Liquid columns are relevant to a variety of industrial (Gaudet et al., 1996; Yao and McKinley, 1998; Meseguer and Sanz, 1985; Powell et al., 2002; Cai and Bhushan, 2008; Vogel and Steen, 2010) and natural (Vogel and Steen, 2010; Prakash et al., 2008; Reis et al., 2010) systems, and as such, they have been the subject of research for nearly 150 years (Plateau, 1863; Eggers, 1997; Eggers and Villermaux, 2008). A convenient platform often used to study liquid columns is the liquid bridge, which consists of a drop of liquid connecting two solid surfaces that can be stretched apart. To simplify both computational and experimental analyses of liquid bridges, the three-phase contact line at the intersection of the solid, liquid, and gas phases is often pinned in place. While this is a reasonable approximation in some applications, such as extensional rheometry (Yao and McKinley, 1998) and float-zone crystallization (Meseguer and Sanz, 1985), it is not true for all systems. In fact, the motion of the contact line often plays a key role in the bridge dynamics, and thus it is vital to understand this effect for many applications (Powell et al., 2002; Cai and Bhushan, 2008; Vogel and Steen, 2010; Prakash et al., 2008). This is especially true for industrial printing processes, where it is *desirable* for the contact lines to slip along the surfaces, so that the amount of liquid transferred from one surface to another can be maximized. Despite their importance, the effects of contact line motion and surface wettability on liquid bridge dynamics have received very little attention until recently (Powell et al., 2002; Cai and Bhushan, 2008; De Souza et al., 2008; Vagharchakian et al., 2009; Balu et al., 2009; Dodds et al., 2009; Villaneuva et al., 2007; Gupta et al., 2007; Qian et al., 2009; Qian and Breuer, 2011).

A common motivation for the study of liquid bridges is the printing and patterning of small-scale features, which includes various techniques such as contact drop dispensing (Qian and Breuer, 2011) and gravure printing (Dodds et al., 2009). In these processes, current interest is often in producing small features, typically 10 μm or less. These small length scales, combined with stretching speeds on the order of cm/s or lower, allow the inertial terms in the Navier-Stokes equations to be ignored, greatly simplifying theoretical analysis of the stretching and breakup process. However, not all printed patterns are this small, and gravure in particular is often used to produce features on the order of hundreds of microns. In particular, the solution processing of electronic devices often requires features on this length scale (Mäkelä et al., 2005; Pudas et al., 2005). At these scales inertial forces can become significant, resulting in nonlinear effects that produce substantial departures from the bridge behavior observed in Stokes flow, such as the formation of secondary drops during breakup.

Gravure is a common printing and coating technique that is currently used in the production of a variety of consumer products, such as magazines, stamps, and packaging (Kasunich, 1998; Kipphan, 2001). In gravure, a network of micron-sized cavities is engraved into the surface of a cylindrical roll. The cavities are filled with liquid and then pressed

against a substrate, transferring liquid wherever there is a cavity. To date, most of the work on gravure has focused on coating (Patel and Benkreira, 1991; Benkreira and Patel, 1993; Schwartz et al., 1998; Kapur et al., 2001; Schwartz, 2002; Kapur, 2003; Hewson et al., 2010), where the goal is to produce a continuous film, as opposed to printing, where a discrete pattern is desired. This seemingly subtle difference between the two techniques leads to fundamental differences in the fluid mechanics. In coating, for example, the cavities are organized in a way that promotes hydrodynamic interaction between each cavity, so that the features merge properly and a uniform film is produced over the entire substrate. In printing, however, this merging would ruin any discrete patterns, and so proper spacing between each feature must be included. This results in completely different flow profiles for coating and printing, and thus separate studies are required to understand and optimize the dynamics of each process.

There has been a recent burst of activity on gravure printing (Chuang et al., 2008; Hoda and Kumar, 2008; Huang et al., 2008; Kang et al., 2009) due to its ability to produce small features at high speeds, making gravure a promising technique for the large-scale production of electronic devices (Pudas et al., 2005; Krebs, 2009; Noh et al., 2010) and solar cells (Santa-Nokki et al., 2006; Ding et al., 2009; Kopola et al., 2010). A key step in the printing process is the transfer of liquid between two surfaces, which is difficult to visualize directly due to the high speeds and small length scales involved in gravure. Therefore, theoretical analysis provides the best opportunity to understand the dynamics of cavity emptying. In chapter 2, we used a two-dimensional (2D) axisymmetric Stokes flow model to study the emptying of a single cavity. They found that while the wettability of the two surfaces is a key factor in controlling liquid transfer when both of the surfaces are flat, the presence of a cavity on one of the surfaces alters the dynamics significantly. In this case, the contact line effectively pins along the cavity wall, causing the liquid transfer to the flat surface to decrease. This pinning can be overcome by making the surface of the cavity non-wetting, which increases the dewetting speed, or by increasing the cavity width, which gives the contact line more time to slip off the cavity wall before breakup.

While there have been several other studies on the fluid mechanics of gravure printing (Lee and Na, 2010; Kim and Na, 2010; Lee et al., 2010; Ahmed et al., 2011; Ghadiri et al., 2011), the role of inertia on the dynamics of breakup and liquid transfer has not yet been studied systematically. The nonlinear nature of the Navier-Stokes equations makes it difficult to infer how inertia will modify results obtained in Stokes flow. In particular, the way in which inertia interacts with wettability and/or cavity geometry to produce changes in the amount of liquid transferred represents a fundamentally important relationship that to date has not been examined in the literature. The primary goal of this chapter is to better understand this interaction.

The role of inertia on the asymptotics of breakup of liquid columns is well understood, with several studies describing the self-similarity of breakup when inertia is present (Papa-

georgiou, 1995; Eggers, 1993; Chen and Steen, 1997; Chen et al., 2002). It has been shown that while the interface shape and velocity are symmetric about the breakup point in Stokes flow (Papageorgiou, 1995), this symmetry is broken when inertial effects are considered (Eggers, 1993). As we will show, this has significant implications for the shape of liquid bridges at breakup, including the production or suppression of satellite drops, which are secondary drops that form between the two primary ones. Satellite drops are generally considered to be undesirable because if a satellite does not merge with one of the two primary drops, it could land elsewhere on the printed image and decrease the fidelity of the final pattern. Additionally, if the drop is entrained as a mist this can waste potentially valuable compounds, and pose a health hazard if the liquid is toxic. The asymptotic analyses performed in the above references cannot say anything about the behavior of the bridge far away from breakup, and the effect of variables such as surface geometry and wettability remains unknown. Therefore, an improved understanding of the conditions under which satellite drops are formed is an important practical matter, as well as a topic of fundamental scientific interest.

In this chapter we solve the Navier-Stokes equations with the appropriate boundary conditions using the finite element method (FEM), to study the transfer of liquid from a stationary to a moving plate during stretching of an axisymmetric liquid bridge. To account for variations in the wettability of the two surfaces, we allow the contact lines to slip along the solid plates using a Navier slip law, while holding the contact angle constant. Our goal is to understand how wettability and inertial effects interact to produce changes in breakup shape and liquid transfer. We first use a 2D axisymmetric model (section 3.2) to study the effect of the Reynolds number and contact angle on the breakup of liquid bridges stretched between two flat plates (section 3.3 and figure 3.1(a)). We then compare the results from our 2D model to those from a simpler one-dimensional (1D) long-wave model (section 3.4), which has been used extensively in the study of liquid bridges and jets (Eggers, 1993; Papageorgiou, 1995; Zhang et al., 1996; Doshi et al., 2003; Yildirim and Basaran, 2001; Ambravaneswaran and Basaran, 1999; Liao et al., 2006; Qian and Breuer, 2011; Panditaratne, 2003; Bhat et al., 2010). Finally, we use our 2D model to study the stretching of a liquid bridge between a trapezoidal cavity and a flat plate (section 3.5 and figure 3.1(b)) to understand how changes in wettability and surface geometry alter liquid bridge dynamics.

3.2 Problem formulation

3.2.1 2D axisymmetric model

Our system consists of an axisymmetric liquid bridge with a constant volume V, viscosity μ, surface tension σ, and density ρ. We scale length with the initial liquid bridge radius R, velocity with the constant extensional velocity U, time with R/U, and pressure with $\mu U/R$.

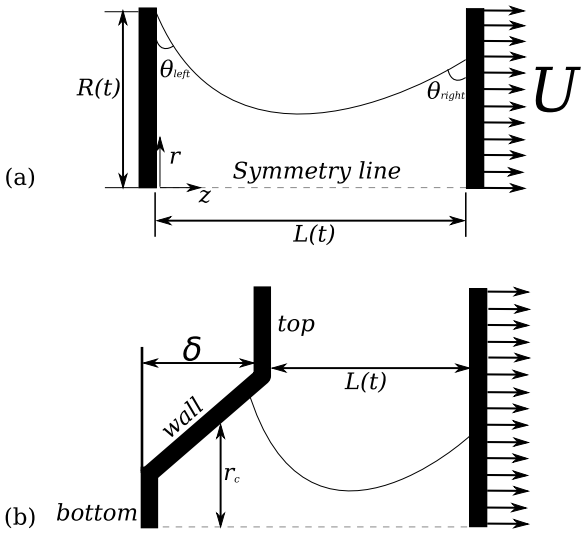

Figure 3.1: Schematics of the geometries considered in this work. (a) A liquid bridge between two flat plates, and (b) a liquid bridge between a cavity and a flat plate.

We can define a Reynolds number $Re = \rho UR/\mu$, which represents a ratio of inertial to viscous forces, such that the Navier-Stokes equations can be written in dimensionless form:

$$Re\frac{D\mathbf{v}}{Dt} = -\nabla P + \nabla^2\mathbf{v}, \tag{3.1}$$

$$\nabla \cdot \mathbf{v} = 0, \tag{3.2}$$

where $\mathbf{v}$ is the velocity and P is the pressure. We assume that the outer phase is a low viscosity gas, and thus ignore its effect on the dynamics of the liquid bridge.

At the gas-liquid interface, we must conserve mass and momentum, leading to the kinematic and interfacial stress boundary conditions:

$$\mathbf{n} \cdot \mathbf{v} = 0, \tag{3.3}$$

$$\mathbf{n} \cdot \mathbf{T} = -\frac{\kappa}{Ca}\mathbf{n}, \tag{3.4}$$

where $\mathbf{n}$ is the outward pointing normal at the interface, $\mathbf{T}$ is the total stress tensor, $Ca = \mu U/\sigma$ is the capillary number, which is a ratio of viscous to surface tension forces, and κ is the curvature of the interface. We take the pressure of the ambient gas surrounding the liquid bridge to be zero when writing equation (3.4) without loss of generality, as this simply sets the pressure datum for the system.

The liquid is thus parametrized by two dimensionless variables, Re and Ca. It should be noted that one could instead scale length with R and time with the capillary breakup time, $t_c \sim \sqrt{\rho R^3/\sigma}$, leading to a velocity scale of R/t_c. In this case the problem is characterised by an Ohnesorge number, $Oh = \mu/\sqrt{\rho R\sigma}$, which is a capillary number with a velocity of

R/t_c, and a Weber number, $We = \rho R U^2/\sigma$, which is a ratio of inertial to surface tension forces. We choose Re and Ca for this work because this allows us to easily isolate the role of inertia on the dynamics of the bridge, though understanding the role of viscosity and stretching speed becomes more difficult as these parameters appear in both Ca and Re.

To finish specifying the boundary conditions in our system, we apply no-slip and no-penetration conditions at the two solid surfaces (figure 3.1):

$$\mathbf{t} \cdot \mathbf{v} = 0, \text{at } z = 0, L(t), \tag{3.5}$$

$$\mathbf{n} \cdot \mathbf{v} = \begin{cases} 0 & \text{for } z = 0, \\ 1 & \text{for } z = L(t), \end{cases} \tag{3.6}$$

and because we are studying axisymmetric cylindrical liquid bridges, we impose symmetry boundary conditions along the bridge axis:

$$\mathbf{t} \cdot (\mathbf{n} \cdot \mathbf{T}) = 0, \tag{3.7}$$

$$\mathbf{n} \cdot \mathbf{v} = 0, \tag{3.8}$$

where $\mathbf{t}$ and $\mathbf{n}$ are the tangent and normal vectors to the solid surfaces or the symmetry line.

We allow the contact lines to slip along the solid surfaces by replacing (3.5) at the contact line with the Navier slip boundary condition, while fixing the contact angle θ instead of the contact line position:

$$\mathbf{t}_{wall} \cdot (\mathbf{n}_{wall} \cdot \mathbf{T}) = \frac{1}{\beta} \mathbf{t}_{wall} \cdot \mathbf{v}, \tag{3.9}$$

$$\mathbf{n}_{wall} \cdot \mathbf{n} = cos\left(\theta\right), \tag{3.10}$$

where $\mathbf{t}_{wall}$ and $\mathbf{n}_{wall}$ are the tangent and normal vectors at the solid surface, $\mathbf{n}$ is the outward pointing normal at the liquid-gas interface, and β is the slip coefficient. We set β to 10^{10} for all computations, producing a shear-free contact line. While our treatment of the contact line neglects the dependence of the contact angle on the slip velocity (Blake, 2006), one would expect the results predicted from this approach to be qualitatively similar to those obtained with a more realistic model. Therefore, as in our previous work in the Stokes-flow regime (chapter 2), we assume that despite utilizing such a simplistic slip model we are able to capture the essential features of stretching liquid bridges with moving contact lines.

Finally, as in chapter 2, we consider two different geometries for the stationary left surface. We first consider a flat plate, defined simply by the plane $z = 0$ (figure 3.1(a)). In

the second case, we use a hyperbolic tangent function to define a cavity wall (figure 3.1(b)):

$$z = \frac{1}{2}\delta\left(1 - \tanh\left(\frac{r - r_c}{r_s}\right)\right), \tag{3.11}$$

where r and z are the radial and axial positions along the wall, δ is the depth of the cavity, r_c corresponds to the distance from the axis of symmetry to the center of the wall, and r_s is related to the curvature of the corners and to the steepness of the cavity wall. Sharp corners and steep walls are obtained by using small values of r_s.

To solve equations (3.1)-(3.10) we use the finite element method along with elliptic mesh generation to track the interface, and a second-order trapezoid rule scheme to perform the time integration. The details of the methods used are described in chapter 2 in detail, and so are not repeated here.

3.2.2 1D long-wave model

A common approach used when studying liquid jets and bridges is to assume that variations in the interface shape are small when compared to the length of the jet/bridge. This leads to a set of greatly simplified lubrication (or long-wave) equations governing the axial velocity and the interface shape. This approximation has been widely used because it provides a simple enough description of the liquid to allow analytical (Eggers, 1993) and efficient numerical solutions (Zhang et al., 1996), while maintaining good agreement with experiments (Zhang et al., 1996; van Hoeve et al., 2010) and with 2D axisymmetric computations (Yildirim and Basaran, 2001; Eggers and Dupont, 1994). However, the long-wave model has been used to describe systems with moving contact lines in only one study to date (Qian and Breuer, 2011), and it has not been systematically validated against a full solution of the Navier-Stokes equations to determine its ability to capture the dynamics of moving contact lines.

If we define ϵ as the ratio of the length scale of variations in the interface position to the length of the bridge, we can perform an asymptotic expansion in the axial velocity v and pressure p:

$$\begin{aligned} v(r,z) =& v_o(z) + \epsilon v_1(z) + \epsilon^2 v_2(z) + \cdots \\ p(r,z) =& p_o(z) + \epsilon p_1(z) + \epsilon^2 p_2(z) + \cdots \end{aligned} \tag{3.12}$$

Because the radial dependence in this expansion appears in the small parameter ϵ, this indicates that to leading order the variables are constant along a radial slice of fluid. This has important implications when modeling moving contact lines, as will be discussed later. We can now substitute equation (3.12) into equations (3.1)-(3.4) to obtain the following set of evolution equations at leading order (Eggers and Dupont, 1994), while dropping the 'o'

subscripts for clarity:

$$\begin{aligned} Re\,(v_t + vv_z) &= -\frac{1}{Ca}\kappa_z + \frac{3}{h^2}\left(h^2 v_z\right)_z, \\ h_t + vh_z + \frac{1}{2}hv_z &= 0, \end{aligned} \tag{3.13}$$

where h is the interface position, κ is the curvature:

$$\kappa = \frac{1}{h\left(1+h_z^2\right)^{1/2}} - \frac{h_{zz}}{\left(1+h_z^2\right)^{3/2}}, \tag{3.14}$$

and all other variables have the same definition as in the previous section. As in Eggers and Dupont (1994), we keep the full curvature term to allow for a more accurate description of the interface.

To solve these equations, we use the finite element method as described in Zhang et al. (1996). This requires the introduction of a new variable, Ω, which augments equations (3.13):

$$\Omega - \frac{\partial h}{\partial z} = 0. \tag{3.15}$$

We take this approach to decrease the order of equations (3.13) from third-order in height to second-order, allowing the use of lower-order basis functions in our FEM analysis.

The boundary conditions that we apply on the velocity are no-penetration at either plate:

$$v(z=0;t) = 0, v(z=L;t) = 1. \tag{3.16}$$

For h, we set either the position of the contact line or the contact angle. In the first case, the height at both plates is fixed, and no boundary conditions are applied on Ω:

$$h(z=0,L;t) = 1. \tag{3.17}$$

If we instead wish to fix the contact angle we can use a simple geometric relation between Ω and θ, since:

$$\Omega = \frac{\partial h}{\partial z} = \cot(\theta). \tag{3.18}$$

In this case, we apply the contact angle as a Dirichlet condition on Ω, and we apply no boundary conditions on h.

Because the radial velocity is ignored in this framework, we cannot impose a slip law. If we substitute the expansion (3.12) into the Navier slip law (3.9), we find that the slip law does not appear at leading order. Therefore, neglecting Navier slip is consistent with the 1D model. The contact line is thus able to move freely over the solid, which allows for a fair comparison with our 2D model, where the slip parameter was chosen to be large enough so that the contact line is shear-stress free.

Finally, we do not compare the 1D and 2D models when a cavity is present. Because

the 1D model only contains information about the interface, it is unable to capture the dynamics of the liquid deep within the cavity, where there is no interface.

3.2.3 Selection of parameters for study

The liquid bridge systems in this study provide a rich parameter space characterized by Re, Ca, the left (θ_{left}) and right (θ_{right}) contact angles, the cavity dimensions (δ, r_c, and r_s), the liquid volume, and the initial interface shape and liquid velocity profile. In this work, we restrict our study to understanding how inertia, wettability, and surface geometry interact to modify the stretching dynamics of the liquid bridges.

For most printing processes, length scales vary from roughly 1-500 μm, the liquid viscosity can be anywhere from 1 to 100 cp, and stretching speeds range from 0.01-1 m/s. If we take the liquid density to be similar to that of water, and the surface tension to be between 20-70 mN/m, we get $Re \approx 10^{-4}$ - 10^{2} and $Ca \approx 10^{-4}$ - 1. Based on the results in chapter 2, we fix the capillary number at $Ca = 0.1$, vary the contact angles between 50° and 90°, and have chosen to use one wide ($r_c = 0.90$, $r_s = 0.14$, $\delta = 0.45$) and one narrow ($r_c = 0.8$, $r_s = 0.3$, $\delta = 1.0$) cavity. To evaluate the effect of inertia, we vary the Reynolds number from $Re = 0$ to 100, choosing specifically $Re = 0$, 0.1, 1, 10, and 100 for all runs.

The initial bridge shape and velocity for the liquid present us with additional variables which can be adjusted. In the case of flat plates, we begin with a cylinder of liquid that has a length equal to its radius. We then solve either our 1D or 2D model equations holding both plates still until a steady-state is achieved, which provides the initial interface shape. For the velocity, we note that because the system is Galilean invariant (Papageorgiou, 1995), pulling only one plate at a velocity of U gives the same result as pulling both plates apart at a velocity of $\pm U/2$, so long as the bridge initially has a linear velocity profile that matches with these boundary conditions. Otherwise, there would be an initial acceleration during the first time step as the top plate goes from static to moving, which would violate the assumption that our system is in an inertial reference frame, as discussed in Ambravaneswaran and Basaran (1999). To achieve this linear velocity profile in a manner that is consistent with our equilibrium bridge shape, we use the Stokes-flow solution from the first time step after stretching from equilibrium (at $t = 10^{-6}$) as our initial condition for computations where $Re \neq 0$.

When the left plate has a trapezoidal cavity, the procedure for developing the initial condition is similar to that for flat plates. The right plate is initially in contact with the top of the cavity so that $L(t = 0) = 0$, and the liquid meniscus is placed slightly below the upper cavity corner (see figure 2.13, where the cavity shapes studied in this work are for aspect ratios of 0.8 and 2.0). As when only flat plates are present, we allow the interface to achieve an equilibrium shape, and then use the Stokes-flow solution from the first time step during stretching as our initial condition when $Re \neq 0$.

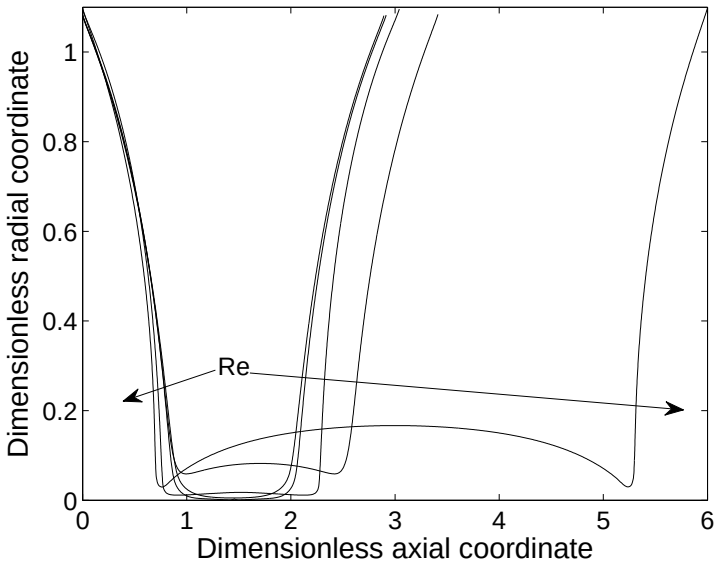

Figure 3.2: Interface shapes near breakup for $Re = 0$, 0.1, 1, 10, and 100, for a liquid bridge with $\theta_{left} = \theta_{right} = 50^{\circ}$ and $Ca = 0.1$.

3.3 Results: Flat plates

We first consider a case where the two plates have the same contact angle, $\theta_{left} = \theta_{right} = 50^{\circ}$. Figure 3.2 shows the interface as the bridge approaches breakup for $Re = 0$, 0.1, 1, 10, and 100. As the bridge is stretched it thins in its middle to conserve mass, resulting in two large drops resting on either plate that are connected by a thin fluid thread. This leads to an increased capillary pressure in the thread due to the increased azimuthal curvature, which pumps fluid out of the neck and accelerates breakup. As the Reynolds number increases, the relative strength of inertia to viscosity also increases. This slows the diffusion of momentum and thus the fluid in the neck becomes more difficult to accelerate, resulting in a bridge that is able to stretch further as Re is increased (see figure 3.2). A consequence of the increased stretching length is the production of satellite drops, which have been observed previously with pinned contact lines (Zhang et al., 1996). As the neck thins it can become extremely elongated, leading to two pinch-off events and the formation of a satellite drop, which is observed in figure 3.2 at $Re = 1$, 10, and 100. However, the breakup remains symmetric about the bridge mid-point despite the satellite drops, because the contact angles on both plates are the same.

If the contact angles are no longer the same on both plates, we expect the symmetry of breakup to be broken. This is observed in figure 3.3(a), which shows the interface as the bridge approaches breakup for $\theta_{left} = 70^{\circ}$ and $\theta_{right} = 90^{\circ}$. The difference in wettability between the two plates produces distinctly different breakup shapes from those seen in figure 3.2. Here we observe only one breakup event, which shifts toward the left plate as Re

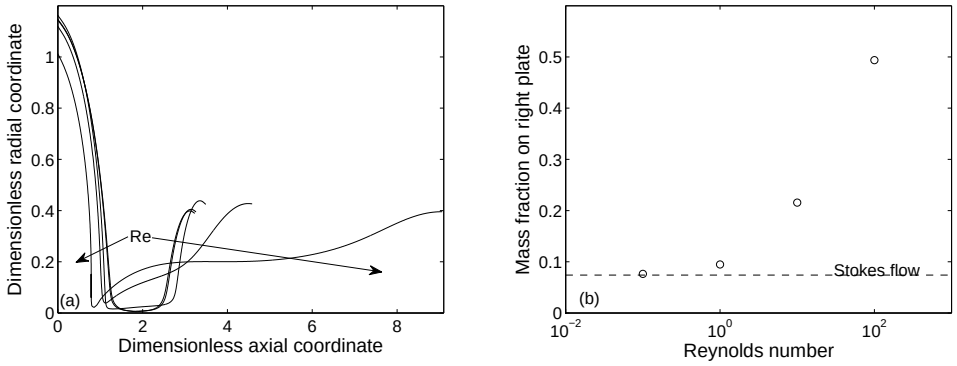

Figure 3.3: (a) Interface shape $Re = 0$, 0.1, 1, 10, and 100, and (b) mass fraction transferred to the right plate after breakup for a liquid with $\theta_{left} = 70^\circ$ and $\theta_{right} = 90^\circ$, and $Ca = 0.1$.

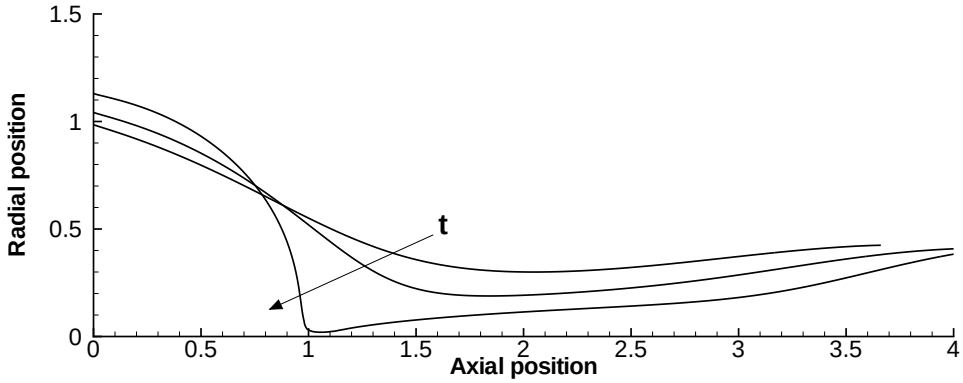

Figure 3.4: Interface profiles at three times during stretching for $\theta_{left} = 70^\circ$, $\theta_{right} = 90^\circ$, $Ca = 0.1$, and $Re = 10$.

is increased. This change in the breakup behavior can be understood by noting that, in the region near the breakup point, the interface must map onto a similarity solution as time progresses. As discussed by Eggers (1995), when surface tension, viscosity and inertia are all present the similarity solution is asymmetric, with the interface approaching the pinch-off location at a much greater slope on one side than the other. This higher slope occurs in our system near the more wettable plate because the liquid will have a larger contact radius on this plate, providing a natural orientation for the similarity solution. We observe this in figure 3.4, where we plot the interface profile at three times near breakup. At the earliest time shown the bridge is far from breakup, but already the interface is asymmetric about the minimum. As breakup is approached, the region near pinch-off takes on a shape similar to that predicted by Eggers (1993), and the pinch-off location is convected to the left due to the high capillary pressure developed on the right of the pinch-off, resulting in a single breakup point near the left plate.

The shift in the breakup location observed in figures 3.3(a) and 3.4 comes along with

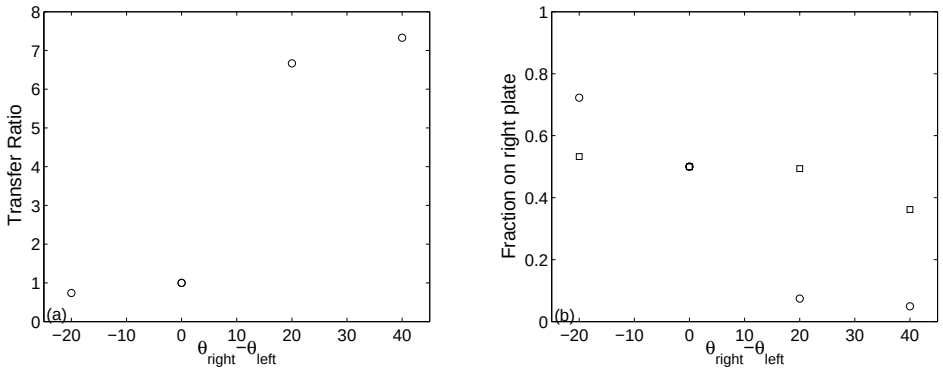

Figure 3.5: (a) Transfer ratio, which is the ratio of liquid transfer at $Re = 100$ to that at $Re = 0$, versus the difference in contact angles between the right and left plates at $Ca = 0.1$. (b) Liquid transfer to right plate versus difference in contact angle for $Re = 0$ ($\circ$) and $Re = 100$ ($\square$).

an increase in the liquid transfer to the right plate, seen in figure 3.3(b). We hypothesize that this is related to the curvature of the interface near the contact line. As the breakup point shifts to the left, the interface must curve more sharply in the vicinity of the left contact line to satisfy the contact angle condition, eq. (3.10), while still mapping onto the similarity solution at the breakup location. This produces a large gradient in curvature near the contact line, which in turn produces a large gradient in pressure. This gradient in pressure will then drive fluid away from the contact line, resulting in a smaller contact radius on the left plate near breakup as Re is increased. This is observed in figure 3.3(a), where the contact line position on the left plate is seen to decrease significantly as Re is increased.

In the previous two paragraphs we have shown that when the left plate is more wettable than the right, the breakup point shifts toward the left, causing an increase in the liquid transfer to the right plate. One would then expect that if the right plate were more wettable these trends would reverse. This is seen in figure 3.5(a), which plots the transfer ratio, defined here as the ratio of the liquid transfer to the right plate at $Re = 100$ to that at $Re = 0$, versus the difference in wettability between the two plates. If the left plate is more wettable than the right, *i.e.*, $\theta_{right} - \theta_{left} > 0$, the transfer ratio is greater than one, indicating that inertia is improving the liquid transfer. However, when $\theta_{right} - \theta_{left}$ is negative the transfer ratio is less than one, indicating that liquid transfer to the right plate is hindered by inertia. It should be noted that because the breakup is symmetric when the two contact angles are equal, the liquid transfer at $Re = 100$ has been set to 0.5 in these cases, even though the presence of a large satellite drop will alter the actual liquid transfer after breakup.

Finally, we note that the transfer ratio does not indicate anything about the actual liquid transfer to the right plate, which is shown in figure 3.5(b). In Stokes flow, we observe that as the right plate becomes less wettable relative to the left the liquid transfer decreases, as

was noted in chapter 2. However, at $Re = 100$, the liquid transfer is nearly independent of the contact angles, even though the interface shape at breakup varies significantly between each of these cases.

The results from this section illustrate how inertial effects modify the breakup behavior of stretching liquid bridges with moving contact lines. We have shown that inertia and wettability are competing effects, with the amount of liquid transferred to the more wettable plate decreasing with an increase in Re. The origin of this competition lies in the interaction between surface wettability, which characterizes the global behavior of the system, and the similarity solution near breakup, which characterizes the local behavior of the system. This is an unexpected result that has important practical implications, since operating in a high-Re regime can help to overcome the poor liquid transfer observed when the right plate is less wettable than the left. We have also shown that the formation of satellite drops depends not only on the liquid parameters Re and Ca, as it does when the contact lines are pinned, but also on surface wettability. This has practical implications as the wettability can be used to suppress the formation of satellite drops, which are generally seen as being detrimental. We now compare some of the results from this section to those obtained using a one-dimensional model.

3.4 Comparison of 1D and 2D models

The use of 1D long-wave equations has led to a great deal of advancement in our understanding of the breakup dynamics of liquid columns. The simplicity of these 1D equations often allows for the derivation of analytical descriptions of breakup (Eggers, 1993), while the use of only one dimension allows complex phenomena to be included (*e.g.*, surfactant dynamics) without the computational expense of solving the full two-dimensional problem. While 1D long-wave equations have been used to study a number of different systems, to the authors knowledge only one paper has taken this approach in studying moving contact lines. In their work, Qian and Breuer (2011) used a long-wave model to study the breakup of a liquid column with one moving contact line at low Ca and Re, and compared the model predictions to their experiments. They found that while they did not observe good agreement between theory and experiment when the contact angle was fixed, there was very good agreement when using a Tanner's law relation for the contact angle with two fitting parameters.

We begin by validating our implementation of the long wave equations using our 2D code with pinned contact lines (figure 3.6). We see good agreement between the two models at all three Re shown, as is expected given previous comparisons Yildirim and Basaran (2001). When we compare the two models with moving contact lines (figure 3.7), we observe that while there is reasonable qualitative agreement, there are significant quantitative differences. In particular, the 1D model predicts a much greater extent of contact line motion than the

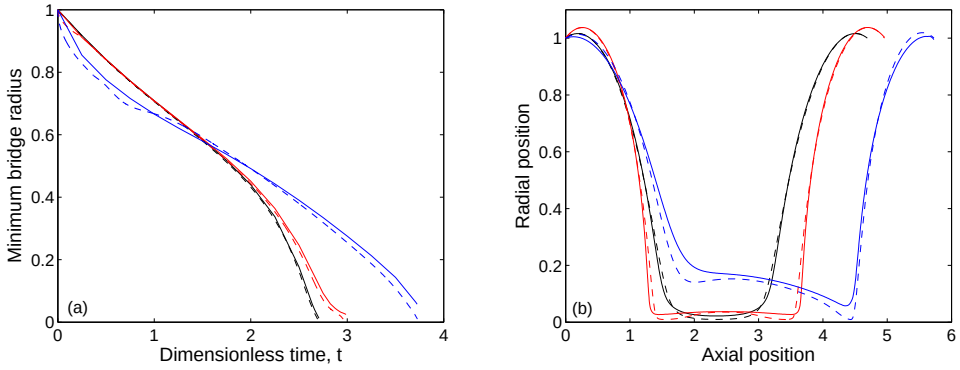

Figure 3.6: Comparison of 1D (−−) and 2D (—) models for $Re = 0.1$ (black), $Re = 1$ (red), and $Re = 10$ (blue). Both contact lines are pinned in place during stretching, and Ca =0.1. Panel (a) compares the variation of the minimum bridge radius with time during stretching, and panel (b) compares the shape of the interface just before breakup.

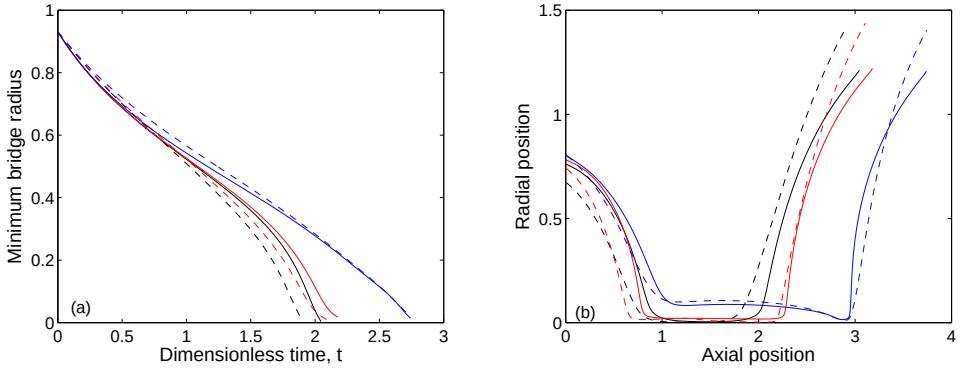

Figure 3.7: Same as in figure 3.6 but with moving contact lines. For these computations, $\theta_{left} = 70°$ and $\theta_{right} = 50°$.

2D model. This results in a significant overestimate of liquid transfer to the moving plate with the 1D model at low Reynolds numbers (see table 3.1). As Re is increased and the strength of inertia relative to surface tension goes up, the 1D model better predicts the liquid transfer for the conditions considered here. This is most likely due to the decreasing importance of the contact lines, as surface tension effects become less pronounced. However, the 1D model continues to do a poor job of capturing the shape of the free surface, and in particular cannot predict the overturning of the interface that is observed near pinch-off at higher Re.

A key assumption in the development of the long-wave model is that there are no radial variations in the system variables, and thus the pressure within the liquid is determined solely by the normal stress boundary condition at the interface. While this assumption is valid when the contact lines are pinned, the stress singularity that arises when the contact lines are allowed to move leads to an exponentially increasing pressure as the contact lines are approached (Huh and Scriven, 1971). Therefore, in the vicinity of the contact lines the

Table 3.1: Comparison of the liquid transfer to the right plate after breakup for the 1D and 2D models, with $\theta_{left} = 70°$, $\theta_{right} = 50°$, and $Ca = 0.1$. Liquid transfers are given as fractions, and the percent difference is calculated relative to the liquid transfer from the 2D model.

	$Re = 0$	$Re = 1$	$Re = 10$	$Re = 100$
1D model	0.845	0.820	0.704	52.6
2D model	0.723	0.711	0.652	53.3
Difference	16.9%	15.3%	8.0%	1.3%

pressure is no longer constant along a radial slice and the assumptions for the 1D model break down. However, as the Reynolds number is increased and the effect of surface tension decreases relative to inertia, the contact line motion becomes less important and the model becomes more accurate, as seen in table 3.1.

It is important to note that, because the error in the 1D model is due to the singularity that develops near the contact lines, one cannot expect the long-wave equations to be quantitatively accurate unless the contact line model eliminates this singularity (*e.g.* the model presented in Shikhmurzaev, 1993). Therefore, while Qian and Breuer (2011) obtain good agreement between their model and experiments, this might be due to the two fitting parameters that were used in the Tanner's law expression, and not to any fundamental ability of the 1D model to properly capture the dynamics of moving contact lines.

We have shown that while the long-wave model can greatly improve computational efficiency, it is unable to capture the complex dynamics which arise due to the motion of the contact line. However, the model is able to predict the qualitative behavior of the bridge, and thus is still a valuable tool for understanding the dynamics of liquid bridges with moving contact lines. Our next step in this work is to return to our 2D-axisymmetric model to study how the presence of topographical features, such as cavities, affects breakup and liquid transfer for non-zero Re.

3.5 Results: Trapezoidal cavities

We now consider how breakup is altered by the presence of a trapezoidal cavity on the stationary plate, shown schematically in figure 3.1(b). Figure 3.8(a) shows the interface shape near breakup for various Reynolds numbers with a wide cavity and $\theta_{left} = \theta_{right} = 70°$. Qualitatively, the results are similar to those observed in figure 3.3, *i.e.*, the breakup point shifts toward the left as the Reynolds number is increased, leading to an increase in liquid transfer (figure 3.8(b)). However, in figure 3.8 the contact angles are symmetric, and thus the asymmetric breakup could not have been caused by a difference in wettability between the two plates (as was the case in figure 3.3), but must instead have been caused by the presence of the cavity. As discussed in chapter 2, the inclination of the cavity wall allows the interface to approach the wall without a large curvature gradient. This results in a lower pressure near the contact line at the cavity than at the flat plate, and thus

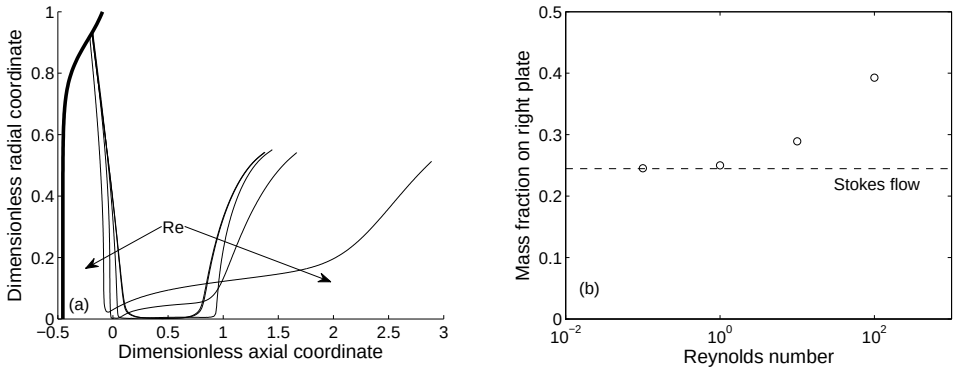

Figure 3.8: (a) Interface shape at $Ca = 0.1$ and $Re = 0$, 0.1, 1, 10, and 100, and (b) mass fraction transferred to right plate after breakup for the wide cavity ($r_c = 0.90$, $r_s = 0.14$, and $\delta = 0.45$) and a liquid with 70° contact angles at both plates. The thick black line on the left side of panel (a) is the cavity outline.

the contact line at the cavity effectively pins in place. Because this pinning prevents the contact line from continuing to slip down the cavity wall, the contact radius in the cavity will generally be much larger than on the flat plate. In Stokes flow, this reduces the liquid transfer to the right plate compared to the case where the cavity is absent. In flows with finite Re, the sharp interface deformation near the cavity forces the interface to map onto a similarity solution in a manner that shifts the breakup closer to the cavity, similar to what was discussed in section 3.3 for flat plates. The simple presence of a cavity is thus able to force asymmetric breakup at high Re, even in the absence of a wettability difference.

In figure 3.8 the problem parameters were such that only a single breakup point was observed. However, if the right plate is made more wettable, this can produce a second breakup point on the other side of the bridge. This is observed in figure 3.9, which was obtained for the same parameters as figure 3.8, but with $\theta_{right} = 50°$ instead of 70°. Here we see that while the cavity drives pinch-off on the left, the lower contact angle drives pinch-off on the right as well. We see the clear formation of two breakup points, resulting in the eventual formation of a satellite drop. It is important to note that it becomes difficult to quantify liquid transfer when a satellite drop is present because there is no way to know where the satellite will end up after breakup. It is possible that the satellite merges with either primary drop, or is simply entrained as a mist and removed from the system. For the purposes of this work, the liquid transferred to the right plate is computed by calculating the volume of liquid to the right of the *first* breakup point. In figure 3.9, for example, the liquid contained within the satellite will be included as part of the liquid transferred to the right plate.

To further examine the formation of satellite drops, we tabulate the liquid transfer at $Re = 0$ and $Re = 100$, and the transfer ratio for a number of cases listed in table 3.2. Here we vary both contact angles as well as cavity geometry, using the wide and narrow cavities defined in section 3.2.3, and we group the results based on whether or not a satellite drop is

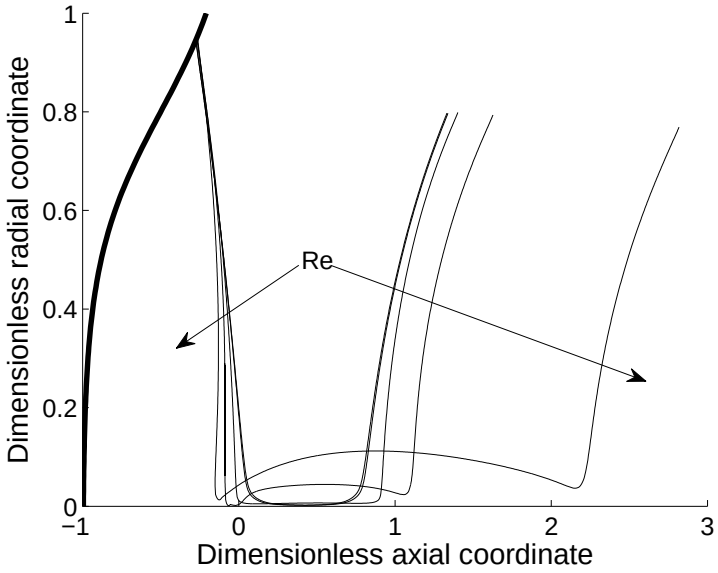

Figure 3.9: The same as figure 3.8(a), but with $\theta_{right} = 50^\circ$ instead of $\theta_{right} = 70^\circ$.

formed. We consider only $\theta_{right} = 50^\circ$ and 70° because significant error is introduced into the solution for small angles ($\sim 30^\circ$ or lower for quadrilateral elements), while for angles higher than $\theta_{right} = 70^\circ$, no liquid was found on the flat plate after breakup in the cases we studied. We observe that for $\theta_{right} = 50^\circ$ satellite drops are observed in all but one case, whereas for $\theta_{right} = 70^\circ$ satellites are observed in only one case. This suggests that by properly balancing the tendency of the cavity to force pinch-off on the left, and the wettability of the flat plate to force pinch-off on the right, one can promote (or suppress) the formation of satellite drops. It should be noted that we found no correlation between the formation of satellite drops and the cavity contact angle or cavity shape when a cavity is present. This is because the effect of contact line pinning becomes the predominant factor controlling the interface shape at the cavity, as we noted in chapter 2.

While the production of satellite drops can be predicted by considering only the wettability of the flat plate, the transfer ratio depends more clearly on the difference in contact angles, shown in figure 3.10. Here we note that as the wettability of the cavity is increased, *i.e.*, as $\theta_{left} - \theta_{right}$ becomes smaller, the transfer ratio increases, indicating that the effect of inertia on liquid transfer becomes stronger. We also see an increase in the transfer ratio when the cavity is narrow, for a fixed wettability difference. In both cases, this is due to the resistance that the contact line experiences when trying to slip down the cavity wall, which is made stronger by a more wettable cavity or by a more narrow cavity. This increased resistance creates a larger contact radius for the drop resting in the cavity, which drives breakup further into the cavity, as discussed earlier. Therefore, the effect of inertia on liquid transfer relative to the Stokes-flow case will be more pronounced for a narrower or more wettable cavity.

Table 3.2: Comparison of results obtained with a trapezoidal cavity at $Ca = 0.1$. Definitions for wide and narrow cavities are in section 3.2.3, and the transfer ratio is defined in figure 3.5.

θ_{left}	θ_{right}	cavity shape	Liquid transfer at $Re = 0$	Liquid transfer at $Re = 100$	Transfer ratio
No satellite drop observed					
110°	70°	narrow	0.273	0.367	1.34
90°	70°	narrow	0.186	0.319	1.72
70°	70°	narrow	0.150	0.280	1.87
110°	70°	wide	1.000	1.000	1.00
70°	70°	wide	0.245	0.393	1.60
90°	50°	wide	0.673	0.409	1.72
Satellite drop observed					
90°	50°	narrow	0.321	0.295	0.92
70°	50°	narrow	0.251	0.296	1.18
50°	50°	narrow	0.208	0.279	1.34
90°	70°	wide	0.416	0.360	0.87
70°	50°	wide	0.347	0.358	1.03
50°	50°	wide	0.288	0.377	1.31

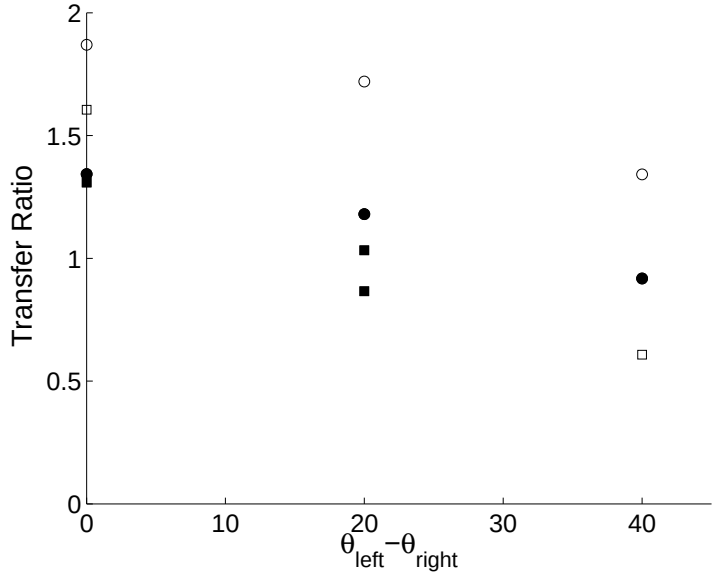

Figure 3.10: Transfer ratio, as defined in figure 3.5, vs. $\theta_{left} - \theta_{right}$ for both wide (□) and narrow (○) cavities, at $Ca = 0.1$. Filled data points represent computations where satellite drops are predicted.

In this section we have shown that the presence of a cavity on one of the plates can have a significant effect on the breakup dynamics. The cavity causes the contact line to pin along its wall, which shifts the breakup point closer to the cavity and improves liquid transfer. This indicates that inertia can help to overcome the decrease in liquid transfer observed when a cavity is present in Stokes flow. This effect is balanced by the wettability on the flat plate, which can produce an additional pinch-off point and a satellite drop. This leads to the surprising conclusion that, when inertial effects are present, the best operating condition is not always to use the most wettable substrate possible. A more wettable substrate promotes the formation of satellite drops which not only present a potential health hazard, but can actually lead to a *decrease* in the amount of liquid transferred if the satellite does not end up on the right plate.

3.6 Conclusions

We have shown that the presence of inertia can greatly affect the breakup dynamics of stretching liquid bridges, sometimes in surprising ways. This can lead to potentially drastic changes in the amount of liquid transferred to one surface after breakup, as well as the possible formation of satellite drops. When the bridge is stretched between two flat plates with the same contact angles, a satellite drop is formed, though the breakup remains symmetric about the bridge mid-point. If there is a difference in wettability, the breakup point shifts closer to the more wettable surface as the Reynolds number is increased. This can lead to large increases in the amount of liquid transferred to the less wettable surface, including the six-fold improvement observed in figure 3.3(b). In addition, we compare our 2D Navier-Stokes results to those obtained using a 1D long-wave approximation. There are significant quantitative differences between the two models because the long-wave model is unable to capture the pressure singularity at the contact lines, which creates a radially varying pressure profile in the bridge. However, the qualitative agreement between the two models is still quite good, making the long-wave model a useful tool for understanding the dynamics of liquid bridges with moving contact lines.

When a cavity is present on the stationary plate, the contact line pins on the cavity wall. This produces a high interfacial curvature, which pushes the breakup location toward the cavity and increases the liquid transfer to the moving plate. As the wettability of the moving plate is increased a second breakup point is produced near this plate, resulting in the formation of a satellite drop. This may result in a decrease in liquid transfer, though this depends on whether the satellite merges with the primary drop on the substrate or the one in the cavity after breakup.

The role of inertia is notable because it demonstrates that inferences built on Stokes-flow behavior of liquid bridges is not always accurate. At a first glance, it seems reasonable to assume that higher liquid transfer will always be obtained by making the right plate

more wettable, improving the tendency of the liquid to exit the cavity and spread onto the moving surface. We have shown that in the presence of inertia, a more wettable right plate does not necessarily improve liquid transfer, and that it can also lead to the formation of satellite drops. Therefore, for practical applications, one needs to carefully consider the regime in which stretching will occur before making a final decision on material properties.

The work presented here is an important extension of existing work on liquid bridges, which had not previously addressed the interplay between inertia, wetting, and surface geometry. These results are especially relevant to industrial printing processes, such as gravure, where $O(1)$ or higher Reynolds numbers are often achieved. However, the printing inks used in industry are rarely Newtonian, and the cavities are generally not axisymmetric. Three-dimensional effects in particular can significantly modify the breakup behavior (Lockwood et al., 2011), and effects such as a combined shearing and extensional plate motion have been shown to improve liquid transfer from cavities in 2D-planar geometries (Hoda and Kumar, 2008) (though it remains to be seen how including the azimuthal curvature of the bridge will alter this conclusion). Due to the computational difficulties associated with solving 3D free-surface problems with moving contact lines, these effects are still poorly understood but promise to be a rich area for further investigation (see chapter 4).

CHAPTER 4

Stretching liquid bridges in three dimensions

Liquid bridges with moving contact lines are relevant in a variety of natural and industrial settings, ranging from printing processes to the feeding of birds. While it is often assumed that the liquid bridge is two-dimensional in nature, there are many applications where either the stretching motion or the presence of a feature on a bounding surface lead to three-dimensional effects. To investigate this we solve Stokes equations using the finite element method for the stretching of a three-dimensional liquid bridge between two flat surfaces, one stationary and one moving. We first consider an initially cylindrical liquid bridge that is stretched using either a combination of extension and shear or extension and rotation, while keeping the contact lines pinned in place. We find that whereas a shearing motion does not alter the distribution of liquid between the two plates, rotation leads to an increase in the amount of liquid resting on the stationary plate as breakup is approached. The mechanism can be understood by considering a rotation-induced fictitious force that pumps liquid toward the stationary surface. This suggests that a relative rotation of one surface can be used to improve liquid transfer to the other surface. We then consider the extension of non-cylindrical bridges with moving contact lines near non-cylindrical features. We find that dynamic wetting, characterized through a contact line friction parameter, plays a key role in allowing the bridge to maintain its original shape after breakup. By adjusting the friction on both plates it is possible to drastically improve the amount of liquid transferred to one surface while maintaining the fidelity of the initial bridge shape.[1]

[1]This chapter is currently in preparation for publication.

4.1 Introduction

Free-surface flows represent one of the most important realms of fluid mechanics. In addition to their natural elegance (Py et al., 2007; Jung et al., 2009), free-surface flows are found in an incredibly diverse array of settings, from coating (Kistler and Scriven, 1984) and printing (Dodds et al., 2009) flows, oil recovery (Gaudet et al., 1996), and rheological measurements (Yao and McKinley, 1998), to natural defense systems (Vogel and Steen, 2010), the feeding of birds (Prakash et al., 2008), and the lapping of cats (Reis et al., 2010). The importance of this field can be measured in part by the large number of review articles on the subject (see, for example, Stone, 2010; Oron et al., 1997; Craster and Matar, 2009; Eggers, 1997; Eggers and Villermaux, 2008; Weinstein and Ruschak, 2004; Blake, 2006; Bonn et al., 2009). From an analytical perspective, free-surface flows present a formidable challenge because the location of the interface is not known *a priori*, but must be included as part of the solution for the flow field. This has led to a great deal of work involving the development of numerical techniques to solve the Navier-Stokes equations with a moving boundary, including the volume-of-fluid (VOF, see Scardovelli and Zaleski, 1999), level set (Sethian and Smereka, 2003), and arbitrary Lagrangian-Eulerian (ALE, see Christodoulou et al., 1997) methods. While computations of free-surface flows are becoming increasingly routine in two dimensions, only recently has there been progress in solving for the dynamics of three-dimensional systems (Cairncross et al., 2000; Dimitrakopoulos and Higdon, 2003; Walkley et al., 2005b; Xie et al., 2007; Zhou et al., 2010).

A common example of a free-surface flow is a stretching liquid bridge, which is a mass of liquid connecting two solid surfaces that are pulled apart. Stretching liquid bridges are found in a variety of settings, ranging from printing processes (Dodds et al., 2009) to capillary feeders (Prakash et al., 2008), and so have been extensively studied (see Eggers, 1997; Eggers and Villermaux, 2008, and the references within). It is often assumed that the three-phase contact lines connecting the bridge to the solid remain pinned during stretching, which significantly simplifies both experimental and computational analyses. While this may be a reasonable approximation in some applications, such as extensional rheometry (Yao and McKinley, 1998), it is certainly not the case in others. In printing processes in particular, it is *desirable* for the contact lines to move so that the amount of liquid transferred from one surface to the other can be maximized. Despite this importance, liquid bridges with moving contact lines have only recently received much attention in the open literature (Powell et al., 2002; Gupta et al., 2007; Villaneuva et al., 2007; Prakash et al., 2008; Balu et al., 2009; Qian et al., 2009; Qian and Breuer, 2011; Dodds et al., 2009, 2011a,b).

In addition to the assumption that the contact lines remain pinned, many prior studies on stretching liquid bridges assume an axisymmetric geometry (Gaudet et al., 1996; Zhang et al., 1996; Ambravaneswaran and Basaran, 1999; Yildirim and Basaran, 2001; Kang et al., 2009; Dodds et al., 2009, 2011b). This is a reasonable assumption as surface tension will drive the bridge toward axisymmetry in an attempt to minimize the interfacial

area. However, there are many relevant applications where three-dimensional effects become important. Lockwood et al. (2011) showed that for liquid bridges on the nanometer scale, the roughness of the surface can significantly alter breakup and produce asymmetric bridge shapes due to the topography of the substrate. Darhuber et al. (2001) studied the stretching of non-axisymmetric liquid bridges that were confined by a rectangular chemical pattern, finding that higher capillary numbers are required to ensure that the bridge maintained the pattern shape after breakup. Hoda and Kumar (2008) studied the emptying of liquid from 2D planar cavities as a model system for gravure printing, and found that optimal emptying is obtained when the stretching motion combines both shear and extensional components. Shear is generally avoided during printing in an attempt to minimize pattern distortion, and so this work suggests that one may need to balance emptying with pattern fidelity. However, by using a 2D planar model Hoda and Kumar neglect the azimuthal curvature of the bridge, which can significantly alter its breakup behavior (Huang et al., 2008). To include a combination of shear and extensional motion along with the azimuthal curvature requires a three-dimensional model. An improved understanding of the manner in which three-dimensional effects alter the dynamics of the bridge is therefore of interest in a variety of applications.

Gravure offset printing, shown schematically in figure 4.1, is a typical roll-to-roll printing technique that has shown promise in the solution processing of electronic devices (Hagberg et al., 2001; Pudas et al., 2004, 2005). In this process a pattern is produced by engraving a series of small cavities into the surface of a cylindrical roll, creating an image of the pattern. The cavities are filled with ink and the ink is transferred first onto a rubber backing roll and then onto a moving substrate, after which the ink is dried so that the pattern is fixed in place. This second transfer stage can be idealized as the stretching of a liquid bridge between two flat, rigid surfaces, significantly simplifying analysis. One can then examine the effect of system parameters such as wettability and capillarity on the transfer of liquid to the substrate, which has been done for both 2D-planar and axisymmetric systems (Gupta et al., 2007; Huang et al., 2008; Kang et al., 2009; Dodds et al., 2009, 2011a,b; Ahmed et al., 2011; Ghadiri et al., 2011). However, these studies neglect the three-dimensional nature of the printing process, which arises through several mechanisms. First, the cavities engraved on the roll appear in a network, and the interaction between the cavities can have a significant effect on the emptying process (Schwartz et al., 1998; Schwartz, 2002). Second, the transfer of liquid between rotating, cylindrical rolls implies that the idealization of stretching as a purely extensional motion may not be accurate, as shear and/or rotation can become important during printing. Third, the printed features may have an asymmetric cross-section, as would be the case when printing a letter or a line for a conductive circuit. In this case it is important to understand how the feature shape can be maintained after printing, as surface tension will drive the bridge toward a cylindrical geometry. These issues are difficult to address because printing systems generally incorporate high speeds, small

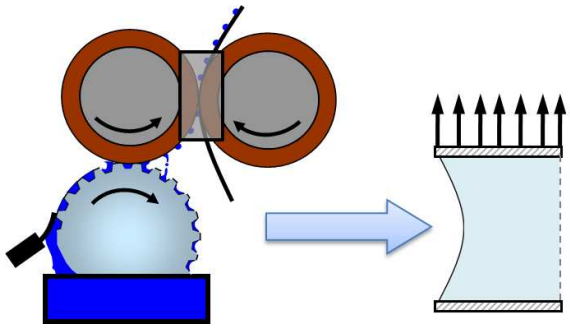

Figure 4.1: Schematic of the gravure offset printing process, and the analogous liquid bridge system.

length scales, and opaque surfaces that make direct visualization difficult, while numerical studies require an algorithm that can solve the Navier-Stokes equations in three dimensions with a free surface and moving contact lines. Such algorithms have only recently been developed (Baer et al., 2000; Dimitrakopoulos and Higdon, 2003; Walkley et al., 2005a; Saha and Mitra, 2009; Zhou et al., 2010).

The goal of this chapter is to evaluate the role of three-dimensional effects on the dynamics of liquid bridges, focusing in particular on the role of either asymmetric stretching or asymmetric initial bridge shapes. To achieve this, we solve the Navier-Stokes equations using the finite element method (FEM) along with the elliptic mesh generation technique discussed by Christodoulou et al. (1997), which has not previously been extended to three dimensions (section 4.2). We then consider how asymmetric stretching alters breakup and liquid transfer while the contact lines remain pinned (section 4.3). Specifically, we examine the effect of either combined extension and shear or extension and rotation, and evaluate how the stretching rates alter the breakup length and the amount of liquid transferred to the moving surface. Finally, we consider how wettability and capillarity affect the stretching of asymmetric bridge shapes, similar to those studied by Darhuber et al. (2001). To do this, we allow the contact lines to slip along the solid surfaces using a Navier slip law and the linearized molecular-kinetic model, which relates the contact angle to the slip velocity (Blake, 2006).

4.2 Problem formulation

4.2.1 Navier-Stokes equations and boundary conditions

We begin by considering a three-dimensional liquid bridge with a constant volume V, viscosity μ, surface tension σ, and density ρ. If we take the bridge radius R to be a typical length scale and the stretching speed U to be a typical velocity scale, we can define a time scale R/U and a pressure scale $\mu U/R$. This allows us to write the Navier-Stokes equations in dimensionless form:

$$Re\frac{D\mathbf{v}}{Dt} = -\nabla P + \nabla^2\mathbf{v} + St\hat{\mathbf{g}}, \tag{4.1}$$

$$\nabla \cdot \mathbf{v} = 0, \tag{4.2}$$

where $\mathbf{v}$ is the velocity, P is the pressure, $\hat{\mathbf{g}}$ is a unit vector in the direction of the gravitational field, $Re = \rho U R/\mu$ is a Reynolds number, and $St = \rho g R^2/\mu U$ is a Stokes number. We assume that the outer phase is a low viscosity gas, and thus ignore its effect on the dynamics of the liquid bridge.

Solving equations (4.1) and (4.2) requires initial and boundary conditions for the velocity, as well as a pressure datum. We impose conservation of mass and momentum at the gas-liquid interface, leading to the kinematic and interfacial stress boundary conditions:

$$\mathbf{n} \cdot (\mathbf{v} - \dot{\mathbf{x}}_{int}) = 0, \tag{4.3}$$

$$\mathbf{n} \cdot \mathbf{T} = -\frac{\kappa}{Ca}\mathbf{n}, \tag{4.4}$$

where $\mathbf{n}$ is the outward pointing normal at the interface, $\mathbf{T}$ is the total stress tensor, $Ca = \mu U/\sigma$ is a capillary number, κ is the curvature of the interface, and $\dot{\mathbf{x}}_{int}$ is the velocity of the mesh at the interface. When writing equation (4.4) we have without loss of generality assumed that the pressure of the ambient gas surrounding the liquid bridge is zero, which sets our pressure datum. Along solid surfaces that do not have a moving contact line we apply no-slip and no-penetration conditions by equating the liquid velocity and the velocity of the surface, $\mathbf{v}_{surf}$:

$$\mathbf{v} - \mathbf{v}_{surf} = \mathbf{0}. \tag{4.5}$$

The system is therefore parametrized by three dimensionless numbers: Re, Ca, and St. In typical printing systems the feature sizes are often on the order of 10 μm, which leads to extensional velocities on the order of 1-10 cm/s. As in previous chapters, we assume that the liquid density is 1 g/L, that its viscosity is between 1-100 cp, and that its surface tension is between 20-70 mN/m. This leads to estimates of Re = 0.001-1, $Ca = 10^{-4}$ - 1, and $St = 10^{-5}$ - 1. It was shown in chapter 3 that for $Re \leq 1$ the bridge dynamics are not significantly affected by inertia and we therefore set $Re = 0$ for all computations, though we note that for larger feature sizes inertial effects can become important. We also set $Ca = 0.1$ and $St = 0$ based on our prior work in this thesis.

We take advantage of problem symmetry and include either one or two symmetry planes depending on the bridge geometry (see sections 4.3 and 4.4 for further details). While this prevents us from studying fully three-dimensional problems, it provides significant computational savings. At each of these symmetry planes we apply the following conditions on the momentum equations:

$$\mathbf{n}_{sym} \cdot \mathbf{v} = 0, \tag{4.6a}$$

$$\mathbf{t_1} \cdot (\mathbf{n}_{sym} \cdot \mathbf{T}) = 0, \tag{4.6b}$$

$$\mathbf{t_2} \cdot (\mathbf{n}_{sym} \cdot \mathbf{T}) = 0, \tag{4.6c}$$

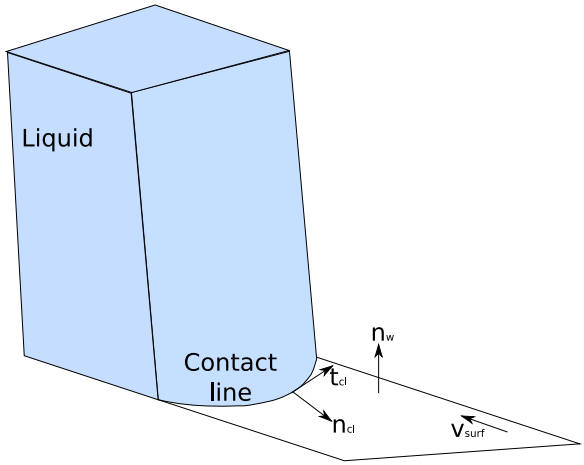

Figure 4.2: Schematic of a three-dimensional wetting line

where $\mathbf{n}_{sym}$ is an outward pointing normal to the symmetry plane, and $\mathbf{t_1}$ and $\mathbf{t_2}$ are tangent vectors in the symmetry plane.

In section 4.4 we allow the contact lines to move along the solid surfaces. To do this we apply conservation of mass at the contact line, using what Baer et al. (2000) refer to as an edge kinematic condition (see schematic in figure 4.2):

$$\mathbf{n}_{cl} \cdot (\mathbf{v} - \dot{\mathbf{x}}_{cl}) = 0, \tag{4.7a}$$

$$\mathbf{t}_{cl} \cdot (\mathbf{v} - \mathbf{v}_{surf}) = 0, \tag{4.7b}$$

$$\mathbf{n}_{w} \cdot (\mathbf{v} - \mathbf{v}_{surf}) = 0, \tag{4.7c}$$

where $\mathbf{n}_w$ is a vector that is normal to the solid surface, $\mathbf{n}_{cl}$ is a vector in the plane of the solid that is normal to the contact line, $\mathbf{t}_{cl}$ is a vector in the plane of the solid that is tangent to the contact line, and $\dot{\mathbf{x}}_{cl}$ is the velocity of the mesh at the contact line.

Because the contact line position is no longer fixed we specify the angle that the interface makes with the solid (the contact angle). To do this, we relate the contact angle to the velocity at the contact line using a linearized version of the molecular-kinetic model:

$$\cos\theta = \cos\theta_s - \Gamma Ca \left(\dot{\mathbf{x}}_{cl} - \mathbf{v}_{surf}\right), \tag{4.8}$$

where θ is the actual contact angle that the liquid makes with the solid, θ_s is the static contact angle and Γ is the coefficient of wetting-line friction (defined as ζ/μ in Blake, 2006). We note that the parameter Γ can vary over several orders of magnitude, from roughly 10 for water on polyethylene terephthalate (Blake, 2006) to nearly 1,000 for some silicone oils on glass (Ranabothu et al., 2005). In the limit that $\Gamma \to 0$ the velocity has no effect on the contact angle, and so the contact line maintains the static angle as it slips over the surface. In the limit that $\Gamma \to \infty$ the contact line velocity must approach zero so that the $\cos\theta$ term

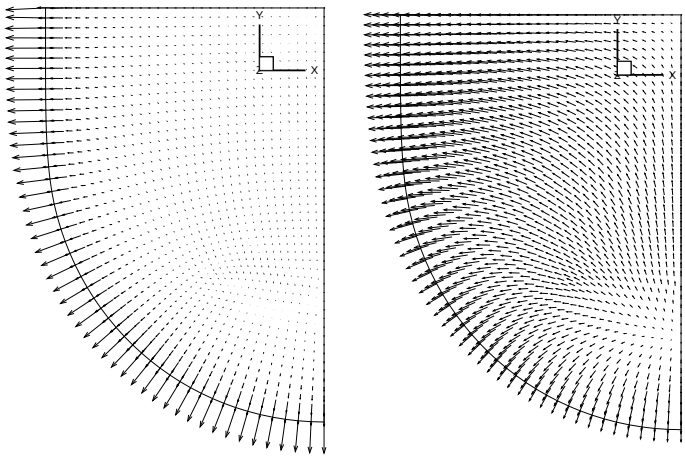

(a) (b)

Figure 4.3: Velocity vectors on a solid surface with a moving contact line for (a) $\beta = 10^{-2}$ and (b) $\beta = 10^{2}$

stays between -1 and 1. While this linear model cannot capture all the features of a real contact line, such as the hysteresis between the advancing and receding angles, it remains a useful tool because it allows the contact angle to vary along the wetting line. This is an important feature when modelling three-dimensional flows with moving contact lines, as can be seen when a drop of water slides down a surface (Baer et al., 2000). Finally, to avoid a well-known singularity in the stress as the contact line is approached (Huh and Scriven, 1971) we apply Navier slip along the solid surface when a wetting line is present:

$$\mathbf{t}_{cl} \cdot (\mathbf{n}_w \cdot \mathbf{T}) = \frac{1}{\beta} \mathbf{t}_{cl} \cdot (\mathbf{v} - \mathbf{v}_{surf}) \,, \tag{4.9}$$

where β is a slip parameter that controls the size of the region over which the contact line velocity dissipates to the no-slip condition. Figure 4.3 shows that for small β the velocity dissipates quickly, and no-slip is recovered after a short distance, whereas for larger values of β the velocity remains non-zero over most of the solid. We also note that whereas a smaller value of β produces a relatively constant contact line velocity in this particular example, when β is large the velocity over the solid clearly has a strong influence on the contact line velocity. Finally, taking a typical slip length on the order of 100 nm and a characteristic bulk length scale of 10 μm, we set $\beta = 10^{-2}$ for all computations in this work.

4.2.2 Numerical solution technique

In the previous section we constructed a set of time dependent, nonlinear equations that must be solved. We use the method of lines to separate the problem into a spatial component that is discretized using the Galerkin finite element method, and a time-dependent component that is solved using a second-order adaptive time-stepping scheme, as described in Gresho et al. (1980). We refer the reader to chapter 2 for specific details on the time-

stepping and finite element algorithms used in this chapter.

To track the moving interface we extend the elliptic mesh generation technique discussed by Christodoulou et al. (1997) to three dimensions. In this technique the moving interface is tracked by solving a set of diffusion equations which map the physical coordinates (x, y, z) of the mesh onto a cubic computational domain with coordinates (ξ, η, ζ):

$$\nabla_{\mathbf{x}} \cdot (D_\alpha \nabla_{\mathbf{x}} \alpha) = 0, \tag{4.10}$$

where $\alpha = \xi, \eta$, or ζ, $\nabla_{\mathbf{x}}$ indicates a gradient operator taken with respect to the physical coordinates, and the D_α can be thought of as diffusion coefficients for the mesh, which allow the mesh spacing to change dynamically as the domain changes shape. Equation (4.10) is solved for all three coordinates simultaneously with equations (4.1) and (4.2), producing a set of seven fully coupled PDEs. While the solution of this large equation set requires greater computational effort than solving the mesh and fluid equations separately, it provides a better convergence rate and a more accurate representation of the interface.

At this point it is worthwhile to compare the current mesh generation approach and the pseudo-solid mesh generation technique used by Cairncross et al. (2000), which is quite similar in formulation. With the pseudo-solid method the mesh is formed by solving a set of elliptic equations that govern the displacement of the mesh from an initial state, *i.e.*, the mesh displacement is treated as a fictitious solid mechanics problem. If the deformation from this initial mesh state becomes large the initial state must be reset, which is known as annealing. Because the diffusion-based technique developed here does not consider the initial state of the mesh, it does not explicitly require this annealing step. In fact, one can interpret the diffusion-based method as a special case of the pseudo-solid method which has automatic annealing at every iteration. An additional difference is that the pseudo-solid technique requires the mesh to be formulated in a normal-tangent reference frame to avoid the development of spurious mesh stresses at the boundaries, as discussed by Cairncross et al. (2000). The rotation of the equations is not a trivial task, and it requires significant analytical work to derive the residual equations and their derivatives in this new reference frame. With our diffusion-based technique the mesh stress is never computed, and so the method is insensitive to the orientation of the reference frame. Our approach is therefore much simpler to implement. The trade-off is that the pseudo-solid approach can be used with unstructured meshes, allowing it to be more broadly applied, whereas our diffusion-based technique cannot.

Our equation set is nonlinear because the interface position is unknown, and we therefore use the Newton-Raphson method to obtain a linear matrix problem of the form:

$$\left(\frac{1}{\Delta t}\mathbf{M} + \mathbf{J}\right)_{\delta^n} \left(\delta^{n+1} - \delta^n\right) = -\mathbf{R}|_{\delta^n}, \tag{4.11}$$

where δ is the solution vector containing the velocity, pressure and position unknowns, n

is the iteration number in the Newton-Raphson scheme, $\mathbf{R}$ is the residual vector, $\mathbf{J}$ is the Jacobian matrix, Δt is the time step size, and $\mathbf{M}$ is the mass matrix. The derivatives in the Jacobian and mass matrices are calculated analytically to ensure high accuracy and convergence rate when solving the system. We use Gaussian quadrature to evaluate all integrals in the assembly of $\mathbf{R}$, $\mathbf{J}$, and $\mathbf{M}$.

There are many techniques that can be used to perform the matrix inversion required to solve equation (4.11). Iterative solvers, such as the conjugate gradient and the generalized minimum residual (GMRES) methods, are the most commonly employed because they provide significant computational savings by solving equation (4.11) indirectly. However, we found that these techniques did not give satisfactory solutions for the stretching bridges studied in this work, where at late times the mesh elements would become elongated. We therefore perform a full Gauss-elimination step using the frontal solver package MUMPS (Amestoy et al., 2001). While this requires significantly more memory and computational time, it allows us to solve for the liquid bridge profile much closer to breakup.

4.3 Asymmetric stretching with pinned contact lines

We first validated our code with a variety of test problems. We compared results produced by our code for a cubic lid-driven cavity at $Re = 100$ to those in Ku et al. (1987), for a rotating bucket with a free-surface to those in Baer et al. (2000), and for an axisymmetric liquid bridge with both pinned and moving contact lines to those in 2. In all cases we observed excellent agreement between our results and those in the literature. We now consider how asymmetric stretching affects the breakup dynamics of liquid bridges with pinned contact lines.

4.3.1 Stretching with shear

We begin by studying the effect of a combined stretching and shearing motion on the breakup dynamics of liquid bridges. While shear is known to improve cavity emptying in gravure coating (Kapur, 2003), its effect is often ignored when studying printing processes (Darhuber et al., 2001; Huang et al., 2008; Dodds et al., 2009, 2011b). Work by Hoda and Kumar (2008) began to address this by showing that shear is required to completely empty a 2D-planar cavity, though by neglecting the azimuthal curvature of the bridge they are omitting physics that can significantly alter the breakup dynamics. In this section we evaluate the role of shear on the breakup of a three-dimensional liquid bridge with pinned contact lines that is stretched between two flat plates.

We assume that the liquid bridges are small relative to the size of the two rolls (see figure 4.1), so that the plates can be treated as flat surfaces and the rotation of the rolls can be ignored. During stretching the bottom surface remains fixed in place while the velocity

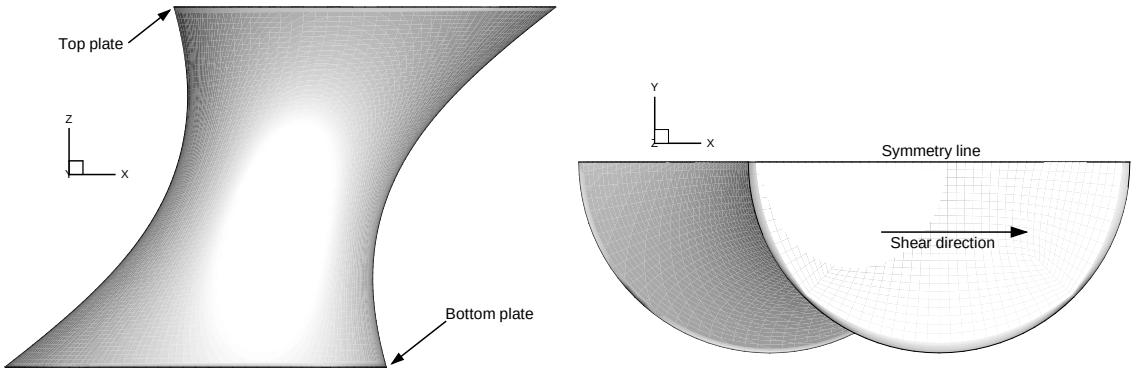

(a) (b)

Figure 4.4: Schematic of a liquid bridge undergoing both shear and extension, viewed from (a) the side, and (b) the top. A $y-z$ symmetry plane is used in this configuration.

of the top surface is set to a linear combination of shear and extension:

$$\mathbf{v}_{surf} = V\hat{\mathbf{i}} + U\hat{\mathbf{k}}, \tag{4.12}$$

where V is the shear velocity, U is the extensional velocity (set to 1 for all computations), and $\hat{\mathbf{i}}$ and $\hat{\mathbf{k}}$ are unit vectors in the x and z directions, respectively. Based on the work of Kapur (2003), V is expected to range from 0 to several hundred, depending on the relative speed of each roll, though in this work computational limitations restrict us to $0 \leq V \leq 1.4$. Because stretching occurs exclusively in the $x-z$ plane, a $y-z$ symmetry plane exists in the middle of the bridge, as seen in figure 4.4. Therefore, we solve for the dynamics of only one half of the bridge. The initial condition is a cylinder of static liquid between two flat, parallel plates, with a height and radius of equal magnitude.

We first note that, as one might expect, when V is increased the horizontal separation between the center of the bridge on each plate at breakup also increases. This increase in horizontal separation is accompanied by a decrease in the vertical separation between the two plates at breakup due to conservation of mass (results not shown). A more interesting observation is that the shape of the drops resting on either plate remain identical as stretching progresses, *i.e.*, the bridge is maintaining some level of symmetry about its breakup point (see figure 4.5). We can understand this result by noting that because the top plate is moving at a constant speed our system is frame invariant. We can therefore observe the stretching from the perspective of either plate and expect the same result. The relevant parameter governing breakup is therefore not the absolute velocity of either plate, but the *difference* in velocity between the two plates. This implies that the liquid is unable to distinguish one plate from the other, and so the amount of liquid resting on either plate after breakup must remain the same regardless of the shear or extensional velocity.

These are not obvious conclusions as the presence of an interface produces an inher-

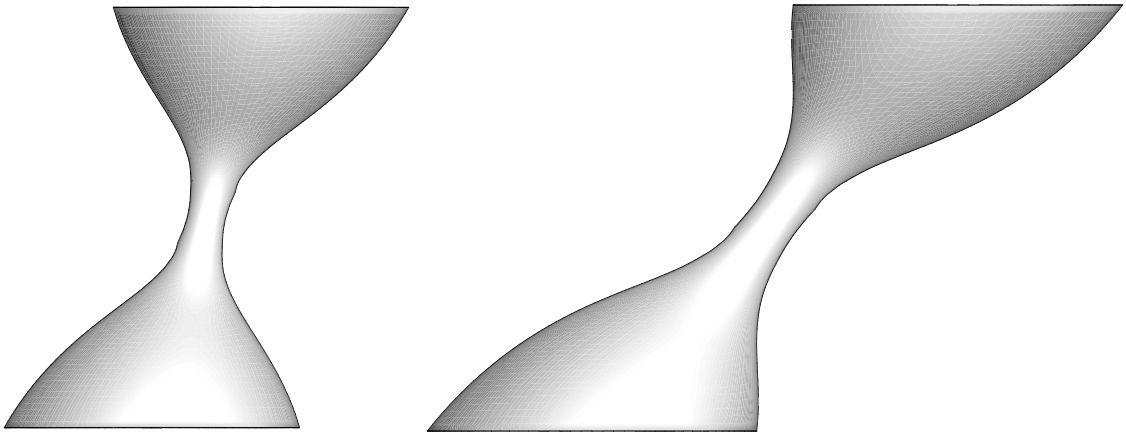

(a) (b)

Figure 4.5: Front view of liquid bridges near breakup for (a) $V = 0.4$ or (b) $V = 1.4$.

ently nonlinear equation set, and so it is difficult to tell beforehand what level of symmetry in the problem may or may not be maintained. Additionally, the interface has deformed significantly at breakup and does not maintain symmetry about its midpoint, so it is surprising that the distribution of liquid remains symmetric. Finally, it has been reported in the literature that when a liquid bridge is stretched over a cavity the presence of shear can help to improve cavity emptying (Kapur, 2003; Hoda and Kumar, 2008). Our results shed some light on this phenomenon by showing that a shearing motion alone cannot produce any change in the distribution of liquid on either plate, so long as the shearing motion remains frame invariant. Therefore, it must be the *combination* of a gravure cavity with the shearing motion that is responsible for the improved cavity emptying.

4.3.2 Stretching with rotation

In addition to the shearing motion discussed in the previous section, the cylindrical geometry of the rolls implies that rotational effects may become important if the liquid bridges are large enough. It has previously been assumed that this rotational effect can be approximated with only one rotating surface (Chuang et al., 2008), and we take the same approach here. The goal of this section is to understand how the combination of rotation and extension on one plate relative to the other alters the breakup dynamics and the liquid transfer. To model this motion we use a linear combination of stretching and solid-body rotation about the plate midpoint, so that the velocity of the top plate is given by:

$$\mathbf{v}_{surf} = -\omega z \hat{\mathbf{i}} + (\omega x + U)\,\hat{\mathbf{k}}, \tag{4.13}$$

where ω is the rotation rate, and U is set to 1 for all computations, as in the previous section. Typical gravure systems operate at rotation rates of up to 100 s^{-1}, which leads to a dimensionless range from 0 to roughly 0.5 when using characteristic length and velocity

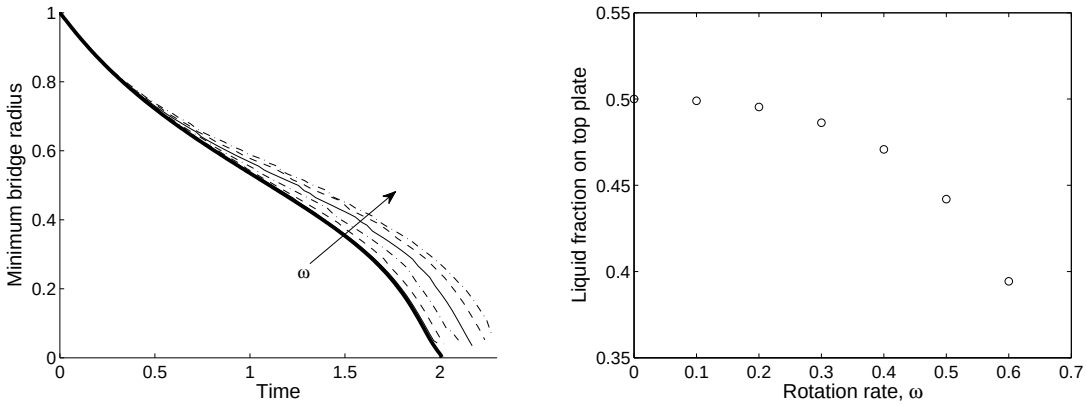

(a) (b)

Figure 4.6: (a) Minimum radius of the bridge vs. time for rotation rates from $\omega = 0$ to 0.6 in increments of 0.1. The thick line presents results at $\omega = 0$. (b) Fraction of liquid resting on the top plate after breakup versus the rotation rate.

scales of 500 μm and 0.1 m/s respectively. As in section 4.3.1 there exists a $y-z$ symmetry plane at the center of the bridge, and we solve for the dynamics of only one half of the bridge. The initial condition for these computations is the same as in section 4.3.1.

In figure 4.6(a) we plot the minimum radius of the bridge, calculated in the $y-z$ symmetry plane, versus stretching time for several values of ω. Here we see that at a given time the minimum bridge radius becomes larger as ω is increased, leading to a corresponding increase in the time to breakup. However, as ω is increased we also note that the liquid transferred to the rotating plate *decreases* (see figure 4.6(b)). Therefore, while the rotational motion stabilizes the bridge during stretching, allowing it to stretch to a greater extent, it also leads to a decrease in the liquid transfer to the rotating plate.

These two results can be understood by examining the axial velocity of the liquid. To isolate the effect of rotation from that of extension we subtract the extensional velocity from the axial velocity v_z, *i.e.*, $v_z'(x,z) = v_z(x,z) - Uz/z_{plate}(x)$, where z_{plate} is the position of the top plate. In figure 4.7 we plot contours of the velocity v_z' within the bridge for $\omega = 0.1$ and 0.6, with light gray indicating $v_z' > 0$, *i.e.* liquid moving to the top, and black indicating $v_z' < 0$, *i.e.* liquid moving to the bottom. For $\omega = 0.1$ capillarity remains the dominant force, and the effect of rotation is confined to a small region near the top plate. Because of this, v_z' is nearly symmetric about the bridge midpoint, with a plane of $v_z' = 0$ along the center of the bridge. Liquid is thus being pumped away from this plane toward both plates simultaneously, leading to a further thinning of the bridge and accelerating breakup. At $\omega = 0.6$ the effect of rotation has begun to overcome that of capillarity, and v_z' is negative in the majority of the liquid. This net downward flow explains the decrease in liquid transfer to the top plate when ω is increased, as seen in figure 4.6(b). Additionally, because the rotation has begun to dominate over capillary forces v_z' is no longer zero in the

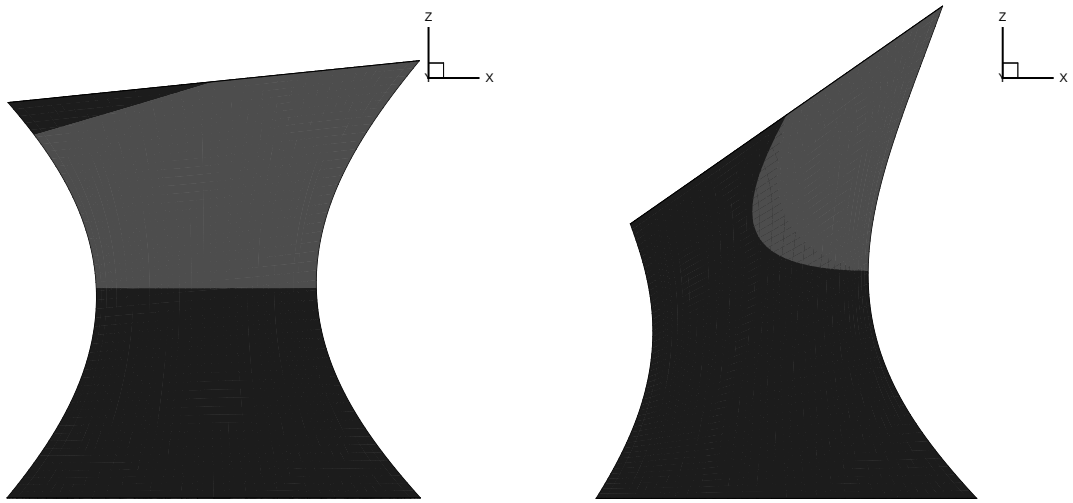

(a) (b)

Figure 4.7: Side views of the bridge at $t = 1.015$ for (a) $\omega = 0.1$ and (b) $\omega = 0.6$. The shades indicate the sign of the axial velocity v_z' after the contribution from the extensional velocity U has been subtracted. Light gray indicates liquid where v_z' is positive, and black liquid where v_z' is negative.

middle of the bridge, and therefore the capillary pumping mechanism that leads to breakup is temporarily overwhelmed by the rotation of the upper plate. This stabilizes the bridge, allowing it to stretch to a greater extent before capillarity produces rupture, as observed in figure 4.6(a).

This change in the distribution of liquid can be explained by noting that the rotating plate is no longer in an inertial frame of reference relative to the stationary plate. Therefore, if one wishes to observe the stretching motion in a reference frame fixed with the upper plate one must include additional fictitious forces to account for this acceleration. Therefore, one way to rationalize the results of this section is through a rotation-induced fictitious force that is driving liquid toward the stationary plate.

The implication of these results is that a mismatch in the size of the two rolls, which will produce a rotation of one roll relative to the other, can be used to produce changes in the amount of liquid transferred. Specifically, if the blanket roll is smaller than the backing roll in a gravure offset press (see figure 4.1), this will increase the liquid transferred to the moving substrate. This is a possible explanation for the success of microgravure coating, where a gravure roll with a small radius (2-5 cm) is used to produce extremely thin films (Hanumanthu, 1996).

4.4 Asymmetric bridge shapes with moving contact lines

In any printing process the primary goal is to reproduce a given pattern. This can be done in a variety of ways, though industrially it is often performed by first creating an image

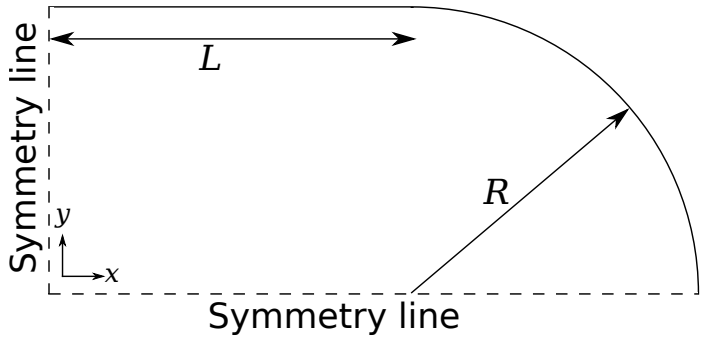

Figure 4.8: Schematic of the geometry used in section 4.4. For all computations presented here, $L = 0.5$ and $R = 1$

surface with a pattern embedded on it either chemically, as in lithographic printing (Lenz and Kumar, 2007), or mechanically with a series of engraved cavities, as in gravure printing (see figure 4.1). This allows the liquid to be located on the image surface only where it is needed, so that when the image is pressed against a substrate the desired pattern is reproduced. Therefore, while the amount of liquid transferred to the substrate is an important measure that can be used to gauge the success of a printing process, the ability to transfer the desired pattern to the substrate is also relevant. This pattern transfer is not guaranteed, as surface tension will drive the bridge toward a cylindrical geometry in an attempt to minimize the interfacial area, potentially destroying any pattern that may be present. Despite this importance, the fluid mechanics of pattern transfer has been examined in only one case (Darhuber et al., 2001), where it was shown that pattern transfer could be improved by using a high capillary number or a high substrate wettability. The goal of this section is to better understand how the dynamics of the contact line alter both the pattern and the liquid transfer during the stretching of a liquid bridge.

We have chosen to investigate a model geometry consisting of a bridge whose initial profile combines a rectangular inner portion of length $2L$, with two semi-cylinders of radius R at the left and right ends. While we will allow the surface properties of the two plates to be different from each other, the values of θ_s and Γ are treated as constant over each individual surface. In this geometry there exist two symmetry planes and we therefore solve for the dynamics of only one quarter of the bridge (see figure 4.8). For all of the computations presented in this section we have set $R = 1$ and $L = 0.5$, with an initial separation of 1 between the two plates. To obtain a suitable initial condition we allow the liquid bridge to relax from its initial geometry for a very brief amount of time ($\sim O(10^{-6})$) with the desired static contact angles, and with Γ and U set to zero on both plates. The solution at this point is then used as the initial condition for further stretching with $U = 1$ and the desired values of Γ on each plate. If this initial step was not performed, we found that spurious oscillations would develop in the contact line velocity that led to errors in the result.

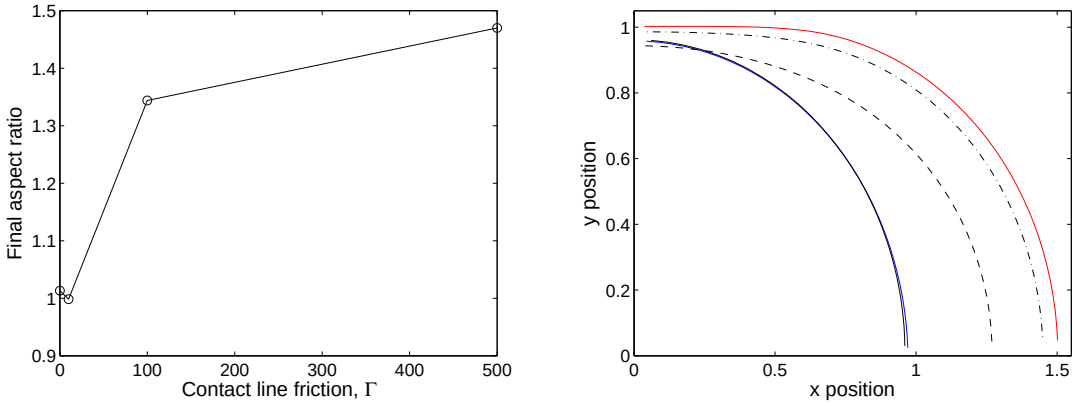

(a) (b)

Figure 4.9: (a) The final aspect ratio, defined in the text, versus Γ. (b) The contact line profile near breakup for $\Gamma = 0$ (blue), $\Gamma = 10$ (—), $\Gamma = 100$ (−−), and $\Gamma = 500$ (− · −). The red line indicates the initial interface profile before stretching. Stretching was performed with $\theta_s = 80°$ on each plate.

We begin by presenting results for a liquid bridge stretched between two plates with the same value of Γ and $\theta_s = 80°$. Figure 4.9(a) shows the final aspect ratio of the bridge, which is defined as the position of the contact line at breakup in the $x - z$ symmetry plane over that in the $y - z$ symmetry plane. When Γ is small the final aspect ratio is close to 1, indicating that the bridge is nearly cylindrical at breakup, whereas when Γ is large the final aspect ratio is close to 1.5, indicating that the bridge has nearly maintained its initial shape. We observe the same trend in the profile of the contact line at breakup, seen in figure 4.9(b). The shape of the bridge is thus strongly influenced by Γ, and these results indicate that some amount of dynamic wetting is necessary to maintain the fidelity of the original pattern under the conditions studied.

While figure 4.9 shows that the contact line friction plays a key role in pattern transfer, the results presented are for two identical plates. The breakup is thus symmetric about the bridge midpoint, and the size of the drops resting on either plate after breakup are equal. We now consider how a wettability difference interacts with Γ to produce variations in liquid and pattern transfer. We will consider cases where the static contact angles are $\theta_s^b = 80°$ on the bottom and $\theta_s^t = 60°$ on the top. Because Γ can have a different value on each plate, we label the contact line friction on the top and bottoms plates with Γ_t and Γ_b, respectively.

In figure 4.10 we show how the final aspect ratio and interface profiles on both plates are affected as Γ_b is varied. As expected, Γ_b has a significant effect on the contact line profile on the bottom plate (figure 4.10(c) and (d)), with a low value of Γ_b resulting in a small, nearly cylindrical contact area. However, Γ_b has very little effect on the contact line on the top surface for the conditions studied (figure 4.10(a) and (b)). In chapter 2, where we used a two-dimensional axisymmetric Stokes flow model with $\Gamma_t = \Gamma_b = 0$, we found that both

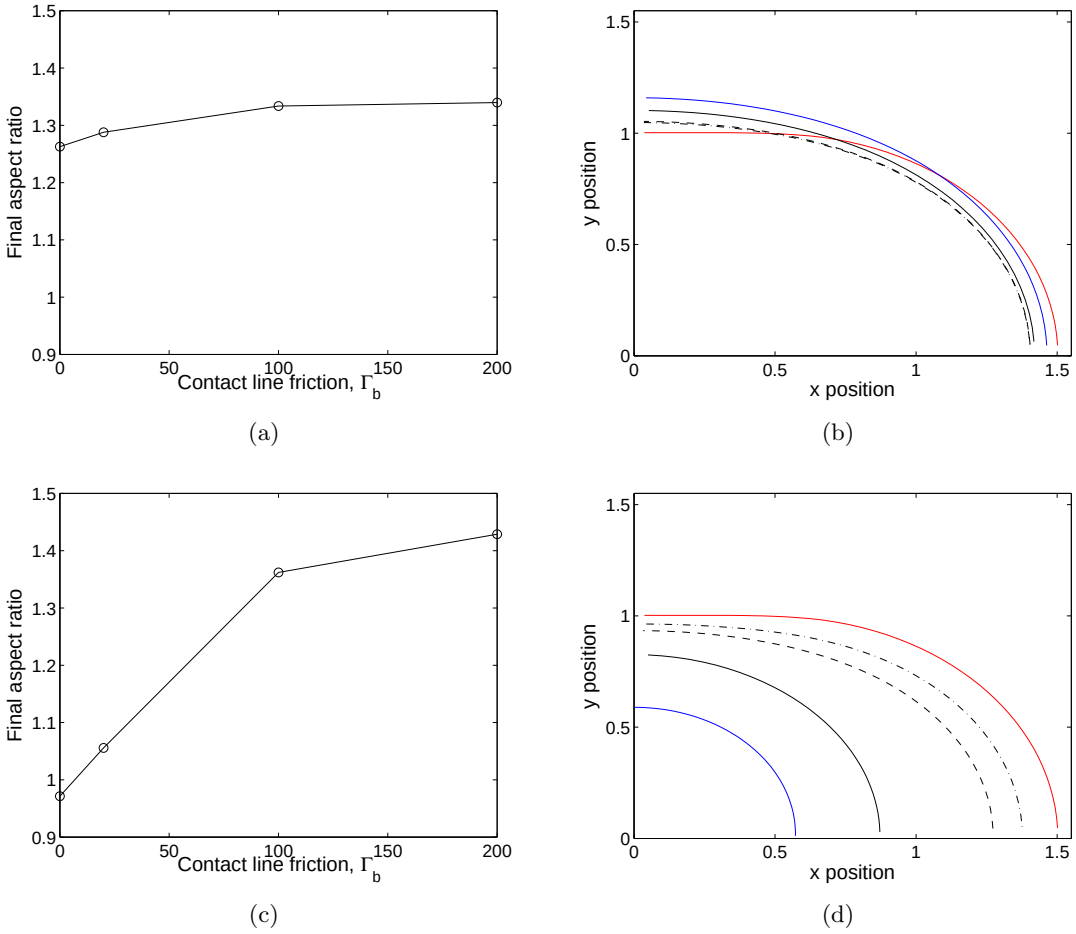

Figure 4.10: (a) The final aspect ratio on the top plate versus the contact line friction on the bottom plate, Γ_b. (b) The contact line profile near breakup on the top plate for $\Gamma_b = 0$ (blue), $\Gamma_b = 10$ (—), $\Gamma_b = 100$ (−−), and $\Gamma_b = 200$ (− · −). The red line indicates the initial interface profile before stretching. Panels (c) and (d) are analogs to panels (a) and (b) for the bottom plate. Stretching was performed with $\theta_s^b = 80°$, $\theta_s^t = 60°$, and $\Gamma_t = 100$.

the wettability of the individual plates as well as the wettability difference between the two plates significantly alters the shape of the bridge at breakup. Therefore, it is surprising that the dynamics of the two contact lines appear to be decoupled when $\Gamma \neq 0$, as we have shown here when $\Gamma_t = 100$. This indicates that the contact line friction diminishes the influence of each plate on the other by reducing the velocity with which the contact line slips over the surface.

While the pattern transfer to the top plate is not strongly influenced by Γ_b, the liquid transfer to the top plate decreases significantly as Γ_b is increased (see figure 4.11). This is because the contact line is able to slip easily off of the bottom surface when Γ_b is small, allowing the top surface to receive a larger fraction of liquid. When Γ_b is increased to 200 the breakup becomes nearly symmetric, as both contact lines have slowed to the point that the effect of the wettability of each surface is negligible. The amount of liquid resting on either

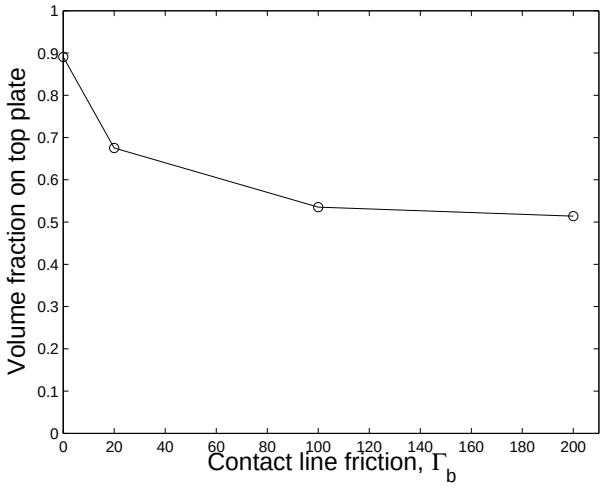

Figure 4.11: Volume fraction of liquid resting on the top plate for the computations presented in figure 4.10

plate therefore approaches 50%. This is similar in nature to stretching at a high capillary number where the effect of wettability is overcome by that of viscosity, and so the bridge also breaks symmetrically about its midpoint. However, the contact line friction allows for a greater degree of control because it is a local effect, so one can choose a liquid/solid combination to produce a difference in Γ that drives liquid from one surface to the other. We note that, in addition to Γ being a property of a given liquid/solid combination, recent work has shown that it can be adjusted by roughly an order of magnitude using surface charge (Puah et al., 2010). This gives the experimenter additional control over the contact line dynamics, and allows them to tune their system to achieve the desired result. In contrast, because the capillary number affects only the bulk liquid, using a high Ca to overcome an adverse wettability difference will always tend toward symmetric breakup. Finally, these results highlight the importance of considering dynamic wetting, as we have shown that for the conditions studied here the static contact angle and capillary number are not enough to fully characterize the dynamics of liquid bridges.

4.5 Conclusions

In this work we have shown that even simple deviations from axisymmetry can produce drastic changes in the dynamics of stretching liquid bridges. When an initially cylindrical bridge is stretched under both shear and extension we find that, regardless of the shearing speed, the drops resting on either plate have the same shape and volume after breakup due to the frame invariance of the system. This is in contrast to the behavior of a bridge that is stretched under both extension and rotation, where a rotation-induced fictitious force develops that drives liquid toward the stationary plate. The nature of the stretching

motion, and in particular the acceleration of one plate relative to the other, thus has a significant effect on the bridge dynamics and the transfer of liquid.

If we stretch a non-cylindrical liquid bridge while allowing the contact lines to move we find that as the contact line friction is increased on a surface the contact line velocity on that surface decreases, effectively pinning the contact line at a high enough Γ. Therefore, by using a substrate with a high value of Γ it is possible to significantly increase the amount of liquid resting on that surface after breakup, while maintaining the fidelity of the initial bridge shape. This result is of key importance in many printing processes, where the goal is to reproduce a desired pattern.

The work presented here is an important extension of the existing literature on stretching liquid bridges which has, with only a few rare exceptions (Darhuber et al., 2001; Walkley et al., 2005a; Bonito et al., 2006), been confined to two-dimensional studies. Although the specific cases we examine focused on the gravure offset printing process, the physical understanding gained through this work can be applied more broadly to any liquid bridge system. While the liquids studied in this chapter are Newtonian, industrial printing inks often contain particulate or polymeric additives which can alter the rheology of the liquid. It is thus important to understand how non-Newtonian effects are able to alter the dynamics of the bridge. In particular, viscoelasticity is known to produce fascinating star-like instabilities during the stretching of liquid bridges (Rasmussen and Hassager, 1999; McKinley and Sridhar, 2002), and an understanding of how such effects combine to alter liquid and pattern transfer during printing promises to be an exciting area for further study.

CHAPTER 5

Stretching liquid bridges with bubbles

Liquid bridges containing bubbles are relevant to industrial printing, and are also a topic of fundamental scientific interest. We use flow visualization to study the stretching of liquid bridges, both with and without bubbles, at low capillary numbers. We find that while the breakup of wetting fluids between two identical surfaces is symmetric about the bridge mid-point, contact line pinning breaks this symmetry at slow stretching speeds for non-wetting fluids. We exploit this observation to force air bubbles selectively towards the least hydrophillic plate confining the liquid bridge.[1]

5.1 Introduction

Stretching liquid bridges are found in numerous industrial (Powell et al., 2002; Yao and McKinley, 1998; Vogel and Steen, 2010) and natural (Vogel and Steen, 2010; Reis et al., 2010; Prakash et al., 2008) systems, and as such, they have been a focus of research for over a century (Eggers and Villermaux, 2008). Of particular importance in many of these cases is the wettability of the solid surfaces, which can significantly alter the stretching and breakup dynamics of the bridge, as we saw in the previous three chapters. However, the presence of a moving contact line complicates both experimental and computational analysis of liquid bridges, and so has received relatively little attention despite its fundamental importance (Chadov and Yakhnin, 1979; Darhuber et al., 2001; Gupta et al., 2007; Cai and Bhushan, 2008; Balu et al., 2009; Dodds et al., 2009; Kusumaatmaja and Lipowsky, 2010; De Souza et al., 2008; Huang et al., 2008; Kang et al., 2009; Qian et al., 2009; Villaneuva

[1]This chapter is reproduced with minor modifications from S. Dodds, M. S. Carvalho, and S. Kumar. "Stretching Liquid Bridges with Bubbles: The Effect of Air Bubbles on Liquid Transfer", *Langmuir*, **27** (2011) 1556-1559

et al., 2007; Panditaratne, 2003).

The dynamics of bubbles are also believed to be important in various applications, such as the formation of aerosols (Bird et al., 2010), the debonding of adhesives (Foteinopoulou et al., 2004), and in industrial printing. In printing processes such as gravure or flexography, bubbles can become trapped in the liquid bridge which connects the image and the substrate. These bubbles can reduce the amount of liquid transferred to the substrate, resulting in a defect known as spackle. This is a potentially catastrophic defect in the manufacture of printed electronics, where any gap in the final pattern could ruin the entire device.

The goal of this chapter is to understand the role of bubbles on the dynamics of stretching liquid bridges, where the authors are aware of only three studies, all computational, that have been published to date (Foteinopoulou et al., 2004, 2006; Chatzidai et al., 2009). These studies do not consider the role of surface wettability on either the liquid bridge or the bubble dynamics, and thus are unable to evaluate the effect that the bubble may have on liquid transfer. We also examine how the stretching of non-wetting fluids differs from that observed with wetting fluids, which is of fundamental scientific importance.

5.2 Experimental Details

The apparatus used in this chapter is shown in figure 5.1. A glass microscope slide was used for the bottom plate, and a steel post 3.25mm in diameter was used for the top plate. Both plates could be covered with one of polyethylene terephthalate (PET), low-density polyethylene (LDPE), or polyoxymethylene (Delrin), allowing for the variation of the wettability of either plate (table 5.1). A 1μL drop of distilled water was placed onto the bottom plate and, for certain experiments, a 0.1μL air bubble was inserted into the drop with a syringe (Hamilton company, model 7001KH). The upper plate was brought into contact with the water, and the drop was compressed. The upper plate was then pulled away from the bottom, stretching the bridge at a constant velocity. In experiments performed with bubbles, the bubble was initially in contact with *both* plates before stretching. The stretching was visualized using a high-speed camera, with a frame rate of 60 to 3,000 frames per second, depending on the stretching speed.

Results were quantified using ImageJ analysis software (Abramoff et al., 2004). Fluid volumes were calculated using Pappus' theorem, which relates the volume of a solid of revolution to its cross-sectional area in the $r - z$ plane. Because this analysis technique assumes an axisymmetric drop shape, we are unable to account for asymmetries in the drop shapes. However, the calculated drop volume, both before and after stretching, was generally within 10%, and often within 5% of the expected volume of 1μL, indicating that our analysis is reasonably accurate.

The maximum stretching speed used in these experiments was 69.3mm/s, and the characteristic length scale for the drop was on the order of 0.5mm. Therefore, the maximum

Table 5.1: Material characteristics used in this chapter, where θ_a and θ_r are the advancing and receding contact angles

Material	θ_a	θ_r
LDPE	95.9±2.9°	79.8±3.6°
PET	78.5±1.8°	60.4±2.5°
Delrin	68.5±3.4°	23.0±4.1°

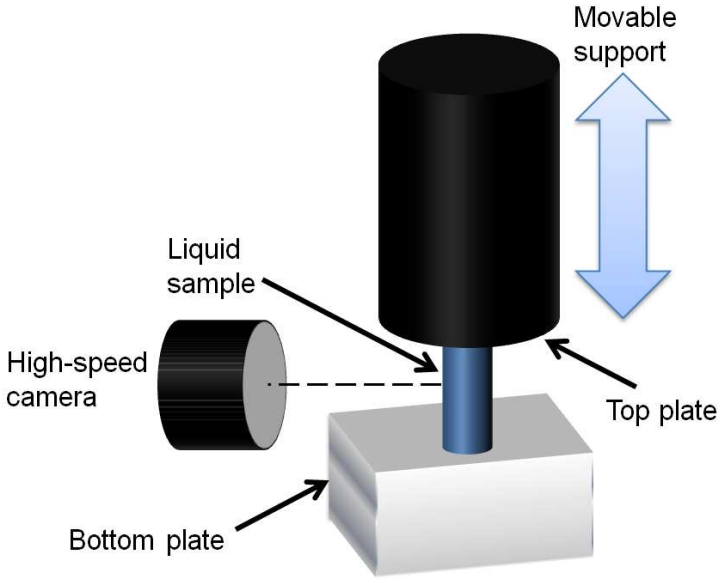

Figure 5.1: Schematic of the apparatus used for the experiments in this chapter.

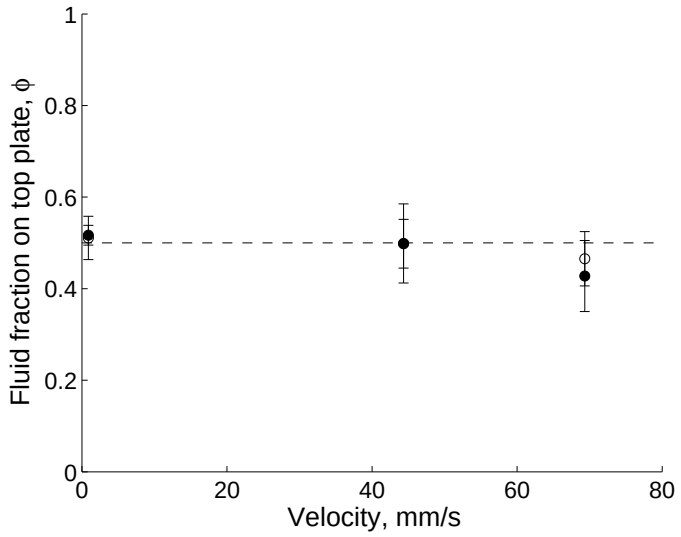

Figure 5.2: Fraction of fluid resting on the top plate after bridge breakup for pure water (∘) and water with an air bubble (•). Both the top and bottom surfaces were covered in PET. The dashed line represents $\phi = 0.5$.

capillary, Weber, and Bond numbers were on the order of 10^{-3}, 0.01, and 0.1, respectively, indicating that surface tension dominates inertial and viscous forces. While the Bond number suggests that gravitional effects may be important, we did not observe this to be the case, within our experimental error. Additionally, Slobozhanin and Perales (1993) found that, for the experimental conditions studied here, there was a negligible difference in the stability of a liquid bridge between a Bond number of 0 and of 0.1 (see supporting information at the end of the chapter), further supporting our assumption that gravitational forces do not play a significant role in our experiments.

5.3 Results and discussion

We first studied the stretching of water between two PET surfaces. Figure 5.2 shows the volume fraction of fluid resting on the top plate after breakup, ϕ, for different stretching speeds. The volume of fluid on the top plate is found to be the same as on the bottom plate, giving $\phi \approx 0.5$, regardless of the stretching speed. Because the effects of inertia and gravity are small in our experiments, any hydrodynamic force that might move the fluid preferentially towards one surface or the other is small. In addition, because the two plates are covered with the same material, there is no wettability difference to drive fluid towards one plate or the other. Therefore, it is expected that the breakup should be nearly symmetric about the bridge mid-point.

When an air bubble is introduced into the bridge prior to stretching, the volume of fluid on the top plate is still the same as on the bottom plate, where we use the term fluid to

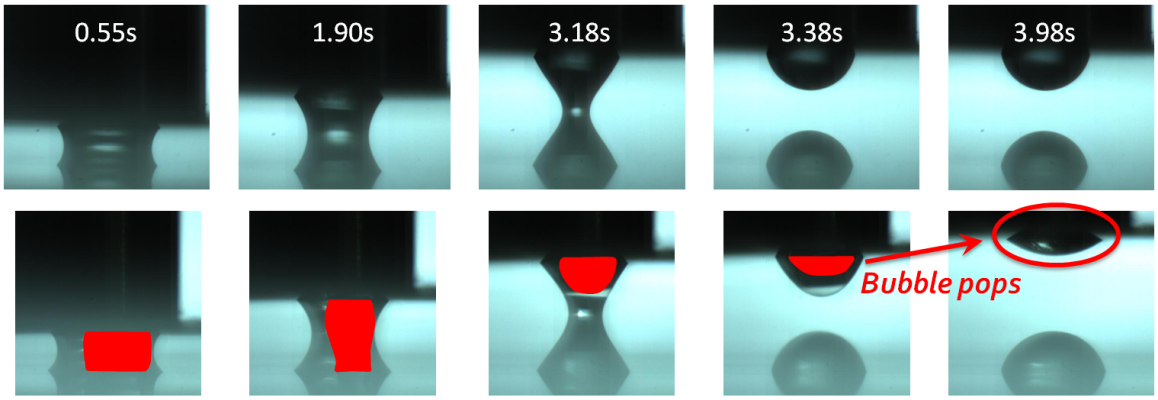

Figure 5.3: Time-series of images taken during stretching of a bridge without a bubble (top) and with a bubble, highlighted in red (bottom). The bridges were stretched between two PET surfaces, at a speed of 0.89mm/s.

refer to the total volume of liquid and gas. This suggests that the presence of the bubble does not have an effect on the breakup of the liquid bridge. To understand this result, it is helpful to examine a time-series of images taken during stretching, both with and without a bubble (see figure 5.3). Comparing the shape of the outer air/liquid interface at a given time, there is virtually no difference in the shape of the interface with or without a bubble. This indicates that the dynamics of the two interfaces are decoupled, and so the outer interface evolves as if no bubble is present.

Examination of the dynamics of the bubble in figure 5.3, which has been highlighted in red (images are included without modification in the supporting information at the end of the chapter), shows that the air bubble slips entirely off of the bottom surface and onto the top surface. Therefore, while the volume of fluid on the top plate is the same as on the bottom, the volume of *liquid* on the top plate is significantly lower. This is highlighted in the final two panels of the bottom series in figure 5.3, where the bubble pops, leaving behind only the liquid that was transferred to the top surface. It should be noted that, while the bubble slips onto the top surface in figure 5.3, we observed it resting on the bottom surface with equal frequency. This indicates that the bubble motion is not buoyancy driven.

The effect of stretching speed on bubble breakup is shown in figure 5.4. As was noted in the previous paragraph and in figure 5.3, at slow speeds the bubble slips entirely off of one surface and onto the other. However, at faster speeds, the bubble breaks up near its centre, resulting in breakup that is more symmetric than at slower speeds. That we observe the symmetry of the bubble dynamics breaking as the speed is *decreased* is a surprising result, because one would expect surface tension, which is the dominant force in this system, to maintain symmetry during stretching for two plates that are covered with the same material.

One possible explanation for this behaviour is that wetting fluids (water on PET) behave in a different manner during stretching than do non-wetting fluids (air on PET). Some evidence for this is provided in figure 2.8(a), which shows the computed interface profile

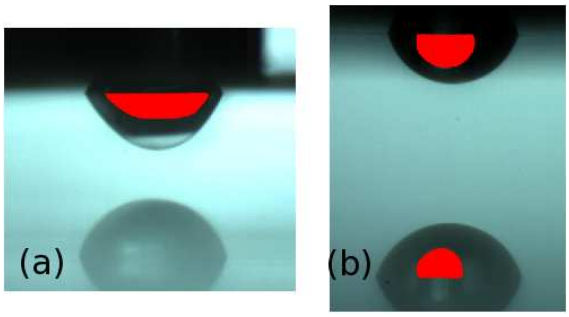

Figure 5.4: Comparison of the bubble position for (a) slow stretching speeds (0.89mm/s) and (b) fast stretching speeds (61mm/s), for water stretched between two PET surfaces.

just before breakup for the stretching of a non-wetting liquid bridge between two identical plates. These computations indicate that while the breakup of the bridge remains symmetric about its mid-point, as one would expect since the plates are identical, the thinnest portion of the bridge is now located near the two plates, instead of at the centre. This change in behaviour can be rationalized by noting that, because the fluid is non-wetting, it will attempt to dewet the two plates as the bridge is stretched. If the stretching rate is slower than the dewetting rate, then the contact lines will move quickly enough to slip off of both plates, and the bridge will break at the solid surfaces, instead of near its centre.

Because the bridge is connected to the plates by thin fluid threads, the region with the highest capillary pressure is near the contact lines. If one of the two contact lines pins, say on the top surface, while the other contact line continues to slip (as in the second panel on the bottom in figure 5.3), then the highest pressure in the bridge will be at the bottom plate. This high pressure causes more fluid to be pumped away from the bottom plate, further thinning the connecting fluid thread, and eventually driving all of the fluid off the plate. Because the contact line pinning should be due primarily to surface roughness, which surface the bubble pins on will be random. This explains why, at slow speeds, the bubble rests on both surfaces with equal frequency. Additionally, as the stretching rate is increased, the contact lines will no longer have time to completely dewet one surface, forcing breakup closer to the centre of the air column instead of at one of the two plates, as is observed in figure 5.4(b).

If the behaviour of the bubble is related purely to the wetting dynamics of the air on the PET surface, as we suggest, and has nothing to do with any interaction between the bubble and the outer gas/liquid interface, then identical behaviour should be observed for a single, non-wetting fluid, which presents a simpler system to study and understand. Figure 5.5 shows the liquid fraction of the largest drop vs. stretching velocity for water between two LDPE plates. This presents a system where the liquid is non-wetting, in contrast to figure 5.2, where the liquid is wetting and the air non-wetting. It should be noted that the largest drop was found on the top and bottom surface with equal frequency over all

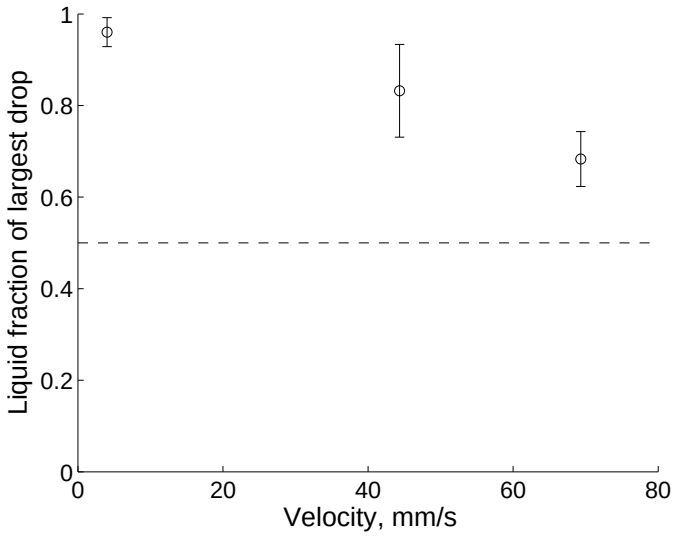

Figure 5.5: Fraction of fluid composing the largest drop after bridge breakup for stretching between two LDPE plates. The dashed line represents $\phi = 0.5$.

stretching speeds (see supporting information at the end of the chapter). For slow stretching speeds, the liquid is found almost entirely on one surface or the other. As the stretching speed is increased, however, the size of the largest drop begins to decrease, approaching the expected result of $\phi = 0.5$ for a fluid stretched between two identical plates. Therefore, water between two hydrophobic surfaces exhibits the same behaviour as the more complex liquid bridge/bubble system from figure 5.3, supporting our hypothesis that the bubble motion is governed by wetting and contact line pinning, and not by any hydrodynamic interactions between the water and the bubble.

If we now consider a liquid bridge system with two chemically different surfaces, PET and Delrin, then the air bubble should wet the PET preferentially[2], even though air is not a wetting fluid on either surface. In addition, we showed in chapter 2 that small differences in wettability have been shown to produce large differences in liquid transfer for non-wetting fluids, and we therefore expect that the entire bubble will slip onto the PET surface, leaving only water on the Delrin. While it is difficult to accurately measure the volume of the bubble because of the resolution of the bubble interface, we find that the bubble does appear to have transferred entirely to the PET surface after breakup, regardless of the stretching speed (see supporting information at the end of the chapter).

In the PET/Delrin systems, the bubble would nearly always pop after stretching. We can therefore compare the volume of the drop, both before and after popping, to get an estimate of the size of the bubble on each surface (figure 5.6). We find that there is a negligible change in volume for the drop on the Delrin surface, indicating that if any air remains, it did not pop during visualization. We also find that the drop on the PET consistently decreases

[2]since $\theta_{air} = \pi - \theta_{water}$, $\theta_{air} > \pi/2$

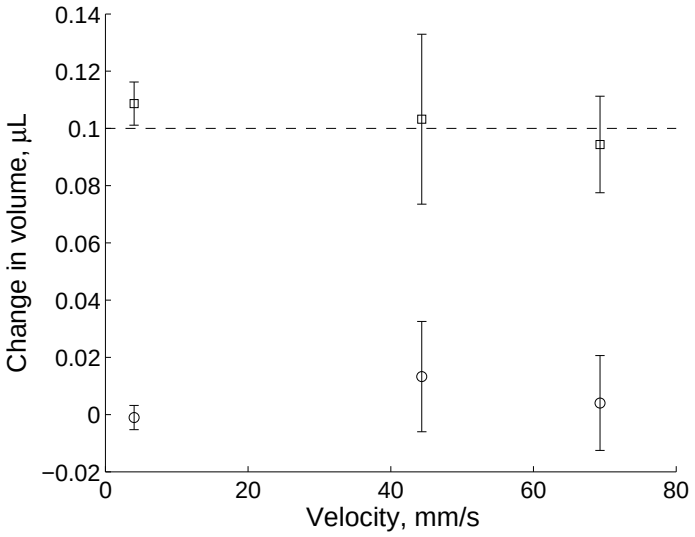

Figure 5.6: Change in volume of the fluid drop resting on Delrin (○) or PET (□), after the bubble pops. The dashed line represents the initial bubble volume inserted into the drop, 0.1μL.

in volume by approximately 0.1μL, which is the volume of the bubble originally inserted into the drop before stretching. This supports our hypothesis that the bubble has moved entirely to the PET surface, leaving only water on the Delrin surface.

The time between breakup and the bubble popping was on the order of one second. In an industrial printing process, where the pattern may dry within milliseconds of being printed, it is possible that the bubble does not pop, but is instead dried into the final product. This type of defect could go unnoticed in graphics arts applications, because the bubble may not make the printed feature visibly different from a feature that had printed correctly. However, a bubble in a printed circuit could significantly alter the electrical properties of the device. This highlights the importance of understanding and controlling the dynamics of the bubble during printing, as we have attempted to do here.

The work presented in this chapter has shown that the breakup behaviour of a non-wetting fluid stretched between two plates is fundamentally different from that of a wetting fluid. When the two solid surfaces are made of the same material, we find that at slow stretching speeds a non-wetting fluid will slip entirely onto whichever surface its contact line first pins on. This behaviour was found to be robust, occurring both when water alone was stretched between hydrophobic plates, and when water with an air bubble was stretched between hydrophilic plates. We were then able to use a wettability difference between the two plates to drive the bubble selectively toward the most hydrophobic plate, allowing us to remove the bubble defect entirely from one of the plates.

5.4 Supplementary information

5.4.1 The effect of gravity

To determine the importance of gravity in our systems, we look to Slopozhanin and Perales, Phys. Fluids A, 1993, Vol. 5, hereafter referred to as S&P. In this work, Slobozhanin and Perlaes, calculated the stability of liquid bridges between two equal disks in a gravitational field. First, we would like to note that the analysis of S&P is restricted to pinned contact lines and so, strictly speaking, is not applicable in our experiments. However, we found that the contact line would pin well before breakup in our experiments, allowing us to use the analysis from S&P. While it is difficult to determine the exact reason for this pinning, we believe it is due to contact line hysteresis. During stretching, the contact line will initially recede. At late times, our 2D-axisymmetric computations (chapter 2) show that as the capillary pressure builds up in the bridge, and fluid begins to be pumped from the neck towards the substrates, the contact line velocity switches sign, and the contact line begins to advance along the surface, causing the drop to spread. In a real system, however, once the contact line velocity becomes small enough, the contact line will pin in place until the interface has deformed enough that the contact angle is equal to the advancing angle, at which point the drop will begin to spread. This pinning prevents us from comparing our computational results directly to our experiments, because our computations cannot currently capture such complex contact line behaviour, and so we do not observe quantitative agreement between our model and our experiments. However, this pinning is also what allows us to use S&P's analysis with some confidence.

If we revisit the experiment shown in the top series of fig. 5.3, we can obtain the length of the bridge and radius of contact area between the liquid and solid, one frame (∼17ms) before breakup is observed. From our results (and using the notation of S&P), R=0.64mm, L=1.63mm and V=0.87mm^3. To compare to the analysis presented in S&P, we calculate $\mathbf{V}=V/(\pi LR^2)$=0.415 and $\Lambda=L/2R$=1.27. If we then compare these values to Fig. 2 in S&P, we see that for Λ=1.27, we get $\mathbf{V}$ of approximately 0.42, which agrees with our experimental finding. This indicates that the analysis performed in S&P is valid for our experiments, as we argued in the previous paragraph, and can be used here to understand the effect of gravity.

At these values of $\mathbf{V}$ and Λ, the curve for the stability envelope at a Bond number of 0 is indistinguishable from the curve for a Bond number of 0.1 or even 0.2 (fig. 4a of S&P). This implies that the shape of the interface near breakup for Bo=0.1 is identical to that for Bo=0 under these conditions, and thus that gravity does not play a significant role on the stability of the bridge. Therefore, one would not expect that the breakup of the bridge would produce significantly different drop shapes after breakup between the Bo=0 and Bo=0.1 cases. However, we do not exclude the possibility that gravity is affecting the results within our experimental error.

5.4.2 Supplementary figures

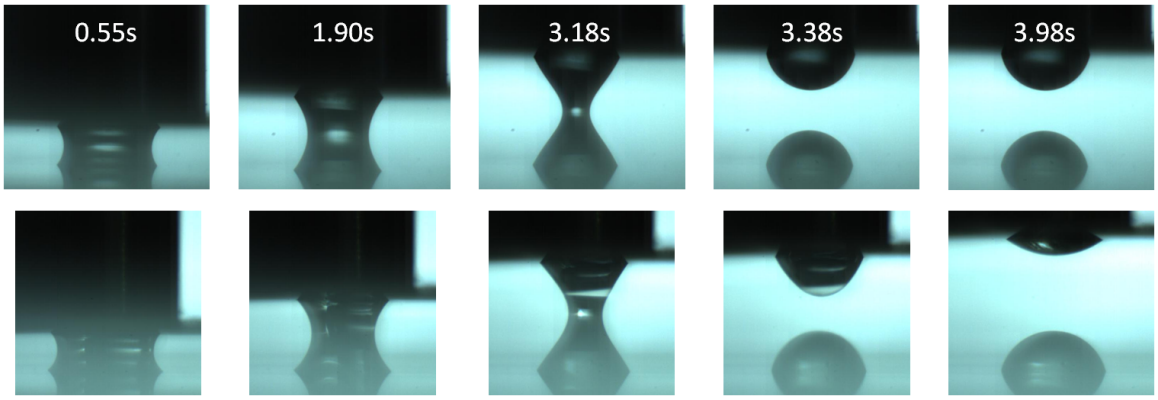

Figure 5.7: Figure 5.3, without highlighting the location of the bubbles. The bubbles can be discerned by a slight change in the way the light is refracted through the bridge.

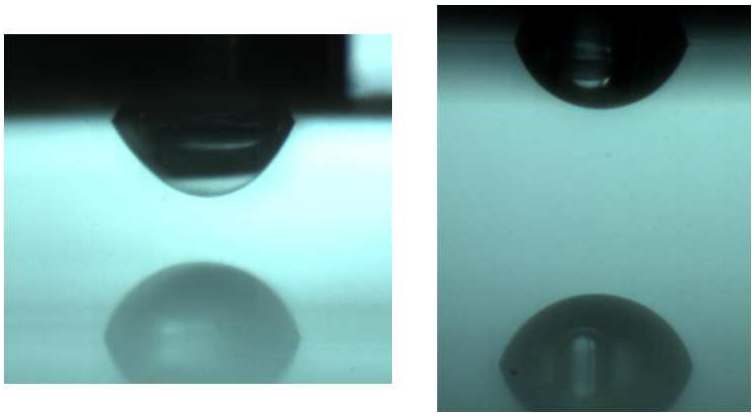

Figure 5.8: Figure 5.4, but without highlighting the bubble location.

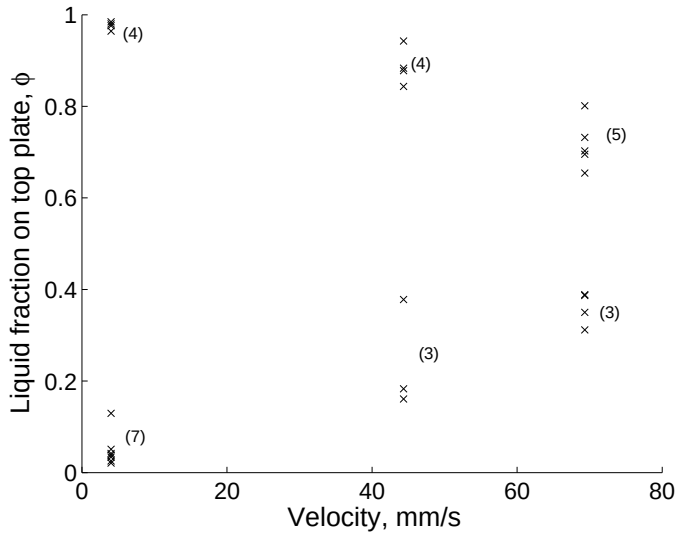

Figure 5.9: The data used to construct figure 5.5. Each mark represents the fraction of liquid on the top plate for an individual experiment. The number in brackets next to each cluster of data represents the number of experiments that compose each cluster. In total, the largest drop rested on the top surface 13 times, and on the bottom surface 13 times.

CHAPTER 6

Final remarks

In this thesis we have considered several model problems that were motivated by a desire to better understand the dynamics of liquid bridges with moving contact lines, with an emphasis on the liquid transfer process in gravure printing. In this chapter we summarize our key findings, and suggest future research directions to further understand this liquid transfer process.

6.1 Conclusions

In chapters 2 through 4 we used the Navier-Stokes equations to study stretching liquid bridges with moving contact lines. In chapter 2 we solved Stokes equations for a two-dimensional axisymmetric liquid bridge between either two flat plates or a flat plate and a cavity. We found that while the wettability of the two surfaces is a key factor in controlling liquid transfer when both of the surfaces are flat, the presence of a cavity on one of the surfaces alters the dynamics significantly. In this case the contact line effectively pins along the cavity wall, causing the liquid transfer to the flat surface to decrease. Cavity designs can therefore be improved by minimizing this contact line pinning. If the cavity is made less wettable the contact line will slip more easily along its wall, improving cavity emptying. However, to avoid defects during printing the wettability of the cavity must be high enough that the cavity can be properly filled and doctored. Another way to minimize contact line pinning is to consider the cavity geometry. If the cavity is made wider (for a fixed depth), the contact line will have more time to slip down the cavity wall before breakup, improving emptying. Alternatively, if the slope of the cavity wall is made less steep contact line pinning will be less pronounced, again improving emptying. There are therefore several parameters that can be adjusted in the design of gravure systems to optimize the liquid transfer.

Contact line pinning was also shown to be relevant in the formation of satellite drops during stretching at non-zero Reynolds numbers (chapter 3). In the presence of inertia the bridge must map onto a similarity solution that is asymmetric about the pinch-off point as breakup is approached. This asymmetry pushes the pinch-off location toward whichever surface has the larger contact radius with the liquid, decreasing liquid transfer to that surface. The pinned contact line will naturally have a large contact radius, often resulting in an increase in cavity emptying as the Reynolds number is increased. However, as the flat surface (web) is made more wettable a second pinch-off location can form near the web, resulting in the production of a satellite drop. While the work presented in chapter 2 suggests that optimal operating conditions include using the most wettable web possible, the work presented in chapter 3 shows that when inertia is present the web wettability should be balanced with the increased tendency of the liquid to form satellite drops during breakup.

In chapter 4 we relax the assumption that the liquid bridges are axisymmetric, and we present results on the stretching of a three-dimensional liquid bridge between two flat plates. We find that the acceleration of the plates relative to each other is a key factor in controlling the distribution of liquid after breakup when the contact lines are pinned and the bridge is stretched asymmetrically. If the plates are separated from each other at a constant velocity the frame-invariance of the system dictates that the liquid must be evenly distributed, as observed when extension and shear are present (§4.3.1). However, if one of the plates is accelerating relative to the other then additional fictitious forces can arise, depending on the reference frame chosen (§4.3.2). This produces an asymmetry in the breakup, and in the case of a combined extension and rotational motion results in a decrease in the amount of liquid resting on the rotating plate after breakup.

Another case where three-dimensional effects may play a role is in the stretching of non-cylindrical features, examples of which are printing a letter or a line instead of a pixel. Because surface tension will attempt to drive the bridge toward axisymmetry, a better understanding of the conditions under which the pattern is able to maintain its original shape after breakup is relevant. In §4.4 we find that the contact line friction plays a key role in pattern transfer by slowing the movement of the wetting line over the solid. Therefore, if two systems have the same wettability and capillarity, the manner in which the contact line slips over the surface can still produce significantly different results between each system. This highlights the importance of dynamic wetting in printing processes, which has not previously been recognized.

In chapter 5 we used flow visualization to study the stretching of liquid bridges between both hydrophobic and hydrophillic surfaces. In particular, we examined the effect of small, non-wetting air bubbles on the breakup of liquid bridges. We found that the dynamics of non-wetting fluids stretched between two flat plates are fundamentally different from those of wetting fluids. When the two solid surfaces are made of the same material, a non-wetting

fluid stretched at slow speeds slips entirely onto whichever surface its contact line first pins on. This behavior is robust, occurring both when water alone is stretched between hydrophobic plates, and when water with an air bubble is stretched between hydrophilic plates. To remove the bubble entirely, one can use a wettability difference between the two plates, as the bubble will move selectively toward whichever surface is the most hydrophobic.

When a bubble was present it would often pop approximately one second after bridge breakup. In an industrial printing process, where the pattern may dry within milliseconds of being printed, it is possible that the bubble does not pop but is instead dried into the final product. This type of defect could go unnoticed in graphics arts applications, because the bubble may not produce a visibly different feature from one that had printed correctly. However, a bubble in a printed circuit could significantly alter the electrical properties of the device. This highlights the importance of understanding and controlling the dynamics of the bubbles during printing.

6.2 Future research directions

In this thesis we have worked to understand how a variety of physical phenomena alter the stretching and breakup behavior of liquid bridges. We have discussed several avenues through which liquid transfer can be improved, including the use of wider cavities to minimize contact-line pinning, and of inertia to overcome an unfavorable wettability difference. While this work has begun to eke out some of the physical mechanisms through which liquid transfer occurs, there are still many questions that must be answered before a complete picture of gravure printing is obtained. Here we summarize a few of the areas which warrant further investigation.

First and foremost, industrial printing inks are hardly ever Newtonian, and often contain polymeric resins and/or ink particles. This can significantly alter the dynamics of printing as these compounds can affect both the surface tension and the viscosity of the printing fluid. Fluid rheology is an especially important factor to consider because printing inks are often viscoelastic, and so a better understanding of how viscoelasticity interacts with wettability is important in improving our understanding of printing. The presence of particles or polymer will also modify our definition of the print quality, as the important parameter is no longer the *liquid* transfer but the *ink* transfer. In a non-homogeneous system it is possible that one achieves a high solvent (liquid) transfer but a low ink transfer, resulting in poor pattern resolution after drying. To study these effects we suggest the use of the long-wave model, presented in §3.2.2. This model allows for the inclusion of additional physics, such as viscoelasticity or the interfacial transport of surfactant, with only a small increase in computational cost as compared to a full two- (or three-) dimensional simulation. However, because the long-wave model cannot account for the fluid within a cavity, it can only be used to study stretching between flat plates, which is a model problem for offset printing.

A two- (or three-) dimensional technique is still required to study cavity emptying.

In addition to rheological effects, gravure printing is often performed with an applied electric field to aid in cavity emptying. This electric field is thought to play two separate roles. First, by distorting the interface of the liquid in the cavity the electric field ensures that good contact is obtained between the liquid and the substrate, without the need for excessive pressure from the backing roll (George, 1982). Second, if a conductive ink is being printed the electric field can improve the transfer of particles to the substrate. Modeling the effect of an electric field on both the wetting and bulk fluid dynamics is most easily done using the long-wave model for the same reasons discussed in the previous paragraph, though again a two or three dimensional simulation is required to study cavity emptying.

In this thesis we have treated the web as a rigid, flat surface, even though the deformability of the web has been shown to play an important role in modifying the fluid mechanics within the cavity (Yin and Kumar, 2005, 2006b; Hewson et al., 2010). Incorporating the mechanics of the solid surfaces into our model is thus important in capturing the dynamics of gravure printing. Additionally, this would allow the study of flexographic printing, described in section 1.1.4, where liquid transfer occurs between an (ideally) rigid substrate and a flexible rubber post. Of particular interest is the deformation of the rubber posts, which can wear over time and reduce the fidelity of the printed pattern. An improved understanding of how the fluid and solid mechanics couple to alter the bridge breakup dynamics should make it possible to suggest material properties for optimal pattern transfer over a long print run.

It is important to note that one of the biggest limitations in any printing process model is our current understanding of wetting phenomena. Even seemingly simple matters such as the spreading of a drop over a surface are not completely understood (Blake, 2006), and the dynamics of wetting remains a hotly studied field (see for example Vandre, 2013). The motion of the contact line in a liquid bridge system is especially complex because it involves dynamic wetting with both advancing and receding contact lines, and therefore is also subject to contact angle hysteresis. There is currently no model available that can account for such complex behavior, which leads most authors (ourselves included) to simplify the wetting dynamics in the interest of gaining some insight into the problem at hand. Additionally, it is unclear how effects such as fluid rheology alter the motion of the contact line, complicating studies of liquid bridges with non-Newtonian fluids. Therefore, until a more complete understanding of the dynamics of wetting exists only qualitative agreement between theory and experiments can be expected.

In sections 1.2.2 and 1.2.3 we alluded to the importance of hydrodynamic interaction between adjacent cavities in understanding liquid transfer. Modeling such a system requires resolving multiple liquid bridges in three dimensions, which is not currently feasible with the finite element technique discussed in chapter 4. Experimental studies thus provide the best opportunity to understand this interaction between cavity arrangement and liquid

transfer. While preliminary work in this area has already been performed by Chuang et al. (2008), the use of opaque rolls prevented them from visualizing the liquid transfer process. Flow visualization experiments using a transparent backing roll can help in providing insight into the dynamics of cavity emptying (Hanumanthu, 1999). However, it would be extremely difficult to observe the dynamics of the liquid within the cavity through the backing roll. We propose the fabrication of transparent cavities through which the liquid transfer process can be directly observed. Rigid, transparent cavities can be made using a polyurethane casting mold, whose surface can be modified chemically to control the wettability. This allows for direct visualization of the fluid within the cavity using the technique implemented in chapter 5 so that we can develop an understanding of how the cavity shape/arrangement alters the breakup dynamics and liquid transfer during stretching.

While the work in this thesis has focused on the emptying of cavities, an equally relevant problem is the filling and doctoring of cavities. These are important phenomena to understand because they set the initial state of the liquid as it enters the printing nip. If the cavity is under-filled because of poor filling/doctoring, this can lead to the entrapment of bubbles and a decrease in liquid transfer (see chapter 5). In contrast, if the cavity is over-filled the printed feature will be larger than expected, resulting in poor pattern resolution. A better understanding of the conditions under which cavities are properly filled and doctored is vital for the development of a printing operability window.

Ultimately, the goal of research on gravure is in developing a complete, predictive model for the entire process, including cavity filling, doctoring, and emptying. Because of the complex physics and disparity in length scales present in a typical printing press, the best hope for this is to build coarse-grained models for each individual step into an overall process model. This kind of multi-scale approach has already been implemented at Sandia National Labs to study the imbibition of liquid for nano-imprint lithography (Roberts and Schunk, 2010). The successful application of such a model to gravure printing would represent a huge leap forward in our understanding of the process.

6.3 Final remarks

Liquid bridges have been studied for nearly two centuries because of their elegance and simplicity. The recent burst in research for applications including the lapping of cats and the self-defense of beetles, not to mention the industrial printing processes discussed throughout this thesis, has shown that liquid bridges play a vital role in many aspects of our lives. We have attempted to advance our understanding of how wetting dynamics interact with various physical properties of liquid bridge systems to alter their breakup dynamics. While there is still much that remains unclear, we hope that this thesis has provided a starting point toward a deeper understanding of liquid transfer and printing.

Bibliography

Abramoff, M. D., Magelhaes, P. J., Ram, S. J., 2004. Image processing with imagej. Biophotonics International 11, 36–42.

Ahmed, D. H., Sung, H. J., Kim, D.-S., 2011. Simulation of non-Newtonian ink transfer between two separating plates for gravure-offset printing. Int. J. Heat Fluid Flow 32, 298–307.

Ambravaneswaran, B., Basaran, O. A., 1999. Effects of insoluble surfactants on the nonlinear deformation and breakup of stretching liquid bridges. Phys. Fluids 11, 997–1015.

Amestoy, P. R., Duff, I. S., Koster, J., L'Excellent, J. Y., 2001. A fully asynchronous multifrontal solver using distributed dynamic scheduling. SIAM J. Matrix Anal. A. 23, 15–41.

Baer, T. A., Cairncross, R. A., Schunk, P. R., Rao, R. R., Sackinger, P. A., 2000. A finite element method for free surface flows of incompressible fluids in three dimensions. part II. dynamic wetting lines. Int. J. Numer. Meth. Fluids 33, 405–427.

Balu, B., Berry, A. D., Hess, D. W., Breedveld, V., 2009. Patterning of superhydrophobic paper to control the mobility of micro-liter drops for two-dimensional lab-on-paper applications. Lab Chip 9, 3066–3075.

Bao, Z., Feng, Y., Dodabalapur, A., Raju, V. R., Lovinger, A. J., 1997. High-performance plastic transistors fabricated by printing techniques. Chem. Mater. 9, 1299–1301.

Benkreira, H., Cohu, O., 1998. Direct forward gravure coating on unsupported web. Chem. Eng. Sci. 53, 1223–1231.

Benkreira, H., Patel, R., 1993. Direct gravure roll coating. Chem. Eng. Sci. 48, 2329–2335.

Bharathan, J., Yang, Y., 1998. Polymer electroluminescent devices processed by inkjet printing: I. polymer light-emitting logo. Appl. Phys. Lett. 72, 2660–2662.

Bhat, P. P., Appathurai, S., Harris, M. T., Pasquali, M., McKinley, G. H., Basaran, O. A., 2010. Formation of beads-on-a-string structures during break-up of viscoelastic filaments. Nature Phys. 6, 625–631.

Bird, J. C., de Ruiter, R., Courbin, L., Stone, H. A., 2010. Daughter bubble cascades produced by folding of ruptured thin films. Nature 465, 759–762.

Birnstock, J., Blässing, J., Hunze, A., Scheffel, M., Stößel, M., Heuser, K., Wittmann, G., Wörle, J., Winnacker, A., 2001. Screen-printed passive matrix displays based on light-emitting polymers. Appl. Phys. Lett. 78 (24), 3905–3907.

Blake, T. D., 2006. The physics of moving wetting lines. J. Colloid Interface Sci. 299, 1–13.

Blanchard, A. P., Kaiser, R. J., Hood, L. E., 1996. High-density oligonucleotide arrays. Biosens. Bioelectron. 11, 687–690.

Bonito, A., Picasso, M., Laso, M., 2006. Numerical simulation of 3D viscoelastic flows with free surfaces. J. Comput. Phys. 215, 691–716.

Bonn, D., Eggers, J., Indekeu, J., Meunier, J., Rolley, E., 2009. Wetting and spreading. Rev. Mod. Phys. 81, 739–805.

Cai, S., Bhushan, B., 2008. Meniscus and viscous forces during separation of hydrophillic and hydrophobic surfaces with liquid-mediated contacts. Mater. Sci. Eng., R 61, 78–106.

Cairncross, R. A., Schunk, P. R., Baer, T. A., Rao, R. R., Sackinger, P. A., 2000. A finite element method for free surface flows of incompressible fluids in three dimensions. part I. boundary fitted mesh motion. Int. J. Numer. Meth. Fluids 33, 375–403.

Chadov, A. V., Yakhnin, E. D., 1979. Investigation of the transfer of a liquid from one solid surface to another. 1. slow transfer. method of approximate calculation. Kolloidn. Zh. 41, 817–820.

Chatzidai, N., Giannousakis, A., Dimakopoulos, Y., Tsamopoulos, J., 2009. On the elliptic mesh generation in domains containing multiple inclusions and undergoing large deformations. J. Comput. Phys. 228, 1980–2011.

Chauhan, S., Palmieri, F., Bonnecaze, R. T., Willson, C. G., 2009. Pinning at template feature edges for step and flash imprint lithography. J. Appl. Phys. 106, 034902.

Chen, A. U., Notz, P. K., Basaran, O. A., 2002. Computational and experimental analysis of pinch-off and scaling. Phys. Rev. Lett. 88, 173501.

Chen, Y.-J., Steen, P. H., 1997. Dynamics of inviscid capillary breakup: collapse and pinchoff of a film bridge. J. Fluid Mech. 341, 245–267.

Christodoulou, K. N., Kistler, S. F., Schunk, P. R., 1997. Advances in computational methods for free-surface flows. In: Kistler, S. F., Schweizer, P. M. (Eds.), Liquid Film Coating. Chapman Hall, London, UK, pp. 297–366.

Chuang, H.-K., Lee, C.-C., Liu, T.-J., 2008. An experimental study on the pickout of scaled up gravure cells. Intern. Polymer Processing xxiii, 216–222.

Clark, R. N., 2011. Notes on the resolution and other details of the human eye. URL `http://www.clarkvision.com/articles/eye-resolution.html`

Cohen, E., Gutoff, E. (Eds.), 1992. Modern coating and drying technology. Wiley-VCH.

Craster, R. V., Matar, O. K., 2009. Dynamics and stability of thin liquid films. Rev. Mod. Phys. 81, 1131–1198.

Creagh, L. T., McDonald, M., 2003. Design and performance of inkjet print heads for non-graphic-arts applications. Mater. Res. Soc. Bull. 28, 807–811.

Crouch, J. P., 1998. Flexography primer. GATFPress.

Darhuber, A. A., Troian, S. M., Wagner, S., 2001. Physical mechanisms governing pattern fidelity in microscale offset printing. J. Appl. Phys. 90, 3602–3609.

Davis, A. M. J., Frenkel, A. L., 1992. Cylindrical liquid bridges squeezed between parallel plates: exact Stokes flow solutions and hydrodynamic forces. Phys. Fluids A 4, 1105–1109.

De Souza, E. J., Brinkmann, M., Mohrdieck, C., Crosby, A., Arzt, E., 2008. Capillary forces between chemically different substrates. Langmuir 24, 10161–10168.

Dimitrakopoulos, P., Higdon, J. J. L., 2003. On the displacement of fluid bridges from solid surfaces in viscous pressure-driven flows. Phys. Fluids 15, 3255–3258.

Ding, J. M., Vornbrock, A. F., Ting, C., Subramanian, V., 2009. Patternable polymer bulk heterojunction photovoltaic cells on plastic by rotogravure printing. Sol. Energy Mater. Sol. Cells 93, 459–464.

Dodds, S., Carvalho, M., Kumar, S., 2009. Stretching and slipping of liquid bridges near plates and cavities. Phys. Fluids 21, 092103.

Dodds, S., Carvalho, M. S., Kumar, S., 2011a. Stretching liquid bridges with bubbles: the effect of air bubbles on liquid transfer. Langmuir 27, 1556–1559.

Dodds, S., Carvalho, M. S., Kumar, S., 2011b. Stretching liquid bridges with moving contact lines: the role of inertia. Submitted to Phys. Fluids.

Doshi, P., Suryo, R., Yildirim, O. E., McKinley, G. H., Basaran, O. A., 2003. Scaling in pinch-off of generalized Newtonian fluids. J. Non-Newtonian Fluid Mech. 113, 1–27.

Durr, M., Schmid, A., Obermaier, M., Rosselli, S., Yasuda, A., Nelles, G., 2005. Low-temperature fabrication of dye-sensitized solar cells by transfer of composite porous layers. Nat. Mater 4, 607–611.

Eggers, J., 1993. Universal pinching of 3D axisymmetric free-surface flow. Phys. Rev. Lett. 71, 3458–3460.

Eggers, J., 1995. Theory of drop formation. Phys. Fluids 7, 941–953.

Eggers, J., 1997. Nonlinear dynamics and breakup of free-surface flows. Rev. Mod. Phys. 69, 865–929.

Eggers, J., Dupont, T. F., 1994. Drop formation in a one-dimensional approximation of the navier-stokes equation. J. Fluid Mech. 262, 205–221.

Eggers, J., Villermaux, E., 2008. Physics of liquid jets. Rep. Prog. Phys. 71, 036601.

Foteinopoulou, K., Mavrantzas, V. G., Dimakopoulos, Y., Tsamopoulos, J., 2006. Numerical simulation of multiple bubbles growing in a newtonian liquid filament undergoing stretching. Phys. Fluids 18, 042106.

Foteinopoulou, K., Mavrantzas, V. G., Tsamopoulos, J., 2004. Numerical simulation of bubble growth in newtonian and viscoelastic filaments undergoing stretching. J. Non-Newtonian Fluid Mech. 122, 177–200.

Frankel, I., Weihs, D., 1985. Stability of a capillary jet with linearly increasing axial velocity (with application to shaped charges). J. Fluid Mech. 155, 289–307.

Frankel, I., Weihs, D., 1987. Influence of viscosity on the capillary instability of a stretching jet. J. Fluid Mech. 185, 361–383.

Gamota, D. R., Brazis, P., Kalyanasundaram, K., Zhang, J. (Eds.), 2004. Printed Organic and Molecular Electronics. Kluwer Academic Publishers.

Gaudet, S., McKinley, G. H., Stone, H. A., 1996. Extensional deformation of Newtonian liquid bridges. Phys. Fluids 8, 2568–2579.

George, H. F., 1982. ACS Symposium Series: Colloids and Surfaces in Reprographic Technology. American Chemical Society, Ch. 18: Electrostatically assisted ink transfer in gravure printing, pp. 359–370.

Ghadiri, F., Ahmed, D. H., Sung, H. J., Shirani, E., 2011. Non-Newtonian ink transfer in gravure-offset printing. Int. J. Heat Fluid Flow 32, 308–317.

Gillette, R. D., Dyson, D. C., 1971. Stability of fluid interfaces of revolution between equal solid circular plates. Chem. Eng. J. 2, 44–88.

Gresho, P. M., Lee, R. L., Sani, R. L., 1980. On the time-dependent solution of the incompressible Navier-Stokes equations in two and three dimensions. In: Taylor, C., Morgan, K. (Eds.), Recent Advances in Numerical Methods in Fluids. Pineridge Press, Swansea, UK, pp. 27–79.

Gupta, C., Mensing, G. A., Shannon, M. A., Kenis, P. J. A., 2007. Double transfer printing of small volumes of liquids. Langmuir 23, 2906–2914.

Hagberg, J., Pudas, M., Leppävuori, S., Elsey, K., Logan, A., 2001. Gravure offset printing development for fine line thick film circuits. Microelectron. Int. 18, 32–35.

Han, M. G., Sperry, J., Gupta, A., Huebner, C. F., Ingram, S. T., Foulger, S. H., 2007. Polyaniline coated poly(butyl methacrylate) core-shell particles: roll-to-roll printing of templated electrically conductive structures. J. Mater. Chem. 17, 1347–1352.

Hanumanthu, R., 1996. Patterned roll coating. Ph.D. thesis, University of Minnesota.

Hanumanthu, R., 1999. Variation of gravure coating thickness during early stages of doctor blade wear. AIChE Journal 45, 2487–2494.

Hewson, R., Kapur, N., Gaskell, P., 2010. Tri-helical gravure roll coating. Chem. Eng. Sci. 65, 1311–1321.

Hewson, R. W., Kapur, N., Gaskell, P. H., 2006. A theoretical and experimental investigation of tri-helical gravure roll coating. Chem. Eng. Sci. 61, 5487–5499.

Hewson, R. W., Kapur, N., Gaskell, P. H., 2009. Modelling the discrete-cell gravure roll coating process: A new perspective. Eur. Phys. J. Special Topics 166, 99–102.

Hoda, N., Kumar, S., 2008. Boundary integral simulations of liquid emptying from a model gravure cell. Phys. Fluids 20, 092106.

Huang, W.-X., Lee, S.-H., Sung, H. J., Lee, T.-M., Kim, D.-S., 2008. Simulation of liquid transfer between separating walls for modeling micro-gravure-offset printing. Int. J. Heat Fluid Flow 29, 1436–1446.

Hughes, T. R., Mao, M., Jones, A. R., Burchard, J., Morton, M. J., Shannon, K. W., Lefkowitz, S. M., Ziman, M., Schelter, J. M., Meyer, M. R., Kobayashi, S., Davis, C., Dai, H., He, Y. D., Stephaniants, S. B., Cavet, G., Walker, W. L., West, A., Coffey, E., Shoemaker, D. D., Stoughton, R., Blanchard, A. P., Friend, S. H., Linsley, P. S., 2001. Expression profiling using microarrays fabricated by an ink-jet oligonucleotide synthesizer. Nat. Biotechnol. 19, 342–347.

Huh, C., Scriven, L., 1971. Hydrodynamic model of a steady movement of a solid/liquid/fluid contact line. J. Colloid Interface Sci. 35, 85–101.

Ingram, S., 1999. Screen printing primer. GATFPress.

Jung, S., Reis, P. M., James, J., Clanet, C., Bush, J. W. M., 2009. Capillary origami in nature. Phys. Fluids 21, 091110.

Kang, H. W., Sung, H. J., Lee, T.-M., Kim, D.-S., Kim, C.-J., 2009. Liquid transfer between two separating plates for micro-gravure-offset printing. J. Micromech. Microeng. 19, 015025.

Kapur, N., 2003. A parametric study of direct gravure coating. Chem. Eng. Sci. 58, 2875–2882.

Kapur, N., Gaskell, P. H., Bates, A., 2001. A parametric study of offset gravure coating. Trans. IChemE. 79, 41–50.

Kasunich, C., 1998. Gravure Primer. GATFPress.

Kawahara, T., Doushita, K., Tada, H., 2003. A large area patterner by TiO_2/SnO_2 bilayer type photocatalyst prepared by gravure printing. J. Sol-Gel Sci. Technol. 27, 301–307.

Kim, S., Na, Y., 2010. Study on the web deformation in ink transfer process for R2R printing application. Int. J. Precis. Eng. Man. 11, 945–954.

Kipphan, H. (Ed.), 2001. Handbook of Print Media. Springer-Verlag.

Kistler, S., March 1988. Flexible-blade doctoring in gravure coating. In: AIChE Spring National Meeting, New Orleans. AIChE, (unpublished).

Kistler, S. F., Schweizer, P. M. (Eds.), 1997. Liquid film coating: scientific principles and their technological implications. Chapman Hall, London, UK.

Kistler, S. F., Scriven, L. E., 1984. Coating flow theory by finite element and asymptotic analysis of the Navier-Stokes system. Int. J. Numer. Methods Fluids 4, 207–229.

Kittilä, M., Hagberg, J., Jakku, E., Leppävuori, S., 2004. Direct gravure printing (dgp) method for printing fine-line electrical circuits on ceramics. IEEE Trans. Electronics Packaging Manufacturing 27, 109–114.

Kopola, P., Aernouts, T., Guillerez, S., Jin, H., Tuomikoski, M., Maaninen, A., Hast, J., 2010. High efficient plastic solar cells fabricated with a high-throughput gravure printing method. Sol. Energy Mater. Sol. Cells 94, 1673–1680.

Krebs, F. C., 2009. Fabrication and processing of polymer solar cells: A review of printing and coating techniques. Sol. Energy Mater. Sol. Cells 93, 394–412.

Ku, H. C., Hirsh, R. S., Taylor, T. D., 1987. A pseudospectral method for solution of the three-dimensional incompressible Navier-Stokes equations. J. Comp. Phys. 70, 439–462.

Kusumaatmaja, H., Lipowsky, R., 2010. Equilibrium morphologies and effective spring constants of capillary bridges. Langmuir 26, 18734–18741.

Kwak, M. K., Shin, K. H., Yoon, E. Y., Suh, K. Y., 2010. Fabrication of conductive metal lines by plate-to-roll pattern transfer utillizing edge dewetting and flexographic printing. J. Colloid Interf. Sci. 343, 301–305.

Larson, M., 2007. Century-old litho printed jumps to flexo. Converting Magazine 25, 52–54.

Lee, S., Na, Y., 2010. Analysis on the ink transfer mechanism in R2R application. J. Mech. Sci. Technol 24, 293–296.

Lee, T.-M., Lee, S.-H., Noh, J.-H., Kim, D.-S., Chun, S., 2010. The effect of shear force on ink transfer in gravure offset printing. J. Micromech. Microeng. 20, 125026.

Lenz, R. D., Kumar, S., 2007. Competitive displacement of thin liquid films on chemically patterned substrates. J. Fluid Mech. 571, 33–57.

Liao, Y.-C., Franses, E. I., Basaran, O. A., 2006. Deformation and breakup of a stretching liquid bridge covered with an insoluble surfactant monolayer. Phys. Fluids 18, 022101.

Lister, J. R., Stone, H. A., 1998. Capillary breakup of a viscous thread surrounded by another viscous fluid. Phys. Fluids 10, 2758–2764.

Lockwood, A. J., Anantheshwara, K., Bobji, M. S., Inkson, B. J., 2011. Friction-formed liquid drops. Nanotechnology 22, 105703.

MacPhee, J., 1998. Fundamentals of Lithographic Printing. GATF*Press*.

Mäkelä, T., Kosonen, H., Bäcklund, T. G., Sandberg, H. G. O., Stubb, H., 2005. Utilizing roll-to-roll techniques for manufacturing source/drain electrodes for all-polymer transistors. Synth. Met. 153, 285–288.

Marín, J. M. R., Rasmussen, H. K., Hassager, O., 2010. 3D simulation of nono-imprint lithography. Nanoscale Res. Lett. 5, 274–278.

Markets and Markets, 2011.
URL `http://www.marketsandmarkets.com/Market-Reports/printed-electronics-market-197.html`

McKinley, G. H., Sridhar, T., 2002. Filament-stretching rheometry of complex fluids. Annu. Rev. Fluid Mech. 34, 375–415.

Meseguer, J., 1983. The breaking of axisymmetric slender liquid bridges. J. Fluid Mech. 130, 123–151.

Meseguer, J., Sanz, A., 1985. Numerical and experimental study of the dynamics of axisymmetric slender liquid bridges. J. Fluid Mech. 153, 83–101.

Michel, B., Bernard, A., Bietsch, A., Delamarche, E., Geissler, M., Juncker, D., Kind, H., Renault, J., Rothuizen, H., Schmid, H., Schmidt-Winkel, P., Stutz, R., Wolf, H., 2001. Printing meets lithography: Soft approaches to high-resolution patterning. IBM J. Res. and Dev. 45, 697–719.

Mikami, T., Cox, R. G., Mason, S. G., 1975. Breakup of extending liquid threads. Int. J. Multiphase Flow 2, 113–138.

Noh, J., Yeom, D., Lim, C., Cha, H., Han, J., Kim, J., Park, Y., Subramanian, V., Cho, G., 2010. Scalability of roll-to-roll gravure-printed electrodes on plastic foils. IEEE Trans. Electronics Packaging Manufacturing 33, 275–283.

Oron, A., Davis, S. H., Bankoff, S. G., 1997. Long-scale evolution of thin liquid films. Rev. Mod. Phys. 69, 931–980.

Orr, F. M., Scriven, L. E., Rivas, A. P., 1975. Pendular rings between solids: meniscus properties and capillary force. J. Fluid Mech. 67, 723–742.

Panditaratne, J. C., 2003. Deflection of microjets induced by asymmetric heating and related free surface flows with moving contact lines. Ph.D. thesis, Purdue University.

Papageorgiou, D., 1995. On the breakup of viscous liquid threads. Phys. Fluids 7, 1529–1544.

Parashkov, R., Becker, E., Riedl, T., Johannes, H.-H., Kowalsky, W., 2005. Large area electronics using printing methods. Proc. IEEE 93, 1321–1329.

Pardo, D. A., Jabbour, G. E., Peyghambarian, N., 2000. Application of screen printing in the fabrication of organic light-emitting devices. Adv. Mater. 12 (24), 1249–1252.

Patel, R., Benkreira, H., 1991. Gravure roll coating of Newtonian liquids. Chem. Eng. Sci. 46, 751–756.

Pepin, X., Rossetti, D., Iveson, S. M., Simons, S. J. R., 2000. Modeling the evolution and rupture of pendular liquid bridges in the presence of large wetting hysteresis. J. Colloid Interface Sci. 232, 289–297.

Plateau, J. A. F., 1863. Experimental and theoretical researches on the figures of equilibrium of a liquid mass withdrawn from the action of gravity, etc. In: Annual reports of the Smithsonian Institution. Smithsonian Institution Press, Washington, DC.

Powell, C. A., Savage, M. D., Gaskell, P. H., 2000. Modelling the meniscus evacuation problem in direct gravure coating. Trans. IChemE 78, 61–67.

Powell, C. A., Savage, M. D., Guthrie, J. T., 2002. Computational simulation of the printing of Newtonian liquid from a trapezoidal cavity. Int. J. Numer. Meth. Heat Fluid Flow 12, 338–355.

Prakash, M., Quéré, D., Bush, J. W. M., 2008. Surface tension transport of prey by feeding shorebirds: The capillary ratchet. Science 320, 931–934.

Puah, L. S., Sedev, R., Fornasiero, D., Ralston, J., Blake, T., 2010. Influence of surface charge on wetting kinetics. Langmuir 26, 17218–17224.

Pudas, M., Hagberg, J., Leppavuori, S., 2004. Printing parameters and ink components affecting ultra-fine-line gravure-offset printing for electronics applications. J. Eur. Ceram. Soc. 24, 2943–2950.

Pudas, M., Halonen, N., Granat, P., Vähäkangas, J., 2005. Gravure printing of conductive particulare polymer inks on flexible substrates. Prog. Org. Coat. 54, 310–316.

Pulkrabek, W. W., Munter, J. D., 1983. Knurl roll design for stable rotogravure coating. Chem. Eng. Sci. 38, 1309–1314.

Py, C., Reverdy, P., Doppler, L., Bico, J., oman, B., Baroud, C. N., 2007. Capillary origami: spontaneous wrapping of a droplet with an elastic sheet. Phys. Rev. Lett. 98, 156103.

Qian, B., Breuer, K. S., 2011. The motion, stability and breakup of a stretching liquid bridge with a receding contact line. J. Fluid Mech. 1, 1.

Qian, B., Loureiro, M., Gagnon, D. A., Tripathi, A., Breuer, K. S., 2009. Micron-scale droplet deposition on a hydrophobic surface using a retreating syringe. Phys. Rev. Lett. 102, 164502.

Ranabothu, S. R., Karnezis, C., Dai, L. L., 2005. Dynamic wetting: Hydrodynamic or molecular-kinetic? J. Colloid Interface Sci. 288, 213–221.

Rasmussen, H. K., Hassager, O., 1999. Three-dimensional simulations of viscoelastic instability in polymeric filaments. J. Non-Newtonian Fluid Mech. 82, 189–202.

Lord Rayleigh, 1878. On the intability of jets. Proc. London Math. Soc. 10, 4–13.

Reddy, S., Schunk, P. R., Bonnecaze, R. T., 2005. Dynamics of low capillary number interfaces moving through sharp features. Phys. Fluids 17, 122104.

Reis, P. M., Jung, S., Aristoff, J. M., Stocker, R., 2010. How cats lap: water uptake by *Felis catus*. Science 330, 1231–1234.

Renardy, M., 2002. Similarity solutions for jet breakup for various models of viscoelastic fluids. J. Non-Newtonian Fluid. Mech. 104, 65–74.

Renardy, M., Renardy, Y., 2004. Similarity solutions for breakup of jets of power law fluids. J. Non-Newtonian Fluid Mech. 122, 303–312.

Rivas, D., Meseguer, J., 1984. One-dimensional self-similar solution of the dynamics of axisymmetric slender liquid bridges. J. Fluid Mech. 138, 417–429.

Roberts, S. A., Schunk, P. R., 2010. Multiscale model development of pattern nano-imprinting process, AIChE Annual Meeting, Salt Lake City, UT (unpublished).

Saha, A. A., Mitra, S. K., 2009. Effect of dynamic contact angle in a volume of fluid (VOF) model for a microfluidic capillary flow. J. Colloid Interface Sci. 339, 461–480.

Santa-Nokki, H., Kallioinen, J., Kololuoma, T., Tuboltsev, V., Korppi-Tommola, J., 2006. Dynamic preparation of TiO_2 films for fabrication of dye-sensitized solar cells. J. Photochem. Photobiol., A 182, 187–191.

Scardovelli, R., Zaleski, S., 1999. Direct numerical simulation of free-surface and interfacial flow. Annu. Rev. Fluid Mech. 31, 567–603.

Schwartz, L. W., 2002. Numerical modelling of liquid withdrawl from gravure cavities in coating operations: the effect of cell pattern. J. Eng. Maths 42, 243–253.

Schwartz, L. W., Moussalli, P., Campbell, P., Eley, R. R., 1998. Numerical modelling of liquid withdrawl from gravure cavities in coating operations. Trans. IChemE. 76, 22–28.

Scriven, L. E., 2005. Fine-structured materials by continuous coating and drying or curing of liquid precursors. In: Galán, M. A., Valle, E. M. D. (Eds.), Chemical Engineering: Trends and Developments. John Wiley & Sons, Ltd, Chichester, UK, pp. 229–266.

Sekitani, T., Takamiya, M., Noguchi, Y., Nakano, S., Kato, Y., Sakurai, T., Someya, T., 2007. A large-area wireless power-transmission sheet using printed organic transistors and plastic MEMS switches. Nat. Mater 6, 413–417.

Sethian, J. A., Smereka, P., 2003. Level set methods for fluid interfaces. Annu. Rev. Fluid Mech. 35, 341–372.

Shikhmurzaev, Y. D., 1993. The moving contact line on a smooth solid surface. Int. J. Multiphase Flow 19, 589–610.

Shimoda, T., Morii, K., Seki, S., Kiguchi, H., 2003. Inkjet printing of light-emitting polymer displays. Mater. Res. Soc. Bull. 28, 821–827.

Shipman, R. W. G., Denn, M. M., Keunings, R., 1991. Mechanics of the "falling plate"extensional rheometer. J. Non-Newtonian Fluid Mech. 40, 281–288.

Sirringhaus, H., Kawase, T., Friend, R. H., Shimoda, T., Inbasekaran, M., Wu, W., Woo, E. P., 2000. High-resolutions inkjet printing of all-polymer transistor circuits. Science 290, 2123–2126.

Slobozhanin, L. A., Perales, J. M., 1993. Stability of liquid bridges between equal disks in an axial gravity field. Phys. Fluids A 5, 1305–1314.

Southee, D., Hay, G. I., Evans, P. S. A., Harrison, D. J., 2007. Lithographically printed voltaic cells - a feasibility study. Circuit World 33, 31–35.

Sridhar, R., Tirtaatmadja, V., Nguyen, D. A., Gupta, R. K., 1991. Measurement of extensional viscosity of polymer solutions. J. Non-Newtonian Fluid Mech. 40, 271–280.

Stone, H. A., 2010. Interfaces: in fluid mechanics and across disciplines. J. Fluid Mech. 645, 1–25.

Tjahjadi, M., Stone, H. A., Ottino, J. M., 1992. Satellite and subsatellite formation in capillary breakup. J. Fluid Mech. 243, 297–317.

Tomotika, S., 1936. Breaking up of a drop of viscous liquid immersed in another viscous fluid which is extending at a uniform rate. Proc. Roy. Soc. A 153, 302–318.

Urso, M. E. D., Lawrence, C. J., Adams, M. J., 2002. A two-dimensional study of the rupture of funicular liquid bridges. Chem. Eng. Sci. 57, 677–692.

Vagharchakian, L., Restagno, F., Léger, L., 2009. Capillary bridge formation and breakage: A test to characterize antiadhesive surfaces. J. Phys. Chem. B 113, 3769–3775.

van Hoeve, W., Gekle, S., Snoeijer, J. H., Versluis, M., Brenner, M. P., Lohse, D., 2010. Breakup of diminutive *r*ayleigh jets. Phys. Fluids 22, 122003.

Vandre, E., 2013. Interface dynamics in high-speed coatings. Ph.D. thesis, The University of Minnesota, (in progress).

Villaneuva, W., Sjödahl, J., Stjernström, M., Roeraade, J., Amberg, G., 2007. Microdroplet deposition under a liquid medium. Langmuir 23, 1171–1177.

Vogel, M. J., Steen, P. H., 2010. Capillarity-based switchable adhesion. PNAS 107, 3377–3381.

Walkley, M. A., Gaskell, P. H., Jimack, P. K., Kelmanson, M. A., Summers, J. L., 2005a. Finite element simulation of three-dimensional free-surface flow problems. J. Sci. Comput. 24, 147–162.

Walkley, M. A., Gaskell, P. H., Jimack, P. K., Kelmanson, M. A., Summers, J. L., 2005b. Finite element simulation of three-dimensional free-surface flow problems with dynamic contact lines. Int. J. Numer. Meth. Fluids 47, 1353–1359.

Weinstein, S. J., Ruschak, K. J., 2004. Coating flows. Annu. Rev. Fluid Mech. 36, 29–53.

Wilson, D. G., 2005. Lithography primer. GATFPress.

Xie, X., Musson, L. C., Pasquali, M., 2007. An isochoric domain deformation method for computing steady free surface flows with conserved volumes. J. Comput. Phys. 226, 398–413.

Yakhnin, E. D., Chadov, A. V., 1983. Investigation of the transfer of a liquid from one solid surface to another. 2. dynamic transfer. Kolloidn. Zh. 45, 1183–1188.

Yao, M., McKinley, G. H., 1998. Numerical simulation of extensional deformations of viscoelastic liquid bridges in filament stretching devices. J. Non-Newtonian Fluid Mech. 74, 47–54.

Yildirim, O. E., Basaran, O. A., 2001. Deformation and breakup of stretching bridges of Newtonian and shear-thinning liquids: Comparison of one- and two-dimensional models. Chem. Eng. Sci. 56, 211–233.

Yildirim, O. E., Basaran, O. A., 2006. Dynamics of formation and dripping of drops of deformation-rate-thinning and -thickening liquids from capillary tubes. J. Non-Newtonian Fluid Mech. 136, 17–37.

Yin, X., Kumar, S., 2005. Lubrication flow between a cavity and a flexible walls. Phys. Fluids 17, 063101.

Yin, X., Kumar, S., 2006a. Flow visualization of the liquid-emptying process in scaled up gravure grooves and cells. Chem. Eng. Sci. 61, 1146–1156.

Yin, X., Kumar, S., 2006b. Two-dimensional simulations of flow near a cavity and a flexible solid boundary. Phys. Fluids 18, 063103.

Zhang, X., Padgett, R. S., Basaran, O. A., 1996. Nonlinear deformation and breakup of stretching liquid bridges. J. Fluid Mech. 329, 207–245.

Zhou, C., Yue, P., Feng, J. J., Ollivier-Gooch, C. F., Hu, H. H., 2010. 3D phase-field simulations of interfacial dynamics in Newtonian and viscoelastic fluids. J. Comput. Phys. 229, 498–511.

Zielke, D., Hübler, A., Hahn, U., Brandt, N., Bartzsch, M., Fügmann, U., Fischer, T., 2005. Polymer-based organic field-effect transistor using offset printed source/drain structures. Appl. Phys. Lett. 87, 123508.

APPENDIX A

Selection of an appropriate velocity scale

When performing a scaling analysis for gravure it is tempting to use the linear web speed, V_w, as the characteristic velocity. In this appendix we use simple geometric arguments to show that the web speed is not the relevant velocity scale, but that the liquid instead experiences a much slower extensional velocity V_E.

We begin by considering how the velocity in the vertical direction varies over the surface of a roll of radius R, shown schematically in figure A.1. At the bottom of the roll, which we define as the origin $(x, z) = (0, 0)$ in our system, the extensional velocity is zero:

$$V_E(0, 0) = 0. \tag{A.1}$$

At any point (x, z) on the surface of the roll the vertical velocity is given by:

$$V_E(x, z) = V_w \sin\theta, \tag{A.2}$$

where θ is the angle that a vector tangent to the roll makes with the horizontal direction at (x, z). We know from trigonometry that the distance x is given by $x = R\sin\theta$ (see figure A.1), so that equation (A.2) becomes:

$$V_E = V_w \frac{x}{R}. \tag{A.3}$$

We see from this equation that V_E increases linearly with x, from $V_E = 0$ at $x = 0$ to $V_E = V_w$ at $x = R$. However, the bridge will break well before it has reached the point $x = R$, and so the extensional velocity will never be as large as the web velocity.

To obtain a more reasonable estimate of the maximum extensional velocity experienced by the bridge, which is given by V_E at breakup, we note that the equation for the surface of the cylindrical roll is:

$$x^2 + (z - R)^2 = R^2, \tag{A.4}$$

which can be rearranged to give:

$$x = \sqrt{2zR - z^2}. \tag{A.5}$$

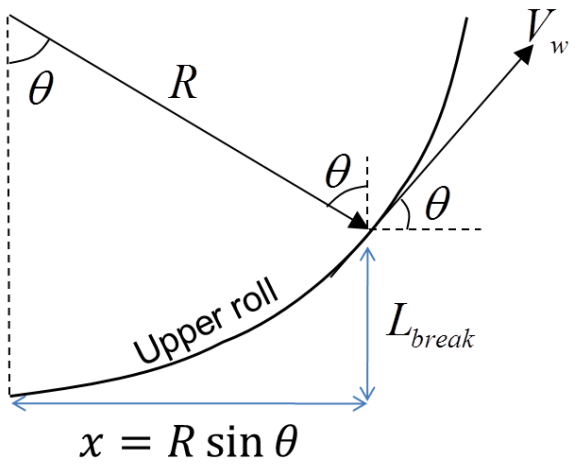

Figure A.1: Schematic of an ink jet printing apparatus

We can now substitute equation (A.5) into (A.2) to give:

$$V_E = V_w \sqrt{2\frac{L_{break}}{R} - \left(\frac{L_{break}}{R}\right)^2}, \tag{A.6}$$

where we have set $z = L_{break}$ because we are only concerned with the extensional velocity at breakup. This simple relationship allows us to estimate the maximum extensional velocity experienced by the bridge during printing. For a typical printing operation we assume that V_w is on the order of 10 m/s, and R is on the order of 6 in. Based on the results presented throughout this thesis, a reasonable estimate for the breakup length is two to five times the original feature size. Therefore, if the desired feature is on the order of 10 μm, the breakup length will be roughly 20-50 μm. After entering all of these parameters in equation (A.6), we find that V_E is roughly 0.2 m/s, which is two orders of magnitude lower than V_w. This highlights the importance of considering the geometry of the system, as simply using the web velocity to estimate the relevant dimensionless numbers (such as the capillary and Reynolds numbers) will lead to a faulty balance of the forces relevant during breakup.